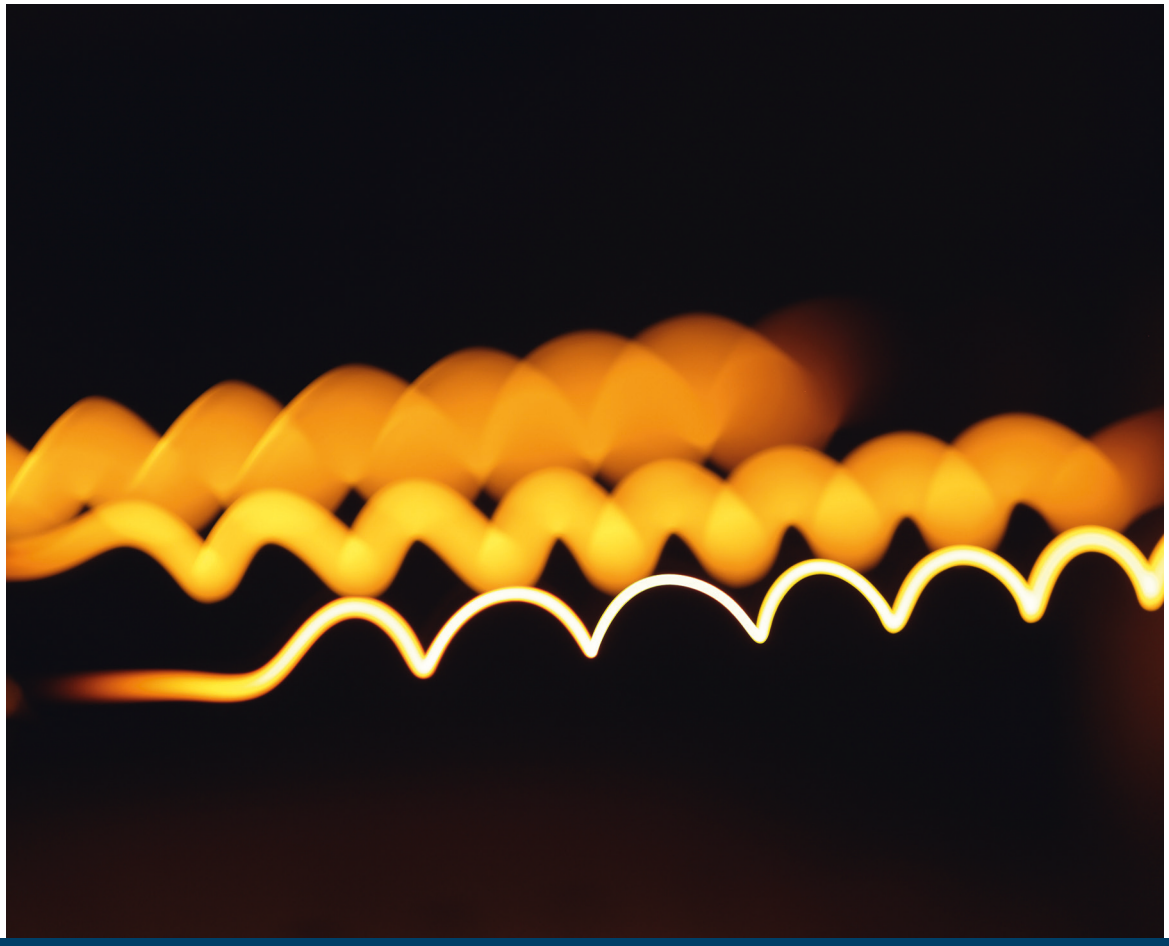

Catalytic-doping of Silicon Alloys for the Use in Silicon Heterojunction Solar Cells

Yong Liu

Energie & Umwelt / Energy & Environment
Band / Volume 556
ISBN 978-3-95806-591-8

Mitglied der Helmholtz-Gemeinschaft

JÜLICH
Forschungszentrum

Schriften des Forschungszentrums Jülich
Reihe Energie & Umwelt / Energy & Environment Band / Volume 556

Forschungszentrum Jülich GmbH
Institut für Energie- und Klimaforschung
IEK-5 Photovoltaik

Catalytic-doping of Silicon Alloys for the Use in Silicon Heterojunction Solar Cells

Yong Liu

Schriften des Forschungszentrums Jülich
Reihe Energie & Umwelt / Energy & Environment Band / Volume 556

ISSN 1866-1793 ISBN 978-3-95806-591-8

Bibliografische Information der Deutschen Nationalbibliothek.
Die Deutsche Nationalbibliothek verzeichnet diese Publikation in der
Deutschen Nationalbibliografie; detaillierte Bibliografische Daten
sind im Internet über http://dnb.d-nb.de abrufbar.

Herausgeber und Vertrieb:	Forschungszentrum Jülich GmbH Zentralbibliothek, Verlag 52425 Jülich Tel.: +49 2461 61-5368 Fax: +49 2461 61-6103 zb-publikation@fz-juelich.de www.fz-juelich.de/zb
Umschlaggestaltung:	Grafische Medien, Forschungszentrum Jülich GmbH
Druck:	Grafische Medien, Forschungszentrum Jülich GmbH
Copyright:	Forschungszentrum Jülich 2021

Schriften des Forschungszentrums Jülich
Reihe Energie & Umwelt / Energy & Environment, Band / Volume 556

D 82 (Diss. RWTH Aachen University, 2021)

ISSN 1866-1793
ISBN 978-3-95806-591-8

Vollständig frei verfügbar über das Publikationsportal des Forschungszentrums Jülich (JuSER)
unter www.fz-juelich.de/zb/openaccess.

Contents

Abstract

To make this planet cleaner and more sustainable, photovoltaic (PV) has long been on its road to pursue higher efficiency (η) and larger market share. Silicon heterojunction (SHJ) solar cell is considered as one of the most promising candidates as next-generation high-efficiency PV techniques due to their high efficiencies and simple production sequences. Efficiency over 26% in research level and over 23% in mass production have been achieved based on SHJ concept. However, there are still several efficiency-limiting issues for SHJ solar cells. The first one is the parasitic absorption in short wavelength range caused by front side doped amorphous(a-Si:H) layers. Many new materials (such as μc-Si:H, nc-SiO_x:H and μc-SiC:H) have been proposed to overcome this problem, yet the trade-off between optical and electrical properties still exists. The second one is that sufficient thickness of a-Si:H(i) layer is needed for good passivation, but the a-Si:H(i) layer acts as isolation for electrical transport. Therefore, another trade-off exists between passivation and electrical transport.

Among many techniques to solve aforementioned trade-offs and even push η forward, Catalytic-doping (Cat-doping) is a cheap, simple and industry feasible technique. Cat-doping has been reported to improve electrical property and passivation quality on films and device consisting of a-Si:H and crystalline silicon(c-Si). However, the effectiveness of Cat-doping on silicon alloys (μc-Si:H, nc-SiO_x:H and μc-SiC:H) is still unknown. The mechanism of Cat-doping on these materials is also not clear so far.

Accordingly, the first goal of this thesis was to exploit the effectiveness of Cat-doping on these silicon alloy materials in terms of electrical and optical properties. Mean-

while, deeper understanding of the mechanism of Cat-doping in different materials was needed. It is shown that P atoms can be effectively incorporated into these films by Cat-doping but with different P atom concentrations (N_{P}) and doping depths. As for a-Si:H films, N_{P} from Cat-doping can be as high as $6 \times 10^{21} cm^{-3}$ with a doping depth around 15 nm while for μc-Si:H N_{P} can reach $6 \times 10^{20} cm^{-3}$ with a doping depth of 5 nm. For nc-SiO_x:H films, N_{P} is also in the range of $10^{20} cm^{-3}$ but P atoms penetrate throughout the whole film. When it comes to μc-SiC:H films, N_{P} is only $6 \times 10^{19} cm^{-3}$ and P atoms seem to just attach to the surface of μc-SiC:H films. The difference in the behavior of Cat-doping might be attributed to the microstructures of these silicon alloys. The loose structure of a-Si:H, where a large number of voids and defects exist, possibly results in large doping concentration N_{P} and deeper doping depth for a-Si:H. The grain boundaries in μc-Si:H could also help to incorporate more P atoms. Nanocrystalline silicon oxide has a very unique porous cage microstructure that might offer channels for P atoms to penetrate the whole film during the Cat-doping process. In contrast, the dense microstructure of μc-SiC:H seems to prevent P atoms to penetrate and the P atoms only attach to the film surface.

The second goal of this work was to improve the passivation quality of different cell precursors and devices. To begin with, different gases were used during Cat-doping process and three effects (i.e. thermal annealing, hydrogenation and P doping effect) were found to co-exist accounting for the improvement of passivation quality. Then, cell precursors and devices with these silicon alloys films were treated with Cat-doping and their passivation quality were enhanced to different extend, which is also likely related to the change in material properties upon applying the Cat-doping process.

At last, the ultimate goal was to implement Cat-doping in SHJ solar cells. In general, applying Cat-doping on various doped layers in the front of SHJ solar cells results in improved η which mainly comes from improved V_{oc} and FF. Filament temperature (T_{f}), substrate temperature (T_{sub}) and processing pressure were all found to influence η and local optimal values were identified. However, the electrical property change for nc-SiO_x:H seems limited due to the low activation of Cat-doping

incorporated P atoms, the impact of Cat-doping on η of cells with nc-SiO_x:H was not significant. Beyond the traditional structure of SHJ cells, a new fabrication method where the deposition of a-Si:H(n) layer was replaced by Cat-doping on a-Si:H(i) layer was proposed. Compared to traditional SHJ cell, equivalent η from cells with new structure was achieved and has demonstrated an increase in J_{sc} about $\sim 1 mA/cm^2$. Based on this concept, when additional a-Si:H(n) layer was added to the front of the new-approach cell, a champion device of 21.2% efficiency was achieved mainly due to an increase of 4.9% in FF compared to the traditional SHJ cell structure.

Zusammenfassung

Um diesen Planeten sauberer und nachhaltiger zu machen, ist die Photovoltaik (PV) seit langem auf dem Weg, eine höhere Effizienz und einen größeren Marktanteil zu erreichen. Die Solarzelle mit Silizium-Heteroübergang (SHJ) gilt aufgrund ihrer hohen Effizienz und einfachen Produktionssequenzen als einer der vielversprechendsten Kandidaten für hocheffiziente PV-Techniken der nächsten Generation. Effizienze von über 26% im Forschungsbereich und über 23% in der Massenproduktion wurde auf der Grundlage des SHJ-Konzepts erreicht. Es gibt jedoch immer noch einige Probleme, die die Effizienz von SHJ-Solarzellen einschränken. Die erste ist die parasitäre Absorption im kurzen Wellenlängenbereich, die durch frontseitig dotierte a-Si:H-Schichten verursacht wird. Es wurden viele neue Materialien (sowie μc-Si:H, nc-SiO_x:H und μc-SiC:H) vorgeschlagen, um dieses Problem zu überwinden, dennoch besteht immer noch ein Kompromiss zwischen optischen und elektrischen Eigenschaften. Die zweite ist, dass eine ausreichende Dicke der a-Si:H(i)-Schicht für eine gute Passivierung benötigt wird, die a-Si:H(i)-Schicht jedoch als Isolation für den elektrischen Transport wirkt. Daher besteht ein weiterer Kompromiss zwischen Passivierung und elektrischem Transport.

Unter vielen Techniken, um die oben genannten Kompromisse zu lösen und sogar die Effizienz voranzutreiben, ist das katalytische Dotierung (CAT-doping) eine billige, einfache und in der Industrie praktikable Technik. Es wurde berichtet, dass CAT-doping die elektrischen Eigenschaften und die Passivierungsqualität von Filmen und Vorrichtungen verbessert, die mit a-Si: H und c-Si zusammenhängen. Die Wirksamkeit der CAT-doping auf Siliziumlegierungen (sowie μc-Si:H, nc-SiO_x:H und μc-SiC:H) ist jedoch noch unbekannt. Der Mechanismus der CAT-doping auf diesen Materialien ist bisher nicht klar.

Zusammenfassung

Dementsprechend bestand das erste Ziel dieser Arbeit darin, die Wirksamkeit der CAT-doping auf diesen Materialien hinsichtlich der elektrischen und optischen Eigenschaften zu nutzen. In der Zwischenzeit wurde ein tieferes Verständnis des Mechanismus der CAT-doping in verschiedenen Materialien abgeleitet. Es wird gezeigt, dass P Atome effektiv in diese Filme eingebaut werden können, jedoch mit unterschiedlichen P-Atom-Konzentrationen (N_{P}) und Dotierungstiefen. Bei a-Si:H Filmen kann der N_{P} aus CAT-doping bis zu $6 \times 10^{21} cm^{-3}$ mit einer Dotierungstiefe um 15 nm betragen, während bei μc-Si:H der N_{P} $6 \times 10^{20} cm^{-3}$ mit einer Dotierungstiefe von 5 nm erreichen kann. Bei nc-SiO_x:H Filmen liegt der N_{P} ebenfalls im Bereich von $10^{20} cm^{-3}$, aber P Atome dringen durch den gesamten Film. Wenn es um μc-SiC:H Filme geht, beträgt N_{P} nur $6 \times 10^{19} cm^{-3}$ und P-Atome scheinen sich an die Oberfläche von μc-SiC:H Filmen zu binden. Der Unterschied im Verhalten der CAT-doping wird auf die Mikrostrukturen dieser Siliziumlegierungen zurückgeführt. Die lockere Struktur von a-Si:H, wo eine große Anzahl von Hohlräumen und Defekten vorhanden ist, führt zu einem großen N_{P} und einer tieferen Dotierungstiefe für a-Si:H. Die Korngrenzen in μc-Si:H tragen auch dazu bei, mehr P-Atome einzubauen. nc-SiO_x:H hat eine sehr einzigartige poröse Käfigmikrostruktur, die einen Kanal für P-Atome bietet, um den gesamten Film während des CAT-doping prozesses zu durchdringen. Im Gegensatz dazu verhindert die dichte Mikrostruktur von μc-SiC:H, dass P-Atome eindringen und sich nur an der Filmoberfläche festsetzen.

Das zweite Ziel war die Verbesserung der Passivierungsqualität verschiedener Zellvorläufer und -vorrichtungen. Zunächst wurden während des CAT-doping prozesses verschiedene Gase verwendet, und es wurde festgestellt, dass drei Effekte (d. H. Thermisches Tempern, Hydrierung und P-Dotierungseffekt) zur Verbesserung der Passivierungsqualität nebeneinander existieren. Dann wurden Zellvorläufer und Vorrichtungen mit diesen Siliziumlegierungsfilmen mit CAT-doping behandelt und ihre Passivierungsqualität wurde in unterschiedlichem Ausmaß verbessert, was teilweise auch mit der Änderung der Materialeigenschaften bei Anwendung des CAT-doping verfahrens zusammenhängt.

Das ultimative Ziel ist es schließlich, CAT-doping in SHJ-Solarzellen zu implementieren. Im Allgemeinen führt das Aufbringen von CAT-doping auf die verschiedenen

dotierten Schichten an der Vorderseite von SHJ-Solarzellen zu einem verbesserten Wirkungsgrad, der hauptsächlich auf verbesserte V_{oc} und FF Werte zurückzuführen ist. Es wurde festgestellt, dass die Filamenttemperatur (T_{f}), die Substrattemperatur (T_{sub}) und der Verarbeitungsdruck die Effizienz beeinflussen, und es wurden lokale optimale Werte identifiziert. Die Änderung der elektrischen Eigenschaften für nc-SiO_x:H ist jedoch aufgrund der geringen Aktivierung von P-Atomen mit eingebautem Cat-doping begrenzt. Der Einfluss vor katalytische Dotierung auf die Effizienz von Zellen mit nc-SiO_x:H war nicht offensichtlich. Über die traditionelle Struktur von SHJ-Zellen hinaus wurde ein neues Herstellungsverfahren vorgeschlagen, bei dem die Abscheidung einer a-Si:H(n) -Schicht durch CAT-doping auf einer a-Si:H(i)-Schicht ersetzt wurde. Im Vergleich zu herkömmlichen SHJ-Zellen wurde eine äquivalente Effizienz von Zellen mit neuer Struktur erreicht und weist eine Zunahme von $\sim 1 mA/cm^2$ in J_{sc} auf. Basierend auf diesem Konzept wurde durch Hinzufügen einer zusätzlichen a-Si:H(n)-Schicht zur Front eine Champion-Effizienz von 21,2% erreicht, wobei der FF im Vergleich zur herkömmlichen SHJ-Zellstruktur hauptsächlich um 4,9% zunahm.

1 Introduction

Upon the awareness of environment protection and desire for sustainable development, photovoltaic (PV), as one of the mainstream renewable energies, has largely drawn attention from the public and been politically supported by governments worldwide. According to the latest report [1], renewable energy accounted for 72% of the total energy capacity expansion in 2019 and PV has a share of ∼56% in the newly added renewable capacity. Meanwhile, another report also pointed out that there is a widening gap between rhetoric and action which jeopardize the completion of cutting carbon dioxide (CO_2) emission in the coming decades [2]. Despite the fast growing market of PV and subsides from governments, the levelized cost of electricity (LCOE) of PV is still not as low as conventional fossil fuel energy and this prevented the bigger explosion of PV market. To embrace a larger share of PV in energy market, new PV modules with higher efficiency and lower cost are needed.

Among many innovative PV techniques, silicon heterojunction (SHJ) solar cells are one of the most promising candidates for the next-generation high-efficiency mainstream PV technology due to their high efficiencies and simple production sequences [3]. In a SHJ solar cell, an intrinsic hydrogenated amorphous silicon (a-Si:H(i)) thin film is usually used to achieve excellent surface passivation quality. Doped a-Si:H layers are used as emitter or surface field layer [3–6]. SHJ solar cell efficiency over 23% has been achieved for mass production [7]. However, there is still optical loss from the parasitic absorption in solar spectrum range due to the use of doped a-Si:H layers at the front side [3, 8] as well as loss from the lower conductive a-Si:H layers. Silicon alloy thin-films, like microcrystalline silicon (μc-Si:H), nanocrystalline silicon oxide (nc-SiO_x:H) and microcrystalline silicon carbide (μc-SiC:H) [9–11], are very promising alternatives to be used in a SHJ solar

cell to reduce the contact resistance and parasitic absorption due to their higher conductivity and lower absorption coefficient in short wavelength range.

Beside the implementation of silicon alloys, catalytic-doping (Cat-doping) has the potential to further improve electrical properties of silicon alloy films and their interfaces. Cat-doping is a cheap, simple and up-scalable post-deposition treatment, which is based on hot wire chemical vapor deposition (HWCVD) technique. During a Cat-doping process, the gas molecules are decomposed at the hot surface of catalyzing wires, then the decomposed radicals diffuse radially towards the sample and penetrate into the surface of silicon films forming a shallow depth doping layer with a thickness of 5-15 nm [12, 13]. With Cat-doping, material properties, e.g. conductivity and doping concentration, could be tuned beyond the level which is achievable for as-grown films [13, 14]. Especially for materials, where the conductivity is limited upwards due to restrictions from process boundary conditions during film depositions or from trade-off with other device relevant material properties, the Cat-doping process might be beneficial to overcome the limit or find better trade-off regime.

So far, Cat-doping has been studied mainly on crystalline silicon (c-Si) and amorphous silicon (a-Si:H) [12, 13, 15, 16]. Former studies have shown that Cat-doping could improve the conductivity of a-Si:H and change the doping type of n- and p-type wafers. Cat-doping could also improve the passivation quality when applied on the surface of c-Si wafer in a symmetrically passivated sample. However, the effectiveness of Cat-doping on different silicon alloy films is still unclear and impact on passivation quality when applied on different interfaces in passivated samples or cells is also unknown. The ability of Cat-doping to improve the efficiency of SHJ cell containing silicon alloy films in the front is yet to explored.

Therefore, the goal of this thesis is to expand the study of Cat-doping to more materials, here specifically on silicon alloys that can be used in the front of SHJ cells to advance the device performance. To achieve this goal, several scopes are included: firstly the effectiveness of applying Cat-doping on silicon alloy films to improve the material properties; secondly the enhancement of passivation quality

when Cat-doping is implanted onto different interfaces and ultimately the probability of Cat-doping to lift the efficiency of SHJ solar cells. These contents are divided into different chapters and following is a brief description of the content in each chapter.

Chapter 2 contains motivation to use various silicon alloys in SHJ solar cells and problems remaining when implanting these silicon alloys into SHJ solar cells. A short introduction of Cat-doping is also given. In detail, Sec. 2.1 gives a brief introduction on SHJ solar cells and points out the problems faced SHJ solar cells on its way to higher η. Sec. 2.2 introduces several silicon materials used in this work including their advantages and trade-offs when used in SHJ solar cells. Sec. 2.3 gives a short summary on the history of Cat-doping and its development so far.

In **Chapter 3**, details on sample preparation and characterization methods are given. Sec. 3.1 describes the methods used in this work to prepare silicon alloy films as well as cells containing these silicon alloys. Most of the films were produced with plasma enhanced chemical vapor deposition (PECVD), except that μc-SiC:H films were deposited with hot-wire chemical vapor deposition (HWCVD). Sec. 3.2 contains details of various methods used to characterize the material properties of silicon alloy films. In Sec. 3.3 describes the systems used to estimate passivation quality and the performance of SHJ solar cells.

The development and effectiveness of Cat-doping on various silicon materials are discussed in **Chapter 4**. This includes Cat-doping on four silicon materials, i.e. a-Si:H, μc-Si:H, nc-SiO_x:H and μc-SiC:H. Intrinsic and doped materials are both studied. In Sec. 4.1, a prepositive study of Cat-doping on glass and silicon films was conducted to exclude the influence from possible film deposition during Cat-doping process. Sec. 4.2 gives a brief introduction of possible radical movements during Cat-doping process. In Sec. 4.3, Cat-doping on μc-Si:H is discussed. Here, intrinsic, n- and p-type μc-Si:H films were used and Cat-doping was found effective for all. In Sec. 4.4, Cat-doping on a-Si:H is discussed and various parameters of Cat-doping were used to have obvious impact on the significance of Cat-doping. Sec. 4.5 presents the results of Cat-doping on nc-SiO_x:H with various O contents. Sec. 4.6 discusses Cat-doping on μc-SiC:H by comparing μc-Si:H with nc-SiO_x:H. In Sec. 4.7, a

comparison is given on Cat-doping into different silicon alloys for a deeper insight of the mechanism of Cat-doping. It is found the difference might be related to material composition and microstructure. Sec. 4.8 describes the change in optical property for silicon alloy films after Cat-doping.

Passivation quality after Cat-doping treatment on different interfaces is an important issue before implanting Cat-doping into cells and is discussed in **Chapter 5**. In Sec. 5.1, three effects during Cat-doping were identified using different processing gases. Sec. 5.2 discussed the effectiveness of Cat-doping to improve the passivation quality upon using on different silicon alloy film surfaces in passivated samples.

In **Chapter 6**, Cat-doping was implanted into SHJ solar cells containing different silicon alloy films and various methods were tested to optimize the device performance. Sec. 6.1 gives an introduction of reference cell used for this work and this is the base of other cell optimization. In Sec. 6.2, Cat-doping on different silicon alloy films in SHJ solar cells is shown to improve the efficiency. Sec. 6.3 presents performance of cells with μc-Si:H(n) in the front side of cells with optimization in Cat-doping parameters. Sec. 6.4 discusses the effect of Cat-doping on cells with nc-SiO_x:H in the font. In Sec. 6.5, a new approach is proposed for conventional SHJ solar cells and has been proven to be significantly effective in improving cell performance.

In **Chapter 7**, conclusions of this thesis are summarized and an outlook is given for future study of Cat-doping and its impact on SHJ solar cells.

2 Fundamentals and literature review

In this chapter, fundamentals of SHJ solar cells and current research topics are presented. The history of Cat-doping and existing studies on Cat-doping are also included.

2.1 Silicon heterojunction solar cells

Silicon heterojunction (SHJ) solar cells are widely studied both in laboratory and industry levels for their high efficiency, simple fabrication procedure and low cost [3, 7, 17–20]. A record η of 25.1% was achieved by both-sides contacted SHJ solar cells and an even higher η of 26.7% was achieved when SHJ was used in interdigitated back-contacted solar cells [4, 5, 21, 22]. Meanwhile, SHJ solar cells have also been combined with other types of cells, such as used as bottom cell in perovskite/c-Si tandem solar cells, for high efficiency [23, 24].

Commonly, a SHJ cell consists of a c-Si wafer passivated by a-Si:H(i) with a thickness of a few nanometer. Then doped a-Si:H layers are deposited on both sides as emitters or surface field layers, TCO layers and Ag grids are subsequently prepared on the top of a-Si:H stacks. By inserting the a-Si:H stacks, the highly recombination-active metal contacts are lifted away from the c-Si surface. Then, misalignment of the band diagrams from c-Si and a-Si:H creates band offsets in conduction band (Ec) and valence band (Ev) and repels the minority carrier from moving to the defect-rich a-Si:H(i)/c-Si interface [25]. Moreover, the a-Si:H(i) significantly reduces the surface state density of c-Si by introducing hydrogen to saturate the silicon dangling

bonds (DB). All in all, the c-Si surfaces are well passivated and recombination is significantly reduced, enabling impressive high iV_{oc} in this heterojunction structure [5].

However, despite the above-mentioned advantages in SHJ solar cells, there are still some limits that prevents SHJ solar cells from getting closer to the theoretical limit efficiency. [4, 5, 21]. The first one is the parasitic absorption form the a-Si:H layers, which causes 3.4% loss [21] in the current record cell and even more in many other cells [3, 8, 17, 19, 26]. Studies and measures have been done to analyze and minimize the optical loss from the a-Si:H layers [27–30] and transparent emitter materials were tested in SHJ solar cells to have more gains in front-side absorption [6, 9–11, 31–35].

The second limit relates to the electrical isolation of the passivation a-Si:H(i) layers with low conductivity. Usually, a-Si:H(i) layers thicker than 5 nm are needed on both sides of the c-Si surface for good passivation. However, a 5 nm a-Si:H layer is too thick for carriers to tunnel through and is detrimental to electrical transport. In the end, this 5 nm a-Si:H(i) acts as an obstacle for achieving higher FF [4, 27]. Therefore, the trade-off between good passivation and good FF must be overcome to achieve higher efficiency.

2.2 Silicon alloys

Among many materials, μc-Si:H, nc-SiO$_x$:H and μc-SiC:H are promising candidates to replace the a-Si:H(n) layers in the front of SHJ solar cells for better electrical property and better optical absorption in the short wavelength range.

Amorphous silicon Intrinsic a-Si:H layer is commonly used in SHJ solar cells for c-Si surface passivation layer and doped a-Si:H layers are used as emitters or surface field layers. The a-Si:H/c-Si hetero structures were first studied by Fuhs et al. in 1974 [36] and showed excellent passivation ability later [37]. SHJ solar cells have been fabricated but showing modest FF due to large interface state density [38]. A breakthrough was made by introducing a thin buffer layer of a-Si:H(i) on c-Si, which

was called Heterojunction with Intrinsic Thin-layer (HIT) structure and patented by Sanyo (later bought by Panasonic) [39]. This thin buffer layer of a-Si:H(i) benefits the V_{oc} and very high value has been achieved ever since [21].

However, the a-Si:H layer stacks used in the front of the cell also introduce large parasitic absorption. The isolating a-Si:H(i) layer also results in high series resistance that reduces the FF. For instance, even in several world records of SHJ solar cells, the parasitic absorption and high resistance have been pointed out to be the obstacles for higher η [4, 21, 40]. Many researches in SHJ solar cells were focused on the optimization of the a-Si:H layer and replacement of a-Si:H thin films. In this work, mainly three silicon alloy materials (i.e. μc-Si:H, nc-SiO_x:H and μc-SiC:H) are studied and discussed. In the following sections, brief introduction of these three silicon alloys are given.

Microcrystalline silicon (μc-Si:H) is an appealing alternative for the front a-Si:H carrier selective contacts because the conductivity of μc-Si:H can be considerably higher than that of a-Si:H, thus it is beneficial to reducing series resistance (R_s). In addition, μc-Si:H has lower absorption coefficient (α) at short wavelengths which leads to lower parasitic absorption. In the early days, μc-Si:H was studied mostly to be used in thin film cells [41–43]. Then, μc-Si:H was applied in silicon heterojunction since 1996 [44]. Due to the limitation of PV technology at that time, very low η was obtained [9]. However, as the SHJ solar cell technologies were further developed, doped μc-Si:H showed exciting potentials for its better electrical conductivity and lower absorption coefficient as compared to a-Si:H [44–47]. Meanwhile, the material properties of μc-Si:H, such as optical absorption, electrical transport, defects and growth mechanism, have been deeply studied [43, 48–53]. It has also been shown that μc-Si:H is a better contact material to TCO than a-Si:H [54–57].

Despite the advantages of μc-Si:H in optical and electrical properties, there are still challenges when integrating μc-Si:H into SHJ solar cells. Compared to the micrometer thickness μc-Si:H in thin-film solar cells, the thickness of μc-Si:H in a SHJ cell is usually 10 nanometer or less. This thin thickness raises challenges to the deposition condition and the quality of μc-Si:H. Firstly, the incubation layer for

μc-Si:H should be as small as possible so to reach crystalline phase and gain in light absorption and electrical transport [43]. Secondly, the deposition of μc-Si:H may deteriorate the passivation of a-Si:H(i) beneath [58]. Thirdly, the Raman crystallinity (χ_c) should be sufficiently high for good optical and electrical property. Furthermore, it should be noted that the boron doping inhibits the crystalline growth and hinder the nucleation of μc-Si:H(p) layers [59, 60], so special care should be taken if p-type μc-Si:H is to be used. To solve these problems, efforts have been taken to reduce the incubation layer thickness, preserve the passivation and speedup the incubation process for high χ_c [61–64].

Nanocrystalline silicon oxide (nc-SiO_x:H) films consist of three different phases, i.e. a-Si:H phase, μc-Si:H phase and SiO_x phase. This multi-phase microstructure offers possibilities to easily tune the electrical and optical properties of the films via varying the deposition parameters, such as O and H content. Varying the CO_2 gas ratio in the deposition gas is a common way to tune the O content and change the portion of SiO_x phase inside the film. With variation in the portion of these three phases, the microstructure of nc-SiO_x:H film can be changed as well as the electrical and optical properties. In general, when increasing the CO_2 ratio in the gas source, the portion of SiO_x increases in the film, thus makes the film more transparent and less conductive.

The nc-SiO_x:H used in this work was initially developed by Ding et. al. for the use in quantum dots and SHJ solar cells [31, 65–68]. Then more details about nc-SiO_x:H was studied in terms of microstructure, doping and application by Richter et. al. [10, 69–71]. There is always a trade-off between the optical band gap (E_{04}) and the dark conductivity (σ_D), even through careful adjustment of the deposition parameters can benefit the trade-off to some extend. With detailed investigation, the films were divided in four distinct deposition regions: (1) the "fully amorphous" region, (2) the "onset of nc-Si formation" region, (3) the "O and nc-Si enrichment" region and (4) the "nc-Si deterioration" region [72]. The optimal deposition region for cells was identified between the (3) and (4) region. Meanwhile, study of the microstructure by TEM and APT reveals the phase distributions in the films, which confirms the anisotropic growth of nc-Si:H. A 3D network of electrically conductive nc-Si:H

and transparent O-rich a-SiO_x:H was observed and a nearly uniform distribution of the dopant atoms across different phases was also found in both p- and n-doped nc-SiO_x:H films.

Microcrystalline silicon carbide As mentioned in Sec. 2.1, optical loss in the front is always a hold-back for efficiency of SHJ solar cells, thus good front window layers are needed. Similar to nc-SiO_x:H, μc-SiC:H is also a wide band gap (2.2-2.4 eV) [73] material that can be used in the front of SHJ solar cells to achieve excellent light transmission. In terms of microstructure, μc-SiC:H consists of crystalline silicon carbide grains that are within the size of micrometers. The research on this material has been done mainly in several aspects. The first one is the doping mechanism, where nitrogen, oxygen and phosphorous are well-known dopants for n-type doping of μc-SiC:H and aluminum, boron and gallium are well-known acceptors for p-type doping of μc-SiC:H [74]. More interestingly, μc-SiC:H presents to be n-type doped even without doping gas during deposition, which is the so-called unintentionally n-doping [75–77]. This unintentionally doping was later referred to the uncontrolled doping from ionized nitrogen [74]. However, oxygen located at the grain boundaries was also argued to provide donors [76, 78]. More detailed study about the doping mechanism was carried out by Pomaska et. al [73]. It was found that the oxygen increases the conductivity of μc-SiC:H mainly due to the lowering of potential barrier height at the grain boundaries and the nitrogen increases the conductivity by increased charge carrier density and charge carrier mobility [73].

Apart from the doping mechanism in μc-SiC:H, the implementation of μc-SiC:H into SHJ solar cells is also an important issue that needs to be solved. In SHJ solar cells, a thin a-Si:H(i) layer is a commonly used passivation layer on c-Si wafer surface. However, when depositing μc-SiC:H on the top of a-Si:H(i) layer, the high H density in deposition process leads to etching into the c-Si surface and deteriorate the passivation quality [79–81]. To overcome this limitation, different approaches have be proposed and tested, such as adding a thin amorphous SiC buffer layer between the substrate and μc-SiC:H layer [79, 81] and replacing the a-Si:H(i) layer by a thin a-SiO_x:H layer or SiO_2 layer to significantly reduce the etching of c-Si surface. [82,83]. Here, the layers are prepared by HWCVD due to its lower H etching compared to

that in PECVD.

The μc-SiC:H films used in this work was initially developed by Pomaska et. al. [73]. The opt-electrical properties of μc-SiC:H are closely related to the deposition conditions during the HWCVD process and the key parameter is the filament temperature (T_f). As shown by Köhler et. al. in Figure 2.1, the conductivity of μc-SiC:H(n) increases as the increase of T_f during HWCVD process. However, the increase of T_f leads to severe H etching from the decomposed gas radicals and reduces the passivation quality. Thus, there is also a trade-off for μc-SiC:H films when implemented into SHJ solar cells. The optimal T_f has been found to be around 1750 °C in terms of passivation quality [84]. To overcome the trade-off between the conductivity and passivation quality, Cat-doping was proposed in this work and more details will be discussed in Chapt. 4 and 5.

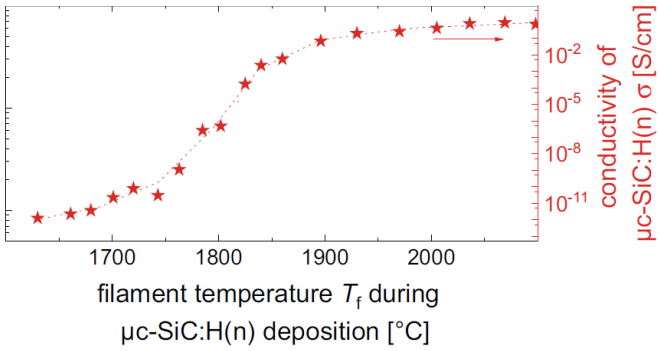

Figure 2.1: *Conductivity of the μc-SiC:H(n) as a function the filament temperature (Tf). Reproduced from Ref. [84] with permission.*

2.3 Catalytic-doping

The Cat-doping phenomenon was first accidentally discovered by Matsumura group and reported in 2011 [85, 86]. During one hydrogenation treatment process to improve the passivation quality of SHJ solar cells, they used a-Si:H(n) deposition chamber instead of a-Si:H(i) deposition chamber and found that the charge carrier

lifetime increased drastically. Later, SIMS results confirmed that P atoms from the a-Si:H(n) chamber were incorporated into c-Si [12, 87]. With deeper studies, they found that Cat-doping happens even at substrate temperature (T_{sub}) as low as 80 °C [12], which is much lower compared to thermal diffusion in c-Si. This indicates a different doping mechanism might exist for Cat-doping. In the following, an overview is given about the reported studies on Cat-doping.

Material property modification Cat-doping is essentially a post-deposition doping method that uses different types of dopants to change the electrical properties, such as conductivity, of silicon thin films. Beyond that, different side-effects were also brought in either with the change of electrical property or with the HWCVD process itself. One of the interesting abilities of Cat-doping is changing the type of an initially doped substrate via compensation doping. For instance, Figure 2.2 shows the carrier density of c-Si wafers as a function of T_f. In Figure 2.2(a) the Cat-doping was done on p-type wafer with phosphorous (P) Cat-doping, when T_f was increased above 1000 °C, the result shows a conversion from p-type to n-type. Similarly in Figure 2.2(b), when boron (B) Cat-doping was applied on n-type wafer, the conversion from n-type to p-type also happened but with lower T_f or just with T_{sub}=350 °C. The possible reason of lower requirement for B Cat-doping is that diborane (B_2H_6) is much easier to crack than phosphine (PH_3). More details can be found in Ref . [12]. Besides study on c-Si wafers, applying Cat-doping on a-Si:H also results in an increase of conductivity up to 4 orders of magnitude [13].

Secondary ion mass spectrometry (SIMS) results confirmed the incorporation of these two dopants (B and P) into c-Si wafers and a-Si:H films with a doping depth slightly varying from 5 to 10 nm [12, 13, 86, 88]. Here, doping depth is defined from the P concentration peak at the surface to the point where the curve meets the detection limit of SIMS. Usually, the doping mechanism could be indicated by the shape of doping profile (error function (*erfc*) indicates conventional diffusion with unlimited source and *Gaussian* indicates ion implantation). However, the P profile after Cat-doping cannot be distinguished between *erfc* and *Gaussian* due to the shallow doping depth. Thus, the doping mechanism is still an open question.

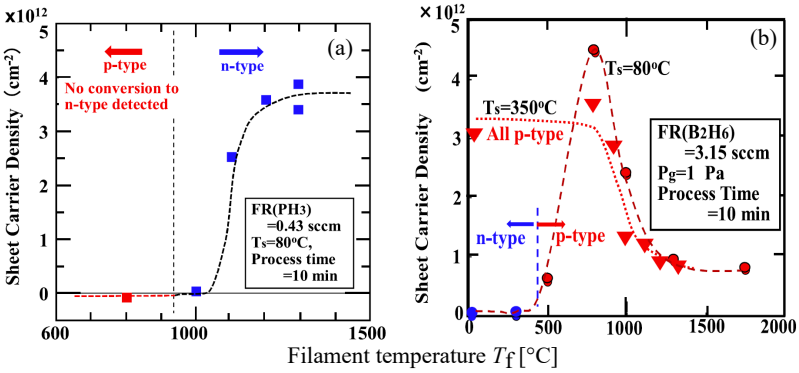

Figure 2.2: *Sheet carrier density of c-Si as a function of T_f for (a) P Cat-doping on p-type wafer and (b) B Cat-doping on n-type wafer with two substrate temperatures (T_{sub}). Reproduced from Ref. [12] with permission.*

Passivation quality improvement Beyond the increase in conductivity, the passivation of a SHJ cell or cell precursor was also found to be improved when Cat-doping was performed prior to the deposition of passivation layers. Matsumura group successfully improved the passivation quality with Cat-doping on c-Si wafers [16, 89]. The local optimal T_f has also been found around 900 to 1300 °C, as too high T_f would cause severe H etching and create damages at the c-Si surface. After Cat-doping process, the surface recombination velocity (SRV) is estimated to be ∼6 cm/s with a minority charge carrier lifetime (τ_{eff}) of 2.4 ms [16], which is much higher than the 1.4 ms from the sample without Cat-doping. Simulation by Afros-HET of the band diagram shows that the barrier height at the c-Si surface and a-Si:H passivation layer is reduced by 88 meV [16]. This reduction in barrier height enhances the backward of electron flow, thus decreases series resistance (R_s) and improves the fill factor (FF).

So far, Cat-doping was applied only on c-Si wafers and a-Si:H films. There still lacks of study on other materials, such as different silicon alloys that could be used in SHJ solar cells for their outstanding electrical or optical properties. The doping mechanism is yet to be clarified, the improvement in passivation quality on more structures and different materials still needs to be studied. It is specially

promising for materials with trade-off between electrical and optical properties, since Cat-doping is able to further tune the electrical property after film deposition and might achieve a better trade-off point. In this work, more silicon alloy materials will be studied in detail and it will be discussed in Chapt. 4. Meanwhile, apart from applying Cat-doping on c-Si surface, Cat-doping will also be performed on other interfaces of SHJ cells or cell precursors to test its ability to improve passivation quality, which will be discussed in Chapt. 5. Furthermore, SHJ solar cells with different silicon alloy films were made and Cat-doping was implemented to validate the improvement in device performance, this will be dicussed in Chapt. 6.

3 Experimental details

In this chapter the experimental methods used to prepare and characterize the materials and solar cells are introduced. The first section describes the systems and sequences used to fabricate material samples and solar cells in this work. The second section lists all the techniques for characterization of material properties as well as a brief description of their principles. The last section gives an overview of methods for evaluation of solar cells.

3.1 Materials and solar cells fabrication

Plasma enhanced chemical vapor deposition (PECVD) is a commonly used chemical vapor deposition technique to prepare thin films. The main components of a PECVD system are a vaccum chamber, two adjecent electrodes with external power generators, temperature control and gas inlet system. A sketch is given in Figure 3.1(a). Normally alternating current (AC) generators with different frequencies are used to provide alternating electrical field between two electrodes. The rapidly changing electrical field creates plasma between the electrodes. When gas precursors are supplied, the gas molecules are decomposed between two electrodes and the decomposed radicals then bond to the substrate forming thin films. Details about the deposition condition can be found in Ref. [90, 91].

Hot wire chemical vapor deposition (HWCVD) also belongs to the chemical vapor deposition (CVD) family. Instead of using plasma in PECVD, HWCVD uses hot filaments (aslo called catalyzers) to crack the gas molecules. Thus, HWCVD is alternatively called Catalytic-CVD (Cat-CVD). In the vacuum chamber of a HWCVD system, the electrodes are replaced by filaments, as illustrated in Figure

3.1(b). Commonly used filament materials in HWCVD are tungsten (W), tantalum (Ta), ceramic, graphene and so on. For all the Cat-doping processes in this work, three curled Ta filaments with a diameter of 0.5 mm and an original length of 15 cm were used. If not specified otherwise, the distance between substrate and filament was 90 mm, the heater temperature was set to 200 °C and pressue during the catalytic-doping (Cat-doping) was set to 0.01 mbar. The filament temperature (T_f) were changed from 700 °C up to 2200 °C. Phosphine (2% PH_3 diluted in helium) was used with a gas flow rate of 20 sccm and the process duration was kept at 10 mins for sufficient doping.

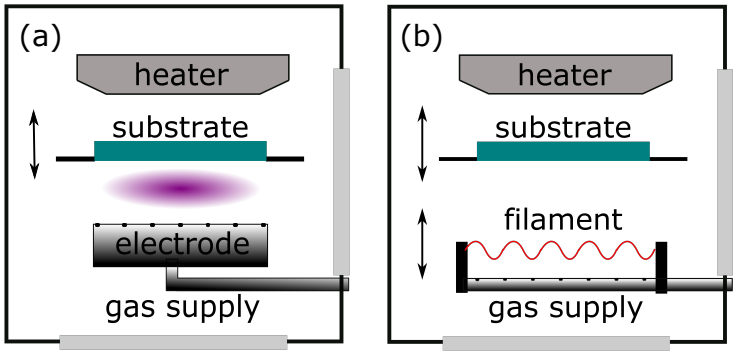

Figure 3.1: *Apparatus sketch of (a)PECVD and (b)HWCVD systems*

Ion implantation is a common technique to implant desired impurity ions into solid materials. The system usually consists of an ion source, an accelerator and a target chamber where the ions are implanted. Ions are accelerated electrostatically to a high velocity and impinge to the target, realizing impurity doping. Due to the high energy ions, this method normally cause the physical and chemical properties of the target to change, amorphization is a very common phenomenon due to the damage in crystalline structure. A free software called Stopping and Range of Ions in Mass (SRIM) is used to simulate the distribution of ions at different energy and dose. In this work, ion implantation and SRIM were used to produce standard samples which act as calibration reference in SIMS measurement. The reference samples were initially intrinsic silicon alloy films and were implanted with P atoms.

Magnetron sputtering is a physical vapor deposition (PVD) technique. The principle of magnetron sputtering is that in a high vaccum chamber, electrons move quickly under electrical field and collide with argon molecules (Ar), creating plasma by ionization of Ar. Charged Ar radicals then accelerate towards the target and bombard the target composition out. Then the target radicals travel to the substrate forming thin films. Magnetic field combined with electrical field inside the chamber makes electrons move in circles, this increases the collision rate with Ar thus increase the deposition rate of magnetron sputtering. In this work, magnetron sputtering was used to deposit indium tin oxide (ITO) as a transparent conductive oxide (TCO) layer. A typical recipe used was: an ITO target with 5 wt. % tin oxide (SnO_2), substrate temperature set to 125 °C, 27 sccm Ar mixed with 3 sccm oxygen (molecular oxygen (O_2) diluted to 1% in Ar) at a p of 4.7×10^{-3} mbar. The substrate rotated at 5 rpm.

Thermal evaporation also belongs to PVD family. The target material is heated in a boat, usually made with W, to vapor phase. Under the high vacuum condition, the mean free path is large enough for evaporated molecules to travel to the substrate. A piezoelectrical crystal was used to characterize the deposition rate by monitoring the vibration frequency change from deposition of films. In this work, a W boat was used to evaporate silver (Ag) for different metal contacts. For example, co-planar contacts were fabricated by evaporation with a layout of 5 mm long, 3.5 mm wide, 700 nm thick and 0.5 mm apart from each other. Some metal contacts for solar cells were also prepared by evaporation.

Screen printing is currently a dominate metallization process in the PV industrial for its simplicity. Figure 3.2 shows (a)the screen with patterned opening and (b) complete cell with contacts made by screen printing. Screens with certain opening are specially designed for both front and back side. The silver paste is forced through the screen with pattern meshed and bonds to the substrate. Then the samples are annealed in the oven at around 200 °C to get rid of the organic binders in the paste.

Solar cell fabrication An overview of the solar cell fabrication procedure is shown in Fig. 3.3. Double side textured n-type crystalline wafer (c-Si) with an orientation

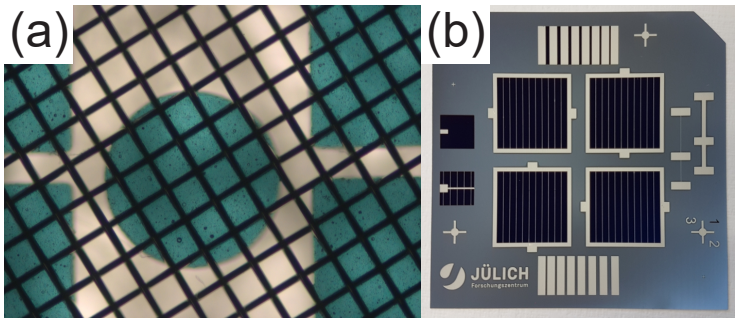

Figure 3.2: *Screen printing (a) close view of the screen with patterned opening and (b) complete cell with contacts prepared by screen printing*

of (100) was first cleaned wtih standard cleaning process developed at Radio Corporation of America (RCA), followed by a HF immersion. Then shortly the wafer was moved into PECVD system for the deposition of a-Si:H(i) passivation layers and doped layers on both sides. After the deposition of silicon thin films, ITO films were prepared on the stacks by magnetron sputtering. The last step was making Ag contacts either by thermal evaporation or screen printing. The complete cell was then annealed at a temperature varying from 170 to 220 °C.

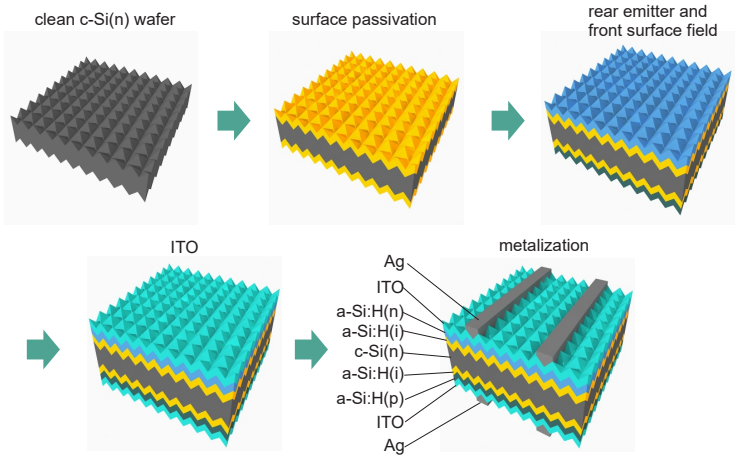

Figure 3.3: *a typical SHJ solar cell fabrication procedure*

3.2 Material characterization

Thickness. A step profiler (Vecco DEKTAK 6M Stylus Profiler) was used to determine the thickness of a sample. A probing tip was used to scan across the sample surface and then determine the step between the substrate and film. The step between the substrate and film was usually created by making a mark on the substrate before deposition and removing it after deposition. The mark can be done with stick tapes or marker pens (which can be removed by IPA).

Conductivity. The lateral conductivity of a thin film sample was measured by using a co-planar contacts with the layout is described in Sec. 3.1. The measurement was usually done in the dark, at room temperature and in air atmosphere. A scan in a voltage range between -100 $\sim$ +100 V was first performed to monitor the ohmic contact between the sample and measuring probes, also the current range was checked not to exceed the up limit of 1 mA. The conductivity was then calculated by Eq. 3.1.

$$\sigma = \frac{I}{V}\frac{w}{dl} \tag{3.1}$$

where w is the distance between the Ag contacts, l is the Ag contact length and d is the thickness of the film.

Spectrophotometry is a quantitative method to measure the interaction of a thin film with light as a function of wavelength (λ). A UV-vis-NIR spectrophotometer (Perkin Elmer LAMBDA 950) was used in this study to measure the total spectral reflectance (R) and transmittance (T). The samples were usually prepared on glass substrates and measured in a wavelength range of 300-1500 nm, which is the most relevant range for silicon solar cells. The absorption coefficient (α) is determined by Eq. 3.2.

$$e^{\alpha d} \approx \frac{T}{1-R} \tag{3.2}$$

Photothermal deflection spectroscopy (PDS) is another method to derive the absorption coefficient (α) of thin film samples, but with much higher sensitivity. The sample is immersed in a liquid medium (typically carbon tetrachloride(CCl_4)), for

which the refractive index (n) changes with temperature. Two light beams are used during the measurement, one monochromatic light is directed towards the sample and one probing laser beam is in parallel to the sample surface. The absorption of the monochromatic light in the sample leads to a rising temperature and heats up the surrounding liquid. The n changes proportionally due to the heating and cause a deflection of the laser beam, which is then used to determine the absorption coefficient of the film. For a measurement performed by spectrophotometry, the absorption is usually derived from the difference of signals that are in large numbers and this makes the accuracy poor when the absorption is small. For measurement by PDS, the deflection signal is proportional to absorption making PDS more accurate method at low absorption. In this study, both spectrophotometry and PDS were used to determine the light absorption of thin films. PDS is more often used for low energy range absorption where the free charge carrier absorption happens.

Raman spectroscopy observes vibrational, rotational and other low-frequency modes in a system to identify molecules and their structures. When a light is applied on a sample, the Raman effect happens in form a inelastic scattering where the sample is excited by photons. The excitation puts molecules in the sample to a virtual energy state shortly before the photons are emitted, but to a lower or higher energy states. This is called Stock shift and Anti-Stock shift, respectively. The polarizability changes as Raman effect occurs and the intensity of Raman spectrum is proportional to the polarizability change. Therefore, by detecting the intensity of Raman spectrum, different rovibronic states of the molecules can be quantitatively identified to reveal the complex composition of the material. For silicon based material, due to the difference in Si-Si bond angels and length in amorphous phase, the transverse optical mode of the Si-Si vibration shifts from sharp 520 cm^{-2} peak to a broad peak around 480 cm^{-2}. In this study, a Renishaw inVia Raman Microscope was used to determine the crystalline volume fraction in the films. A laser with 532 nm wavelength was used and the power was set to 1.2 mW. After the measurements, the data was evaluated by a home-developed program for the value of crystalline volume fraction.

Atom probe tomography (APT) is a destructive method that offers both 3D imaging and chemical composition measurements at atomic scale. The sample should be prepared as a sharp tip and cooled down during measurement so atoms stay in one place. High voltage is introduced at the small radius of the tip and very high electrostatic field is created, which is just below the point of atom evaporation. Upon applying laser or voltage pulse, atoms are evaporated from the tip surface and been collected at the position sensitive detector. Meanwhile, the use of time-of-flight spectrometer identifies the species of the atoms. In this way, the 3D image of interested atoms could be reconstructed to analyze possible microstructure and segregation of thin films.

Secondary ion mass spectrometry (SIMS) is a powerful tool to analyze the composition of solid materials with good depth resolution. First the target is sputtered with primary ions (commonly used are oxygen (O^+) and cesium (Cs^+) ions) and the charged secondary ions are ejected from the surface, then the secondary ions are collected and identified in a mass spectrometer. In this study, the SIMS was used to determine the distribution profiles of P, Si, O, B and H atoms. For every SIMS sample, a 15 nm a-Si:H(i) was deposited on top of the samples as a diffusion barrier for sputter ions and a buffer layer for unstable etching plasma at the beginning of the measurement [92]. Relative sensitivity factor (RSF) was obtained by using the reference from ion implanted samples for different silicon alloys. The measurements were performed in the Central Institute for Engineering, Electronics and Analytics (ZEA-3), Forschungszentrum Jülich, more details can be found in Ref. [65].

Electrochemical capacitance voltage (eCV) is often used to measure the active carrier concentration profiles in semi-conductor films. By forming Schottky contact between the electrolyte and semiconductor films, a depletion region is created where no free electrons and holes exist thus behaves like a capacitor. The carrier concentration then can be derived by measuring the capacitance. It should be noted that the carriers come from not only doping but also other aspects, such as electrically active defects and traps. Depth profiles of carrier concentration can be obtained by electrolytically etching of the semiconductor and repeated capacitance measurements. A sketch of the electrochemical cell is shown in Figure 3.4 [93]. The sample

is pressed against a small sealing ring,through which the sample gets contacted with the electrolyte in the teflon made cell. A saturated calomel electrode is used as a reference to measure the applied potential between the semiconductor and electrode. A linear relationship between $1/C^2$ and V exists in a metal/semiconductor junction:

$$\frac{1}{C^2} = \frac{2(\phi - V)}{qN\varepsilon_0\varepsilon_r A^2} \tag{3.3}$$

where C is the junction capacitance, V is the applied voltage, ϕ is the built in or contact potential, q is the charge of electron, N is the carrier concentration, ε_0 is the permittivity of free space, ε_r is the relative permittivity of the semiconductor and A is the effective contact or etch area on the sample. Therefore, the charge carrier concentration at the edge of the depletion region is given by:

$$N = \frac{1}{q\varepsilon_0\varepsilon_r A^2} \times \frac{C^3}{dC/dV} \tag{3.4}$$

By choosing sealing ring with a certain area, measuring C and dC/dV with a modulated voltage at different frequencies, the N can be derived. Together with step-wise etching, the carrier concentration profile can be obtained.

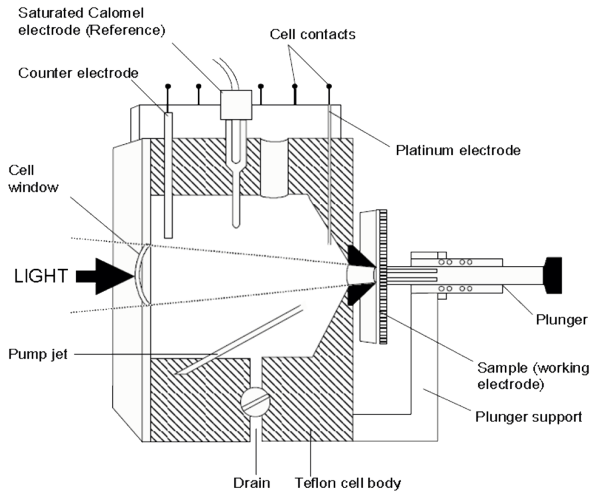

Figure 3.4: *electrochemical cell of an eCV setup*

3.3 Device characterization

Photo conductance lifetime. The effective minority carrier lifetime (τ_{eff}) is measured with a Sinton WTC-120 Photoconductance Lifetime tester. One mode for the test is the Quasi Steady-State mode (QSS), when slowly decaying flash pulse is used. In QSS mode, the excess carrier population is considered to be steady-state which means that the carrier generation rate ($G(t)$)and recombination rate are in balance. Simultaneously measurement of the sheet conductance inductively by RF coil coupled to the sample and the light intensity of the flash, the $G(t)$ and excess carrier density Δn can be derived by comparing to their respective reference. Then the lifetime effective carrier lifetime (τ_{eff}) can be determined via the steady-state condition $\Delta n = G\tau$. In this study, the τ_{eff} is always taken at $\Delta n = 10^{15} cm^{-3}$. The QSS mode is suitable for τ_{eff} under 200 μs. When τ_{eff} is above 200 μs, Transient Photoconductance Decay (PCD) mode is recommended. For transient mode, a shorter pulse of light is applied, usually in a range of 100-200 μs, and the decay of sheet conductance as a function of time is measured. Δn is derived from sheet conductance measured after each flash. Then the τ_{eff} is determined via $\tau = -\Delta n/(d\Delta n/dt)$. For QSS and PCD modes, they are both extreme cases where only steady-state and no generation are considered, respectively. The more common cases are the combination of both modes: the generalized analysis mode in which the τ_{eff} is given by [94]

$$\tau = \frac{\Delta n}{G - \frac{d}{dt}\Delta n} \tag{3.5}$$

Besides τ_{eff}, implied open circuit voltage (iV_{oc}) is another way to characterize the passivation quality defined by

$$iV_{OC} = \frac{k_B}{q} ln[\frac{(\Delta n + N_A)\Delta n}{n_i^2}] \tag{3.6}$$

where k_B is the Boltzmann constant, T is the temperature, q is the charge of electron, N_A is the acceptor doping concentration and n_i is the intrinsic carrier concentration. The iV_{oc} indicates the upper limit of V_{oc} in the cell. The upper limit of FF can also be obtained from implied fill factor (iFF) which is free of series resistance (R_{s}).

Current-Voltage (IV) characterization. The IV characterization is performed with a highly integrated solar cell analysis system "LOANA" from pv-tools GmbH.

Standard test conditions (AM1.5G, 100 mW/cm^2, 25 °C) is employed for the IV curve. Current density (J) is derived from dividing the total current with the cell area. The short circuit current density (J_{sc}) and open circuit voltage (V_{oc}) are determined from the IV curve at $V = 0\ V$ and $J = 0\ mA/cm^2$, respectively. FF is the ratio between maximum power (P_{mpp}) from IV curve and the product of V_{oc} and J_{sc}, i.e. $FF{=}V_{\mathrm{oc}} \cdot J_{\mathrm{sc}}/P_{mpp}$. The efficiency ($\eta$)of the cell is defined as ratio between P_{mpp} and the illumination power from the solar spectrum simulator ($P_{solar} = 100\ mW/cm^2$), i.e. $\eta{=}V_{mpp} \cdot J_{mpp}/P_{solar} = V_{\mathrm{oc}} \cdot J_{\mathrm{sc}} \cdot FF/P_{solar}$. The shunt resistance ($R_{\mathrm{sh}}$)and series resistance ($R_{\mathrm{s}}$) is measured from both IV curve and multi-light method.

Quantum efficiency (QE) offers detailed information of light absorption and carrier extraction in a solar cell with spectral resolution. The external quantum efficiency (EQE) is defined as the portion between the number of charge carriers collected by the solar cell and the number of photons illuminated on the cell as a function of wavelength. Compared tp EQE, the internal quantum efficiency (IQE), excludes the optical loss from front reflectance (R) by calculating $IQE = EQE/(1 - R - T)$. The IQE is the ratio between the number of charge carriers collected and the number of photons absorbed by the cell, giving an independent insight into the losses within the solar cell. The EQE and R are both characterized using LOANA and subsequently IQE is calculated.

4 Catalytic-doping on Silicon Alloys

In this chapter the structural, electrical, and optical properties of different silicon alloys, i.e. a-Si:H, μc-Si:H, nc-SiO_x:H and μc-SiC:H, will be discussed together with the impact of Cat-doping process when applied on these thin films. Cat-doping processes were applied on various doping types of these material as a guiding study for related device development. First the ghost film deposition during the Cat-doping process and the microstructure change of silicon alloys will be introduced and discussed. The impact of Cat-doping on the properties of aforementioned four materials will also be discussed separately in each section and then the correlation between the effectiveness of Cat-doping and the microstructures of different materials will be discussed.

4.1 Possible ghost film deposition and microstructure change

All the Cat-doping processes in this work didn't involve any use of SiH_4 containing gases, which means there was no intentional thin film deposition on the substrate by Cat-doping. The HWCVD chamber was also specifically used for Cat-doping without any other silicon thin film deposition performed in the chamber. However, there still could be some possibilities that thin films are deposited on the substrate, which is called ghost film deposition. The first is the re-deposition of silicon thin films. There is atomic H during the Cat-doping process due to the crack of PH_3 molecules. The atomic H could etch away existing silicon films on the substrate,

substrate holder or even the chamber wall and silicon thin films could be re-deposited on the substrate unwanted [12, 95, 96]. There could also be P_4 deposited due to the existence of P atoms [95] .

All these ghost re-deposited film could change the electrical and optical properties of the substrate, such as increasing the parasitic absorption. To evaluate the significance of ghost film deposition, a bare Corning glass was used during a Cat-doping process with PH_3 gas (2% diluted in Helium). The reflectance (R) and transmittance (T) were measured before and after Cat-doping process, the results are shown in Figure 4.1(a). The solid lines represent T, R and 1-T-R of the glass before Cat-doping and the dash lines represent results after Cat-doping. For all T, R and 1-T-R, the dash and solid lines overlap perfectly, indicating that there is no ghost film deposition or the ghost film deposition is negligible.

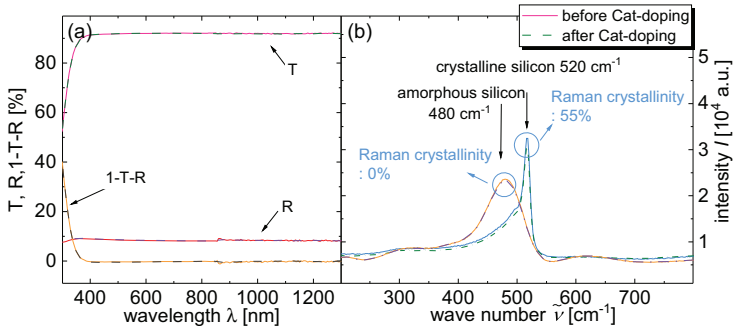

Figure 4.1: *Optical and structural properties before and after Cat-doping process: (a) the reflectance, transmittance and calculated absorptance by 1-T-R of a bare Corning glass before (solid lines) and after (dash lines) Cat-doping process (b) Raman spectrum of a-Si:H and μc-Si:H thin films before (solid lines) and after (dash lines) Cat-doping process*

Meanwhile, the etching of substrate films could also lead to the change in their microstructure. Raman spectrum of a-Si:H and μc-Si:H films both before and after Cat-doping is shown in Figure 4.1(b). The a-Si:H has a Raman crystallinity of 0% and μc-Si:H has Raman crystallinity of 55%. Same as the optical measurements, the solid lines and dash lines represent results before and after Cat-doping, respectively.

For both a-Si:H and μc-Si:H, the solid lines and dash lines overlap perfectly with each other and the evaluated Raman crystallinity remains unchanged, which implies that there no visible change in the microstructure of both amorphous and crystalline phases.

4.2 Mechanism of Cat-doping on silicon alloys

Cat-doping is based on HWCVD system which is a simple apparatus. But the mechanism of Cat-doping process itself is not yet totally understood due to its super facial doping depth. The fluxes of P radicals produced at the surface of hot filaments are simplified and illustrated in Figure 4.2. The movement of the P radicals could be divided into three directions: (1) absorbed at the surface of the silicon thin films, (b) desorb from the surface back into the vacuum, (c) diffuse into the film. Therefore, the dynamic of the radical flux could be expressed as below. Firstly, the P radical density inside the chamber at a given condition can be defined by [87]:

$$n = \frac{P_g}{kT_g} \tag{4.1}$$

where P_g is the gas pressure, k is the Boltzmann constant and T_g is the gas temperature. The thermal velocity of the radicals is:

$$\overline{\nu} = \sqrt{\frac{8kT_g}{\pi m}} \tag{4.2}$$

where m is the mass of the radicals. Then the number of P radicals collides with the substrate per unit area and unit time is:

$$J_0 = \frac{1}{4} n\overline{\nu} \tag{4.3}$$

When the P radicals are absorbed at the substrate surface, part of them will diffuse into the film and others will desorb back into the vacuum. The number of P radicals desorb form the substrate can be determined by [97]:

$$J_d = J_0 \nu_0 e^{-\frac{\Delta G_d}{kT}} \tag{4.4}$$

where ν_0 is the vibrational frequency and ΔG_d is the energy needed for desorption. With these three fluxes defined, the Cat-doping is then an equilibrium process at a given filament, chamber and substrate conditions, which also determine the effectiveness of Cat-doping in different silicon thin film materials.

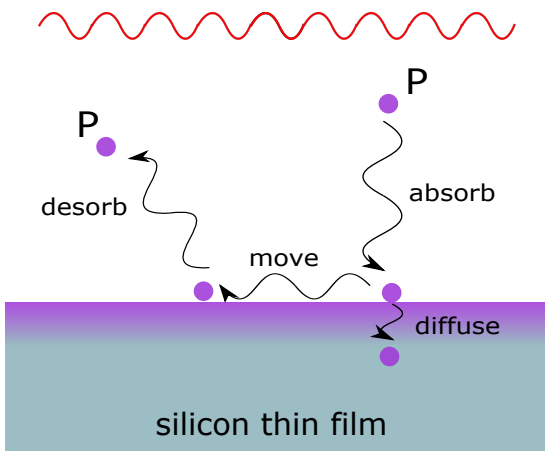

Figure 4.2: *Illustration of the Cat-doping process applied onto silicon thin films*

In a single Cat-doping process, the producing of P radicals could be seen as a dynamic equilibrium at given conditions. Consider the high energy needed for ion implantation, it is more reasonable to treat a Cat-doping process as a diffusion process. Then, the number of P radicals stay on the substrate can be seen as $J_0 - J_d$ due to continuously supply of PH_3 gas and small amount of P atoms diffused into the substrate. Therefore, the diffusion in a Cat-doping process could also be seen as an infinite source diffusion using Eq. 4.5. The diffusion of P atoms in silicon with infinite source might be describes using Fick's law as:

$$C(x,t) = C_S \; erfc \; (\frac{x}{\sqrt{2Dt}}) \tag{4.5}$$

where the P concentration $C(x,t)$ at a certain diffusion time t and depth x can be calculated from the source concentration C_S and diffusion coefficient D with the complementary error function $erfc$. In Eq. 4.5, the diffusion coefficient D can be determined using Arrhenius equation as:

$$D = D_0 \cdot e^{-\frac{E_A}{RT}} \tag{4.6}$$

where D is the diffusion coefficient, D_0 is the maximal diffusion coefficient(at infinite temperature), E_A is the activation energy for diffusion, R is the universal gas constant and T is the absolute temperature. Although diffusion is used to discuss the

in-diffuse flux in the Cat-doping shown in Figure 4.2, the actual mechanism is not very clear yet. Several speculations have been proposed by Matsumura et al. [87] together with some first-principle calculation [98], but no solid proof has been shown for those speculations. More discussion is shown in Sec.4.7.

4.3 Microcrystalline silicon

Microcrystalline silicon is considered as a promising candidate to be used in SHJ solar cells for its higher conductivity and slightly lower absorption coefficient compared to a-Si:H [9, 43]. With Cat-doping's ability of tuning the properties to the level beyond as-grown films, the electrical property of μc-Si:H could be pushed further for the use in SHJ solar cells. In this section, Cat-doping was applied onto different doping types of μc-Si:H with different Raman crystallinities (χ_c) and the influence on electrical property is discussed. The Cat-doping process parameter was initiated from Matsumura et al. [12] and the processing time was set to 10 min for sufficient doping.

4.3.1 Intrinsic microcrystalline silicon

Intrinsic microcrystalline silicon films with different χ_c was prepared by PECVD and the original conductivity (σ_0) was measured with evaporated Ag contacts. Then, Cat-doping was performed on these samples with T_f of 1000 °C and the conductivity (σ_{Cat}) was measured again on the same samples. The results are shown in Figure 4.3(a) together with calculated ratio between σ_{Cat}/σ_0 in Figure 4.3(b). First, the conductivity of these μc-Si:H(i) films increases exponentially with the increase of χ_c, from about 10^{-12} S/cm to 10^{-5} S/cm. This is likely due to the fact that at higher χ_c, the films have higher effective carrier mobility [99]. It could also be found that after Cat-doping, the conductivity increases considerably for all the samples with different χ_c. For the μc-Si:H with a crystallinity around 90%, the σ_{Cat} shows the highest value of 7.67×10^{-5} S/cm after Cat-doping. Comparing the conductivity increasing ratio vs the χ_c, it seems that they all scattered around 10^1 to 10^4 and shows no strong correlation between the increase of conductivity and their crys-

tallinities. The χ_c-independent increase in conductivity is benificial for Cat-doping application on μc-Si:H in SHJ solar cells. The choose of μc-Si:H with different χ_c can be determined by other parameters, such as conductivity, deposition condition and so on, while the increase through Cat-doping is always there.

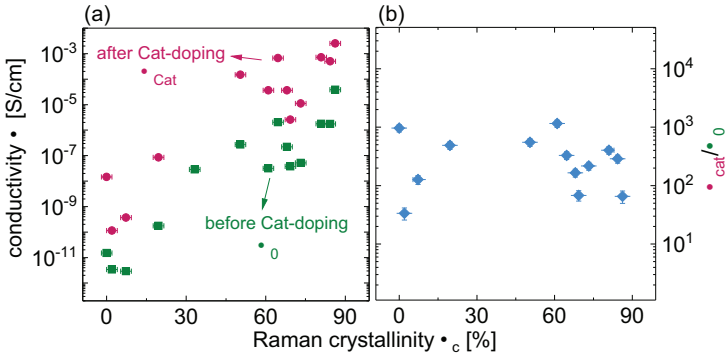

Figure 4.3: *(a) conductivity of intrinsic microcrystalline silicon before (σ_0,green) and after (σ_{Cat}, violet) Cat-doping process, (b) increasing ratio between conductivity after and before Cat-doping process: σ_{Cat}/σ_0*

During the Cat-doping process, different parameters, such as filament temperature (T_f), substrate temperature (T_{sub}) and processing pressure, may influence the effectiveness of Cat-doping. To evaluate the relationship between Cat-doping parameters and the doping profile, the Cat-doping parameters are systematically varied and the results are shown in Figure 4.4. Cat-doping is applied to the surface of μc-Si:H(i) and a layer of 15 nm a-Si:H(i) were deposited afterward as a capping layer, which acts as a barrier for the sputtering plasma and buffer layer before the plasma is stabilized.

First, T_f was varied from 1000 °C to 1800 °C, which affects directly the decomposition efficiency of PH_3. A reference sample of μc-Si:H(i) was also included for comparison. As shown in Figure 4.4(a), the reference sample has no P inside, so the curve of the reference sample actually represents the detection limit of the SIMS. When applying Cat-doping to μc-Si:H(i) films, P atoms are incorporated into the

film within a shallow depth. When increasing T_f, the P doping concentration (N_P) increases from $2 \times 10^{20} cm^{-3}$ at T_f of 1000 °C to $3 \times 10^{21} cm^{-3}$ at T_f of 1800 °C. Then in Figure 4.4(b), the T_{sub} was changed from 100 °C to 300 °C, but despite the incorporation of P atoms into μc-Si:H(i) films the P profiles don't differ much from each other. At different T_{sub}, they all have a similar N_P around $2 \times 10^{20} cm^{-3}$, as illustrated in Figure 4.4(c). The processing pressure was also altered from 0.01 mbar to 0.2 mbar and N_P first increases from $2 \times 10^{20} cm^{-3}$ at 0.01mbar to $1 \times 10^{21} cm^{-3}$ at 0.1 mbar, then drop slightly to $7 \times 10^{20} cm^{-3}$ at 0.2 mbar.

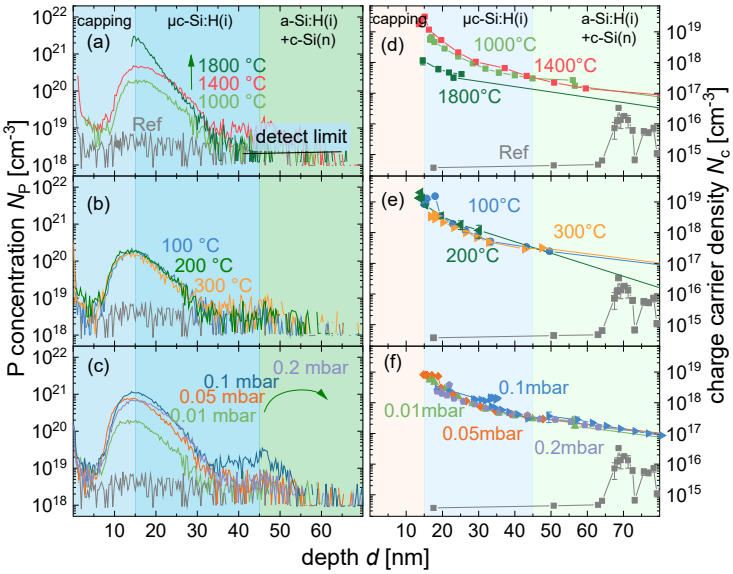

Figure 4.4: *P profiles and charge carrier density in µc-Si:H(i) after Cat-doping with different parameters: (a,d) Cat-doping at different T_f, (b,e) Cat-doping at different T_{sub}, (c,f) Cat-doping at different processing pressures*

Former study shows that at higher T_f, the decomposition efficiency of PH_3 is higher [95]. Therefore, the P radical concentration inside the chamber is larger at higher T_f and more P atoms might penetrate into the films resulting in larger N_P. The P radicals have higher translational kinetic energy when higher T_f was used [100]. Those P radicals with higher energy might penetrate deeper into the films. However,

due to the detection limit of SIMS, the tail of N_P cannot be seen and the accurate depth cannot be read. All the doping depth from Cat-doping are defined as the distance from the peak concentration to the point where N_P equals the detection limit. It should be noted that this definition of doping depth is acceptable since N_P below the detect limit may not have a major impact on the material properties nor device performance.

The diffusion coefficient of the P atoms inside silicon is defined by Eq. 4.6. When using larger T_{sub}, the D is larger, therefore more P atoms can diffuse into the films and the diffusion depth is also larger as defined by $d_{diff} = 2\sqrt{Dt}$, where t is the diffusion time. In the case of Cat-doping into silicon thin films, since the dynamic equilibrium of P radical producing process, it could be seen as a infinite diffusion source at the surface of the sample. As [100] has pointed out that the gas temperature inside the chamber will dramatically drop when it gets further from the filament. In addition, when the pressure inside the chamber is lower the impact on T_{sub} from T_f is less significant. Tests were carried out in this study simply by using a thermal tape indicator which can show roughly the temperature range of the substrate it adheres to. The results showed that at T_f=1000 °C, T_{sub}=200 °C, distance of 20 cm and pressure of 1 Pa, no obvious rise of T_{sub} occurs. It should be noted that, T_{sub} of 200 °C is mostly used in this study and this leads to additional thermal impact besides that from the hot filament. In many cases, the thermal impact from substrate heating would be larger than that from large-distance hot filament. Furthermore, when using higher pressure or T_f, the thermal impact from the hot filament could overrun the substrate heating. Nevertheless, these effects brings thermal annealing effect into the Cat-doping process.

Though the diffusion coefficient D is larger at higher T_{sub}, N_P at different T_{sub} is almost identical with a N_P of $2 \times 10^{20} cm^{-3}$ and depth of 15 nm, as shown in Figure 4.4. The P profiles in the μc-Si:H(i) at different T_{sub} are almost identical and shallow. Actually the temperature for diffusion of P atoms in silicon used in industry is very high, usually above 850 °C. Therefore, it might be related to the microstructure of μc-Si:H(i), such as grain boundaries, defects and dangling bonds inside the film. The relation between the effectiveness and microstructure of silicon

thin films will be discussed later in Sec. 4.7 together with other silicon materials.

Altering the processing pressure during the Cat-doping process leads to the increase of N_P at first then slight drop at even higher pressure. N_P first increases from $2 \times 10^{20} cm^{-3}$ at 0.01 mbar to $1 \times 10^{21} cm^{-3}$ at 0.1 mbar, then decreases slightly to $7 \times 10^{20} cm^{-3}$ at 0.2 mbar. The possible explanation could be that: first increasing the pressure could lead to the increase of PH_3 molecules inside the chamber therefore more P radicals will be produced, which in turn leads to the increase of N_P. However, at a given T_f, the decomposition efficiency is limited. With limited surface area of the filaments, the amount of PH_3 can be decomposed is limited. Further increase of PH_3 beyond the decompose limit inside the chamber will result in finite number of decomposed P radicals. When there are more PH_3 molecular than the filaments can decompose, the P radicals are diluted by the un-decomposed PH_3, which results in slightly decrease of N_P. It could also be that at higher pressure, the mean free path of those radicals decline so that less P radicals could reach the sample surface leading to the decrease in N_P.

The charge carrier densities (N_c) of μc-Si:H(i) films with Cat-doping at different conditions were also measured using electrochemical capacitance voltage (eCV). The results are illustrated in Figure 4.4(d,e,f). The reference is from μc-Si:H(i) film without Cat-doping. The N_c of $10^{15} \sim 10^{16} cm^{-3}$ may come from the intrinsic defects or impurities [101]. When different T_f were used, the N_P increases as T_f increases and it leads to slight increase in N_c from $7 \times 10^{18} cm^{-3}$ at T_f of 1000 °C to $3 \times 10^{19} cm^{-3}$ at T_f of 1400 °C. The N_c for T_f of 1800 °C is however lower around $1 \times 10^{18} cm^{-3}$ despite that the related N_P is the highest. The reason for this could be that at 1800 °C, the film starts to be etched by the H atoms inside the chamber and what measured is actually from deeper in the film where N_P is lower.

Changing the T_{sub} during the Cat-doping process didn't change N_P inside the μc-Si:H(i) films, which is also reflected in the N_c profiles in Figure 4.4(e). The N_c of all three different T_{sub} is around $2 \times 10^{19} cm^{-3}$ with no obvious difference. Altering the processing pressures also results in similar N_c at around $1 \times 10^{19} cm^{-3}$ for all different conditions, although the N_P in the pressure series shows trend of

first increase and then slightly drop. The reason for this similar N_c is not clear yet. It seems that despite at higher pressure and more P atoms were incorporated into the film, not all of them are activated and act as donors.

4.3.2 N-type doped microcrystalline silicon

The phosphorus doping on μc-Si:H(i) was realized by Cat-doping as described in Sec. 4.3.1, but due to the fact that Cat-doping is a shallow depth doping method [12], it still may not replace the use of more than $\sim$ 10 nm of doped μc-Si:H films which has an uniform and high doping. Therefore, the Cat-doping was performed on n-type in-situ doped μc-Si:H films to study the effect of Cat-doping on μc-Si:H(n). The electrical property was evaluated by conductivity measurement and the P distribution profiles were characterized by SIMS.

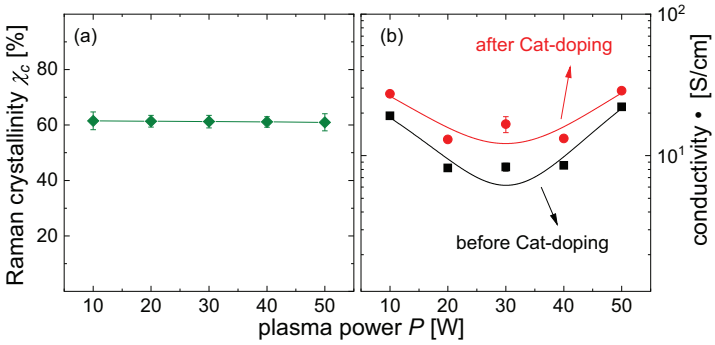

Figure 4.5: *(a) Raman crystallinity of μc-Si:H(n) deposited at different plasma powers and (b) the conductivity of μc-Si:H(n) before and after Cat-doping process*

The deposition condition could have a major effect on the property of μc-Si:H(n) films and the performance of device afterwards. Therefore, μc-Si:H(n) thin films were first prepared at different plasma powers and the Raman crystallinity was characterized. As shown in Figure 4.5(a), all the μc-Si:H(n) films deposited at different plasma powers all have similar χ_c around 60 %. The conductivity of different μc-Si:H(n) were measured on the same piece before and after Cat-doping and the results are shown in Figure 4.5(b). For μc-Si:H(n) films deposited at different plasma powers,

σ is similar around $10^1 S/cm$ and after Cat-doping, the σ all increased slightly by $1 \sim 2$ times. The reason for the increase in σ could be firstly the decrease of defects and increase of mobility and dopants activation ratio when the films are annealed by the thermal effect during the Cat-doping process [102, 103]. The second reason could be the increase in P donors due to P incorporation during Cat-doping process. Different effects co-exist during the Cat-doping process and details will be discussed in Sec. 5.1. Nevertheless, the increase in conductivity for all the samples means that the Cat-doping could be used to improve the electrical property of μc-Si:H(i) films regardless of the deposition condition and similar enhancement might be achieved. It is beneficial for device fabrication since the limitation is reduced on material choose while the effect of Cat-doping could be reserved. μc-Si:H(n) films prepared at different plasma powers have similar electrical improvement after Cat-doping, in the following work the 10 W condition is chosen for its low plasma power density thus low damage to the sample surface.

To have an insight of the P concentration and charge carrier density inside the μc-Si:H(n) films after Cat-doping, SIMS and eCV measurements had also been carried out, the results are shown in Figure 4.6. Firstly, from the SIMS results (4.6(a,b,c)), the μc-Si:H(n) films have a very high base doping of P, around $5 \times 10^{20} cm^{-3}$. After Cat-doping at different T_f, there is slightly increase of N_P in the first few nanometers. Changing T_sub doesn't affect N_P that much and the change can be ignored. Increasing the processing pressure, N_P has small increase in the surface layer. The reason for the small increase of N_P in μc-Si:H(n) films could be that these films are already highly doped. Thus, Cat-doping could incorporate a certain amount of P atoms, but compared to the increase ratio in μc-Si:H(i) the increase ratio in μc-Si:H(n) is much smaller. This is also reflected in the N_c, shown in Figure 4.6(d,e,f). When altering all the three parameters (T_f, T_sub, pressure), N_c doesn't vary much in the range of $10^{20} \sim 10^{21} cm^{-3}$. The total amount of the P atoms incorporated into the films and the active charge carrier, however, may differ from N_P and N_c results, where only trend is shown but no statics analyze. Together with comparison to other materials, the amount of P atoms and charge carriers will be discussed in Sec. 4.7.

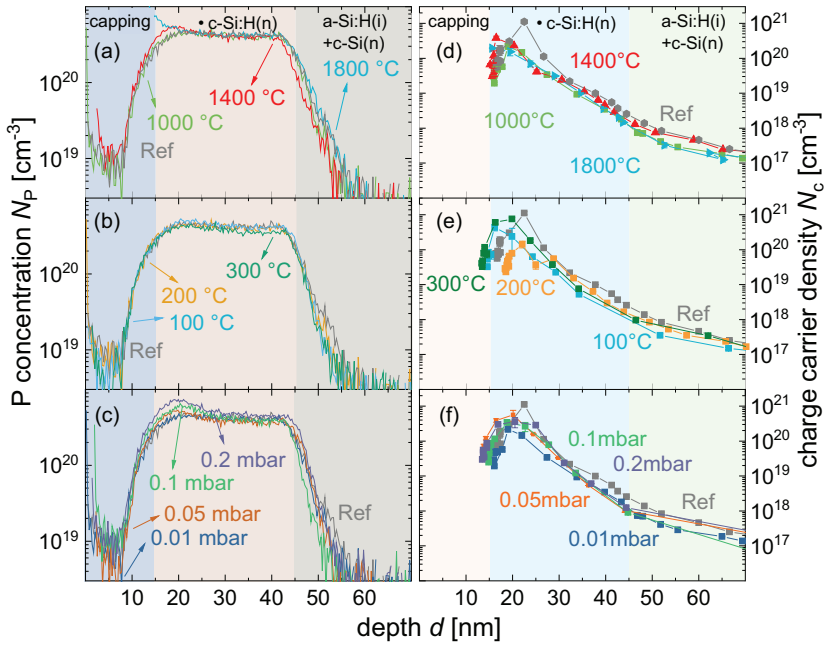

Figure 4.6: *P profiles and charge carrier density in μc-Si:H(n) after Cat-doping with different parameters: (a,d) Cat-doping at different T_f, (b,e) Cat-doping at different T_{sub}, (c,f) Cat-doping at different processing pressures*

4.3.3 P-type doped microcrystalline silicon

It has been shown that using Cat-doping the doping type of the silicon materials can be converted to the other one [12]. The conversion of doping types of the silicon materials then offers many potential applications in SHJ solar cells, such as contact patterning in an IBC solar cell or isolation formation between different contacts [104]. Therefore, Cat-doping is applied on μc-Si:H(p) for the investigation of compensate doping. First, 30 nm μc-Si:H(p) thin films were prepared on glass and then Cat-doping was done to the samples at different T_f. The conductivity σ was measured before and after Cat-doping process to monitor the change. A sample annealed at 220 °C is also included as reference for comparison and the change of conductivity before and after Cat-doping ($\Delta\sigma = \sigma_{Cat} - \sigma_0$) is plotted in Figure 4.7(a). There

are mainly three effects involved in a Cat-doping process, i.e. thermal annealing, hydrogenation and P doping, this will be discussed in detail in Sec. 5.1.

In the case of Cat-doping on μc-Si:H(p) films on glass using PH_3 gas, the thermal annealing which mainly comes from substrate heating and P doping may play a major role. For Cat-doping at T_{sub} of 200 °C, there is strong annealing effect. The annealing could lead to the increase in conductivity due to further activation of dopants, improvement of carrier mobility and reduce of defects inside the film [102, 103]. For the reference sample with only annealing, the conductivity increases by 1.1 S/cm which is likely solely due to thermal annealing. When Cat-doping was done to the samples, P atoms were incorporated into the films, which actually compensation the p-type doping in μc-Si:H(p) and reduces the conductivity. As shown in Figure 4.7(a) at T_{sub} of 200 °C, when introducing Cat-doping, σ still increase as less as 0.2 S/cm and it is not as much as that from the annealed sample. The possible explanation is that the annealing effect is now competing with the P doping to change the conductivity, but with T_{sub} of 200 °C, the annealing effect is the dominate one. Therefore, with Cat-doping, σ_{Cat} is still larger than σ_0, but the increase become smaller when increasing T_{f} which could incorporate more P atoms into the film. However, after 1300 °C, the increase in σ becomes larger again, this is likely due to the fact that when higher T_{f} was used, the thermal radiation from the hot filaments added up to the annealing effect and let the change in σ become large again.

To reduce the thermal annealing effect from the substrate, the heater temperature was lowered to 100 °C as well as room temperature (RT). At T_{sub} of 100 °C, the annealing effect is less significant. When Cat-doping is done to the films at T_{f} of 1000 °C, the change of σ is close to 0 indicating that the P doping completely compensated the annealing effect. Further increase T_{f}, $\Delta\sigma$ becomes negative down to -0.1 S/cm where the P doping dominates over the annealing effect. When further increasing T_{f} up to 2000 °C and above, $\Delta\sigma$ becomes positive again, indicating that the conductivity increase again and the annealing effect comes to play a big role again. For the series with T_{sub} at RT, the trend of $\Delta\sigma$ is similar but the turning point is different: the P doping overcomes the annealing effect after T_{f} reaches 1600

°C, the increase in $\Delta\sigma$ become smaller when increase T_f but even with the highest T_f of 2200 °C, $\Delta\sigma$ is still lower than 0.

Comparing $\Delta\sigma$ at T_{sub} of 100 °C and RT, the RT series seem to have less pronounced annealing effect, the turning point of $\Delta\sigma$ below 0 for the RT series should happen at lower T_f. However, the RT series has a turning point at T_f of 1600 °C, which is higher than that for the 100 °C series at T_f of 1000 °C. This contradiction indicates that there is another effect influencing the change in the conductivity. The most possible reason is the activation of P dopants from Cat-doping process happens at a certain temperature higher than RT. At RT P atoms were incorporated into the μc-Si:H(p) films but not activated due to low temperature. When increasing T_f, more P atoms are incorporated into the films and the annealing effect became more significant, so the amount of P atoms as well as the activation ratio of P atoms became larger.

In total, the P compensation doping became larger at higher T_f for the RT series and reduces σ. This could be the reason that the turning point for RT series happens at higher T_f. For the 100 °C series, the activation is larger at low T_f, so the P doping became dominate at lower T_f.

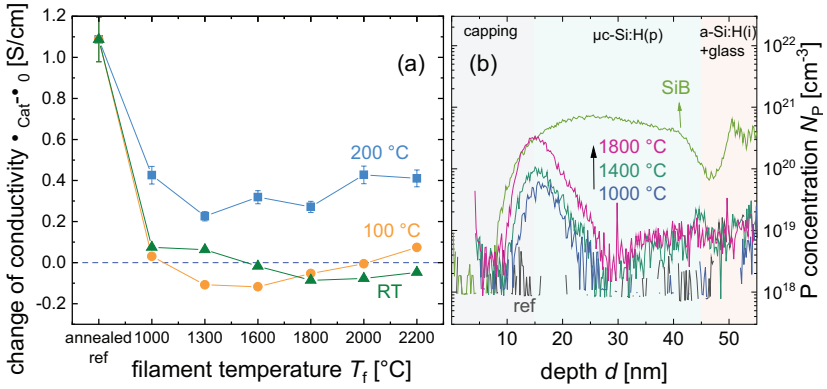

Figure 4.7: *(a): The conductivity change of µc-Si:H(p) before and after Cat-doping $\sigma_{Cat} - \sigma_0$ at different T_f and T_{sub}; (b): P profiles in µc-Si:H(p) after Cat-doping at different T_f together with the initial doped SiB profiles inside the films*

For a closer look at the distribution of P atoms inside the μc-Si:H(p) films, SIMS measurements were done to some of the samples, the results are shown in Figure 4.7(b). First, the μc-Si:H(p) film is initially doped by B with a Si-B pair concentration around $7.5 \times 10^{20} cm^{-3}$ and no P atoms inside, as shown in dark gray line which is actually the detection limit of SIMS. When applying Cat-doping onto the films at different T_{f}, different amount of P atoms were incorporated into the films. When using T_{f} of 1000 °C, the N_{P} is $6 \times 10^{19} cm^{-3}$. Further elevating T_{f}, N_{P} increases to $3 \times 10^{20} cm^{-3}$. Surprisingly, this value is exactly the same as the N_{P} from the Cat-doped μc-Si:H(i) films at T_{f} of 1800 °C in Sec. 4.3.1. It seems that the initial doping of B does not influence the further doping of P. This independence of N_{P} on initial B doping gives hints that the amount of P atoms incorporated into the films may not depend on the saturated N_{P} from as -deposited films, but on the Cat-doping conditions, such as T_{f}, T_{sub} and pressure. However, the significance of Cat-doping seems affected by the initial doping, i.e. when the initial doping is too high, the further doping from Cat-doping may not play a big role on the properties of the films.

4.4 Amorphous silicon

Hydrogenated amorphous silicon (a-Si:H) thin films are widely used in SHJ solar cells for both passivation and surface field/emitter when intrinsic and doped a-Si:H films are applied, respectively. The intrinsic a-Si:H layers offer excellent passivation quality for SHJ solar cells and can achieve very high V_{oc} in the solar cells [4, 5, 105]. However, there are still several problems with using a-Si:H in SHJ solar cells to be solved on its way to higher efficiency. One of the most important issues is that a-Si:H layers cause parasitic absorption in the short wavelength range [4]. The second one is that to guarantee sufficient passivation, a certain thickness of a-Si:H(i) is required. The poor conductivity of a-Si:H(i) layer then cause a poor trade-off between high passivation quality and good fill factor of SHJ solar cells. To improve the electrical property of a-Si:H films as passivation layer or surface field/emitter layer, Cat-doping on a-Si:H films are studied and discussed in this section.

4.4.1 Intrinsic amorphous silicon

Intrinsic amorphous silicon (a-Si:H(i)) films are used for passivation but have poor electrical property. Cat-doping was done on the a-Si:H(i) films to study the effectiveness of Cat-doping to improve the electrical property of a-Si:H(i). 35 nm a-Si:H(i) films were prepared and Cat-doping process was done on these films followed by SIMS characterization. The results are shown in Figure 4.8 with three variations in process conditions. Similar as for the Cat-doping on μc-Si:H(i/n) films in Sec.4.3, P atoms were incorporated into a-Si:H(i) films with different P concentrations N_{P}. First, when T_{f} increases from 1000 °C to 2200 °C, N_{P} increases from 2×10^{20} to 6×10^{21} cm^{-3}, together with the increase in penetration depth from 10 nm to 15$\sim$20 nm. When raising the T_{sub} from 100 °C to 300 °C, N_{P} decreases from 4×10^{20} to 1×10^{20} cm^{-3} while the penetration depth stays the same around 10 nm. As discussed in Sec.4.3.1, the decrease in N_{P} could be attributed to the fact that more P radicals escape from the substrate when higher T_{sub} is used. For the change in processing pressures, N_{P} first increases from 2×10^{20} to 3×10^{21} cm^{-3} due to the increase of P radicals at higher pressure, and the N_{P} decreases slightly to 2×10^{21} cm^{-3} due to the decrease of P radicals density at the sample surface. The doping depth also first increases from 10 nm to 15 nm then drop slightly.

4.4.2 N-type doped amorphous silicon

N-type doped amorphous silicon (a-Si:H(n)) films are usually used as front surface field layer in SHJ solar cells. P atoms are incorporated into the a-Si:H(i) films by Cat-doping and realized post-deposition doping within a shallow depth, it is also interesting to perform Cat-doping on a-Si:H(n) layers to investigate whether the electrical property can be improved further after deposition. Therefore, the same series of experiments done to the μc-Si:H and a-Si:H(i) were also performed on a-Si:H(n) layers. SIMS and eCV measurements were also carried out for the P profiles and charge carrier density profiles inside the films. The results are shown in Figure 4.9, where (a,b,c) are the P distribution profiles in the films after Cat-doping at different conditions and (e,d,f) are the charge carrier density inside. Reference sample was included for comparison. First, in Figure 4.9(a,d), the reference sample

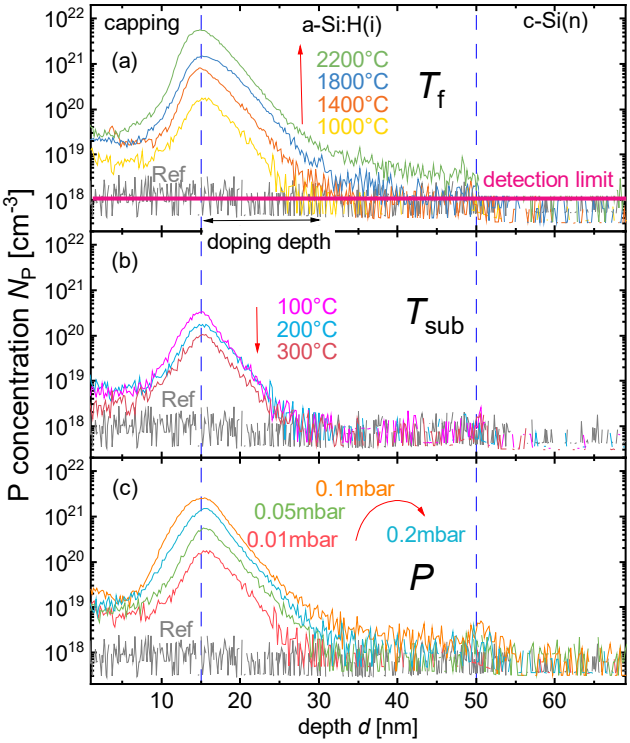

Figure 4.8: *P profiles in a-Si:H(i) after Cat-doping with different parameters: (a) Cat-doping at different T_f, (b) Cat-doping at different T_{sub}, (c) Cat-doping at different processing pressures*

of a-Si:H(n) without Cat-doping has a constant N_P of $1 \times 10^{21} cm^{-3}$ and a N_c of $2 \times 10^{18} cm^{-3}$ across the whole film. N_P increases slightly at the very facial thickness, when first lifting the T_f from 1000 °C to 1800 °C during the Cat-doping process. Continuing to raise the T_f N_P then increases relatively largely to $3 \times 10^{21} cm^{-3}$. Consequently N_c also increases when T_f increases, resulting a highest N_c of $1 \times 10^{19} cm^{-3}$ at a T_f of 2200 °C. Comparing to the P distributions in a-Si:H(i) after Cat-doping, the increase in N_P is less significant in a-Si:H(n) films, the reason could be that in P doped n-type a-Si:H, the N_P is already very high and the P atoms can neither been incorporated so easily nor the incorporated P atoms cannot make a huge difference at this level of N_P. As for N_c from eCV measurements, here the

N_c is plotted vs etched depth d_{etch} due to the fact that when the charge carrier density is very low, under a given condition of electrolyte used and voltage applied, the depletion width is very large. When the depletion is large to a extend of the thickness of the interested layer, the information of N_c inside the interested thin layer cannot be read clearly. By plotting N_c vs d_{etch} provides another way to see the change of N_c inside the film. This is possible because that the intrinsic capping layer is continuously etched away and the depletion zone will stretch into the Cat-doped layer where N_c increases, this increase could be seen in N_c profile.

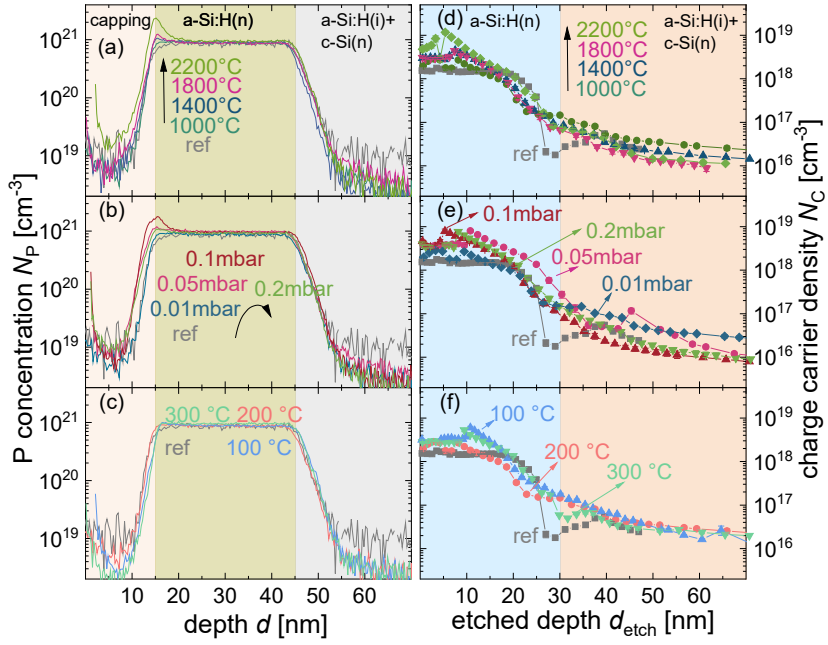

Figure 4.9: *P profiles and charge carrier density in a-Si:H(n) after Cat-doping with different parameters: (a,d) Cat-doping at different T_f, (b,e) Cat-doping at different T_{sub}, (c,f) Cat-doping at different processing pressures*

4.5 Nanocrystalline Silicon Oxide

Nanocrystalline silicon oxide is a wide band gap material that is a good candidate for front windows layer in SHJ solar cells. It consists of three phases: amorphous silicon oxide (a-SiO_x:H), a-Si:H and nanocrystalline silicon (nc-Si), as illustrated in Figure 4.10 [43, 69]. In Figure 4.10(a) is a-Si:H, inside which there is no crystalline phase but many voids and defects. In Figure 4.10(b), the μc-Si:H has both a-Si:H phase and crystalline (c-Si) phase. In Figure 4.10(c-d), nc-SiO_x:H has additional a-SiO_x:H phase with a larger optical band gap. The larger band gap of a-SiO_x:H than the commonly used a-Si:H film benefits in light absorption in the front side of a cell. The property of nc-SiO_x:H is tunable through deposition conditions, such as O concentration in the gas mixture. However, the limitation of nc-SiO_x:H lies on the trade-off between the electrical and optical properties of the nc-SiO_x:H films. With higher O concentration C_O inside the film, it is more transparent but less conductive; with lower C_O, the film is less transparent but more conductive. Changing the CO_2 ratio in the gas mixture is the most direct way to alter the C_O inside nc-SiO_x:H films. Shown in Figure 4.10(e) is the conductivity σ and optical band gap E_{04} of nc-SiO_x:H(n) with different O concentrations, which is represented by the CO_2 ratio in the gas mixture. The CO_2 ratio in the gas mixture is defined as:

$$r_{CO_2} = \frac{[CO_2]}{[CO_2] + [SiH_4]} \times 100\% \tag{4.7}$$

The a-Si:H film has the relatively high σ but its E_{04} is also very low, which results in large parasitic absorption when the a-Si:H film is used in the front of the cell. Microcrystalline silicon has slightly larger σ and E_{04}, but the optical loss in the film is still high compared to nc-SiO_x:H. The nc-SiO_x:H films with different C_O have very large E_{04} and this large E_{04} makes it suitable to be used in the front of a cell. However, σ of nc-SiO_x:H films is not as high as a-Si:H and μc-Si:H, the more O content it has, the less conductive it is. Thus, the contradictory in optical and electrical properties poses a trade-off when choosing which C_O to use. Fortunately, Cat-doping might be used to further dope the as-grown nc-SiO_x:H films to make them more conductive.

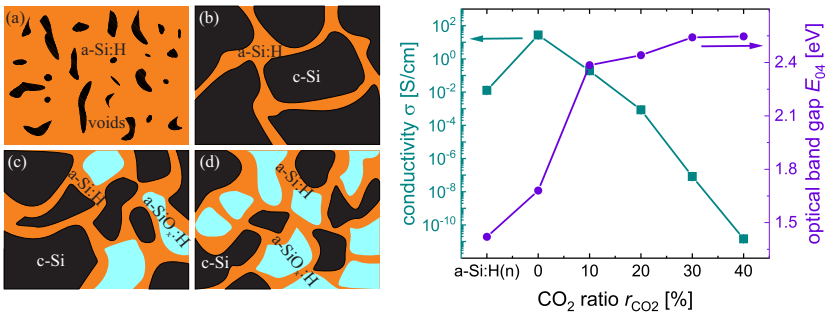

Figure 4.10: *Illustration of microstructure in (a): a-Si:H,(b): μc-Si:H, (c-d): nc-SiO_x:H with different C_O [106]; (e): conductivity σ and optical bandgap E_{04} of a-Si:H, μc-Si:H and nc-SiO_x:H with different C_O*

Cat-doping processes were done at T_f of 1000 °C, T_{sub} of 200 °C, pressure of 0.01 mbar on P-doped n-type a-Si:H, μc-Si:H and nc-SiO_x:H films to investigate the effectiveness of Cat-doping. Here, nc-SiO_x:H with different C_O were used. SIMS, conductivity and eCV measurements have been carried out to monitor the P distribution and electrical property change. First, P profiles are shown in Figure 4.11. For a-Si:H(n) in Figure 4.11(a), as discussed in Sec.4.4.2, the initial N_P is already very high and at T_f of 1000 °C, there isn't large amount of P atoms incorporated into the film. For μc-Si:H(n) in Figure 4.11(b), the initial doping used here is not very high, therefore the P atoms incorporated into the film shows significant increase from 3×10^{20} to $6 \times 10^{20} cm^{-3}$.

For nc-SiO_x:H(n), here r_{CO_2} was varied from 10% to 40% for films with different optical and electrical properties. The initial N_P in nc-SiO_x:H(n) films is around $5 \times 10^{20} cm^{-3}$, after Cat-doping N_P increases slightly and with higher r_{CO_2}, the increase becomes smaller. The increase in N_P also seems to cross though the whole film, which differs from that in μc-Si:H(n). The reason for the unique behavior of P distribution could be related to the microstructure of nc-SiO_x:H films. Inside the nc-SiO_x:H films shown in Figure 4.10(c-d), there are three phases, i.e. a-Si:H, c-Si and a-SiO_x:H. In the microstructure of nc-SiO_x:H(n) film, the microscopically more porous Si-O structure of a-SiO_x:H phase may allow the P atoms to penetrate deeper than in μc-Si:H(n) film [73]. However, the additional P atoms inside the a-SiO_x:H

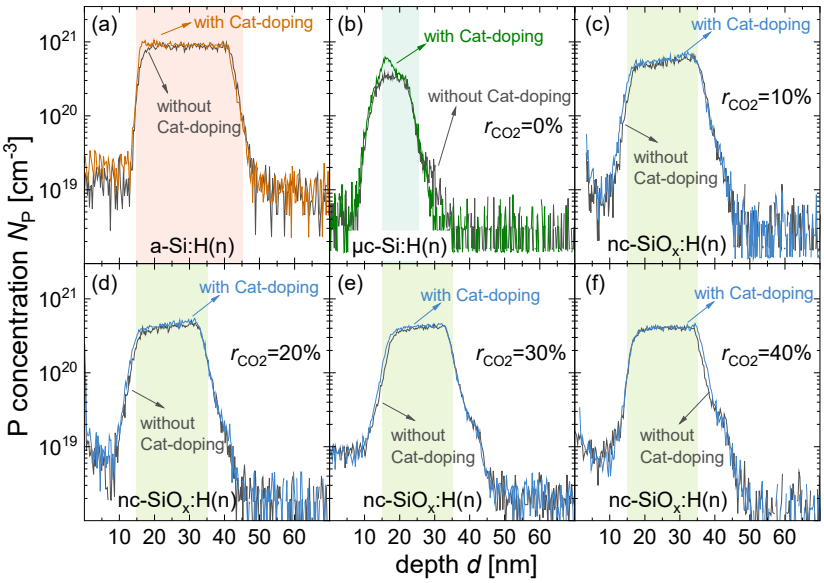

Figure 4.11: *P profiles from SIMS measurement in (a): a-Si:H(n), (b): μc-Si:H(n), (c-f): nc-SiO$_x$:H(n) with different C_O from different r_{CO_2}. A reference sample without Cat-doping is included for each film and the color stripes indicate the thickness of the layer. All the samples were prepared on 5 nm a-Si:H(i)/c-Si substrate and 15 nm a-Si:H(i) films were subsequently deposited after Cat-doping process as capping layer*

phase doesn't seem to provide more charge carriers. To check the activation of P atoms as charge carriers, eCV measurements were done on these sample and the results are shown in Figure 4.12.

For N_c of a-Si:H(n) in Figure 4.12(a), there is no difference between the samples with and without Cat-doping which agrees with the P profile from Figure 4.11(a), where N_P doesn't increase. As for N_c of μc-Si:H(n) in Figure 4.12(b), there is clearly increase amount of charge carriers. For nc-SiO$_x$:H(n), first the initial N_c decreases as the C_O increases, this is likely due to the increase of a-SiO$_x$:H phase inside the film and the P atoms inside the a-SiO$_x$:H phase don't contribute to N_c. Then, after Cat-doping N_c all increase for all nc-SiO$_x$:H films but to different extends: the higher C_O the film has, the less increase in N_c. The increase in N_c then changes the

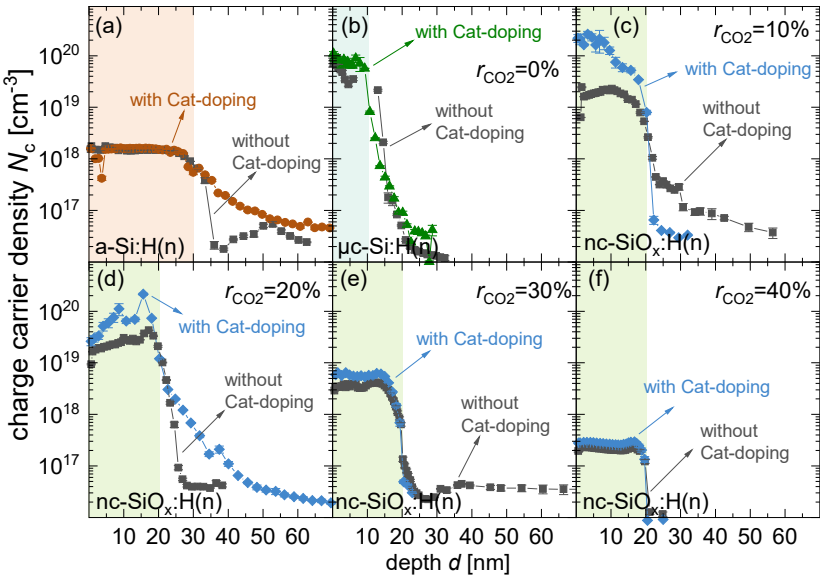

Figure 4.12: *Charge carrier density N_c in (a): a-Si:H(n), (b): μc-Si:H(n), (c-f): nc-SiO_x:H(n) with different C_O from different r_{CO_2}. A reference sample without Cat-doping is included for each film and the color stripes indicate the thickness of the layer.*

electrical properties of nc-SiO_x:H films, as shown in Figure 4.13. First, when the r_{CO_2} increases from 0% to 40%, the σ decreases from $19 S/cm$ to $1.46 \times 10^{-11} S/cm$. The possible reason for the decrease of σ is that when increasing the r_{CO_2}, the crystallinity decreases and the portion of crystalline phase inside the film becomes smaller, which reduces the mobility of carriers as well as the doping efficiency [48, 107]. The number of charge carriers is also reduced by increasing the r_{CO_2} from Figure 4.12.

However, from the P profiles in Figure 4.11, it is difficult to determine how many P atoms are doped inside the films. Therefore, the average value was calculated for P concentration ($N_{\mathrm{P,\ ave}}$) and charge carrier density ($N_{\mathrm{c,\ ave}}$) throughout the doping depth, then the activation ratio of P atoms in nc-SiO_x:H(n) films is calculated from $N_{\mathrm{c,\ ave}}/N_{\mathrm{P,\ ave}}$ and compared between with and without Cat-doping.

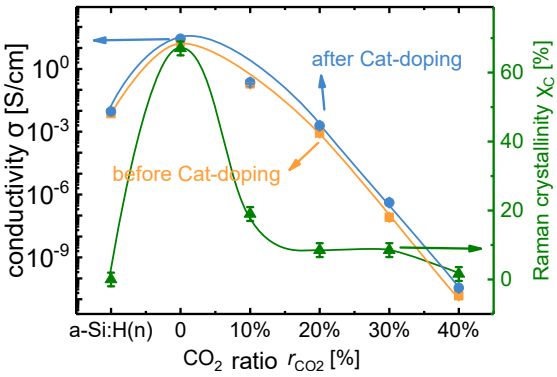

Figure 4.13: *Conductivity σ of nc-SiO_x:H(n) films with different r_{CO_2} measured before and after Cat-doping. a-Si:H(n) and μc-Si:H(n) are include as comparison, the Raman crystallinity χ_c is also included indicating that the crystalline phase reduces as increase of r_{CO_2}*

In Figure 4.14(a) is the $N_{\mathrm{P,\ ave}}$ in different films. They are all located in the range of 10^{20} to $10^{21} cm^{-3}$ and after Cat-doping. The $N_{\mathrm{P,\ ave}}$ all increase but with different significance. The μc-Si:H(n) film has the largest increase in $N_{\mathrm{P,\ ave}}$ ($\Delta N_{\mathrm{P,\ ave}}$) of $10^{20} cm^{-3}$, the a-Si:H(n) has slightly lower $\Delta N_{\mathrm{P,\ ave}}$ of $4{\times}10^{19} cm^{-3}$. For nc-SiO_x:H(n), there is also increase in $N_{\mathrm{P,\ ave}}$ and with r_{CO_2} increasing from 10% to 40%, the $\Delta N_{\mathrm{P,\ ave}}$ decreases from $5 \times 10^{19} cm^{-3}$ to $2 \times 10^{19} cm^{-3}$. The $N_{\mathrm{c,\ ave}}$ is shown in Figure 4.14(b), and $\Delta N_{\mathrm{c,\ ave}}$ is also calculated. First, for a-Si:H(n) the $N_{\mathrm{c,\ ave}}$ stays unchanged indicating that there is no more P atoms activated as dopants. For μc-Si:H(n), the $N_{\mathrm{c,\ ave}}$ increased by $3 \times 10^{19} cm^{-3}$. When adding O inside the films, $\Delta N_{\mathrm{c,\ ave}}$ drops 4 orders of magnitude from $1{\times}10^{20} cm^{-3}$ at r_{CO_2}=10% to $5{\times}10^{16} cm^{-3}$ at r_{CO_2}=40%. The change in $N_{\mathrm{c,\ ave}}$ then likely accounts for the change in σ shown in Figure 4.13. Now, the $N_{\mathrm{P,\ ave}}$ and $N_{\mathrm{c,\ ave}}$ of different films are obtained, the average activation ratio of P atoms ($r_{\mathrm{a,\ ave}}$) into dopants providing free charge carriers can be calculated. The results are shown in Figure 4.14(c) and the difference($\Delta r_{\mathrm{a,\ ave}}$) in Figure 4.14(d). The $r_{\mathrm{a,\ ave}}$ for μc-Si:H and nc-SiO_x:H with Cat-doping all increase compared to the ones without Cat-doping and with rise of r_{CO_2} from 0% to 40%, the increase in $r_{\mathrm{a,\ ave}}$ ($\Delta r_{\mathrm{a,\ ave}}$) becomes several orders smaller, changing from 10% to 10^{-2}%.

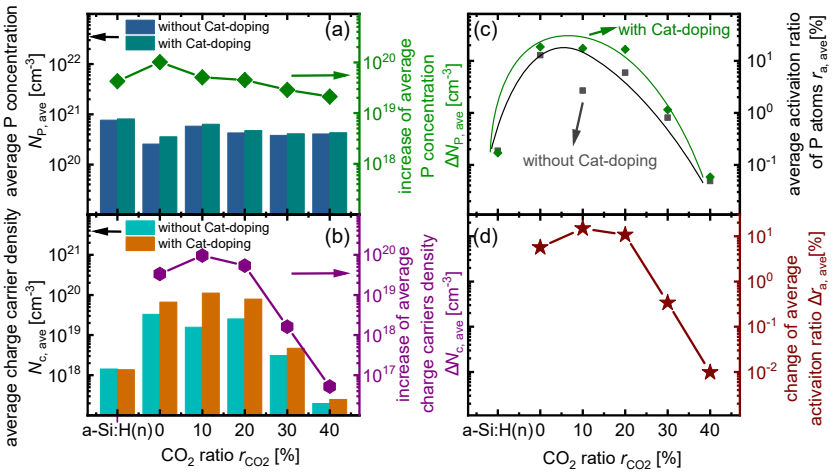

Figure 4.14: *The average value of P concentration and charge carrier density inside a-Si:H(n), μc-Si:H(n) and nc-SiO$_x$:H(n) films with and without Cat-doping process: (a): the average P concentration ($N_{P,\,ave}$) and increase of $N_{P,\,ave}$ ($\Delta N_{P,\,ave}$) inside different films derived from SIMS; (b): the average charge carrier density ($N_{c,\,ave}$) and increase of $N_{c,\,ave}$ ($\Delta N_{c,\,ave}$) inside different films derived from eCV data; (c): the activation ratio of P atoms inside the films derived from $N_{c,\,ave}/N_{P,\,ave}$ and (d): the change of activation ratio with and without Cat-doping*

To explain the difference in effectiveness of Cat-doping and the activation of P atoms inside films with different C_O, the microstructures of these films might be considered. Already shown in Figure 4.10(a-d), if consider that nc-SiO$_x$:H has three phases inside, i.e. a-Si:H, c-Si and a-SiO$_x$:H, with the rise of C_O, the portion of a-SiO$_x$:H phase becomes larger while the portion of c-Si shrinks. When Cat-doping is applied onto nc-SiO$_x$:H(n) films, the $\Delta N_{P,\,ave}$ also decrease with the rise of r_{CO_2} and portion of a-SiO$_x$:H, this indicates that the P atoms from Cat-doping process prefer to in-diffuse through the c-Si phase than the a-SiO$_x$:H phase. As mentioned before, the $r_{a,\,ave}$ is higher for films with Cat-doping, which implies that the P atoms incorporated by Cat-doping have higher activation ratio. With drop of c-Si portion, the $\Delta r_{a,\,ave}$ also gets smaller, this again implies that the P atoms inside the c-Si phase are more activated as dopants than that in a-SiO$_x$:H phase.

Atom probe tomography (APT) was used to investigate the location of the P atoms incorporated by Cat-doping. Two samples with and without Cat-doping were measured and the P information in terms of location and concentration is given in Figure 4.15. In Figure 4.15(a) is the elemental map of the $25 \times 25 \times 10nm$ sample with Cat-doping where the different phases are shown and the c-Si phase is clearly separated from the a-SiO_x:H phase. There is smaller amount of O inside the c-Si part since this is the summary of 10 nm thick films, where the c-Si and a-SiO_x:H overlap each other. In Figure 4.15(b) is the P atom map inside the film and the Si-rich area is also shown. Comparing the c-Si phase and the a-SiO_x:H phase, there are slightly more P atoms gathering in the c-Si phase (shown in Figure 4.15 (c)).

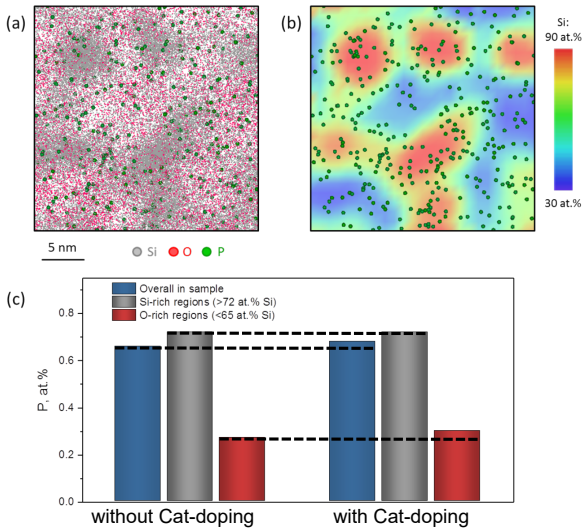

Figure 4.15: *APT analysis of the nc-SiO_x:H(n) films: (a): elemental map of a* $25 \times 25 \times 10nm$ *subvolume of the sample with Cat-doping visualizing the formation of Si-rich fibers in the film (growth direction is perpendicular to the image plane). (b): P map overlaid on the two-dimensional Si concentration plot for the same subvolume. (c): P concentration in the entire film and separately in the Si-rich and O-rich regions of the film.*

4.6 Microcrystalline Silicon Carbide

Microcrystalline silicon carbide (μc-SiC:H) with wide band gap and high electrical conductivity is very suitable to be used as window layer in SHJ solar cells. The μc-SiC:H used in this work was first developed by Pomaska et al. [108] and is called unintentional n-type doped μc-SiC:H since the dopants come from the residual nitrogen (N) in the chamber. HWCVD was used to prepare the μc-SiC:H(n) films and the films' conductivity increases with the increasing T_f [109], but the passivation quality with μc-SiC:H films will deteriorate if T_f is above 1800 °C [14]. To overcome the trade-off between the conductivity and passivation quality, effect of Cat-doping on μc-SiC:H(n) films is investigated. Here, both μc-Si:H and nc-SiO_x:H films are taken for comparison. Firstly, illustration of possible microstructure of three silicon alloys are shown in Figure 4.16 [69]. Compared to the other two materials, the μc-SiC:H has a much denser microstructure and only between the grains boundaries exists some a-SiC:H(n). This difference might has influence on the effectiveness of Cat-doping on μc-SiC:H(n) films.

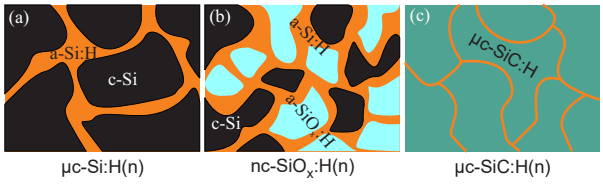

Figure 4.16: *Illustration of possible microstructures of three silicon alloys [73]: (a): μc-Si:H(n), both a-Si:H phase and c-Si phase exist inside the film; (b): nc-SiO_x:H(n), three phases exist inside the film, i.e. a-Si:H, a-SiO_x:H and c-Si; (c): μc-SiC:H where there is mostly crystalline silicon carbide grains and small portion of amorphous silicon carbide at the grain boundaries*

P profiles by SIMS were shown in Figure 4.17 and they reveal the difference of P distribution inside the films. A reference sample without Cat-doping for each silicon alloy is also included. For μc-Si:H(n) with Cat-doping, as shown in Figure 4.17(a), there is an increase in N_P from $3 \times 10^{20} cm^{-3}$ to $6 \times 10^{20} cm^{-3}$ at the interface of a-Si:H(i) capping layer and the μc-Si:H(n) layer. The penetration

depth of P atoms from Cat-doping is 5 nm from the interface into the μc-Si:H(n) layer. For nc-SiO_x:H(n) in Figure 4.17(b), there is also an increase in N_P from $2 \times 10^{20} cm^{-3}$ to $3.5 \times 10^{20} cm^{-3}$ throughout the 20 nm nc-SiO_x:H(n) film. For μc-SiC:H(n) in Figure 4.17(c), there is barely any increase of N_P in the film and the P atoms seem to attach only to the surface of μc-SiC:H(n) film with a concentration of $6 \times 10^{19} cm^{-3}$. It should be noted that the μc-SiC:H(n) thin film is initially nitrogen doped, so no P atoms exist in the reference sample. The black curve in Figure 4.17(c) indicates the detect limit of SIMS.

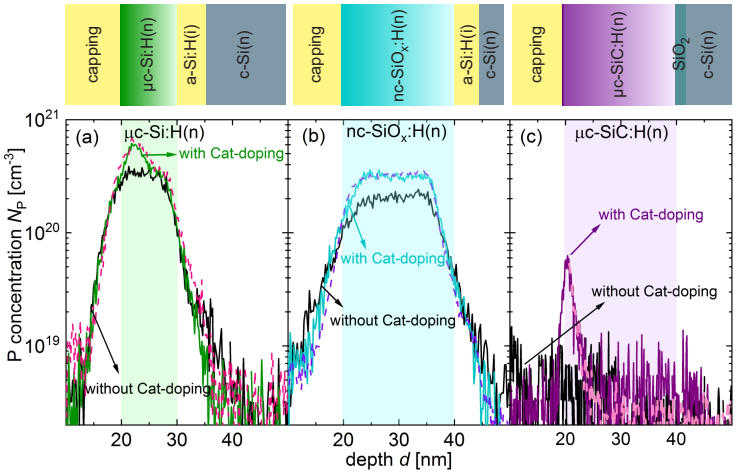

Figure 4.17: *P profiles of three silicon alloys together with sketches of the samples structures: (a) µc-Si:H(n), (b) nc-SiO_x:H(n) and (c) µc-SiC:H(n); the thicknesses are 10nm, 20 nm and 20 nm for each silicon alloy films ,respectively. Here the nc-SiO_x:H(n) used was deposited with different parameters compared to the ones in Sec.4.5, so there is a large difference in the initial N_P. The dash lines in each profiles is a repeat measurement of the sample to confirm the existence of change in N_P. The color stripes represent the silicon alloy layers in the P profiles. The µc-Si:H(n) and nc-SiO_x:H has 5 nm a-Si:H(i) layer beneath but for µc-SiC:H is a 1.5 nm SiO_2 layer*

The average N_P ($N_{P,\,ave}$)inside silicon alloy films by Cat-doping was derived from P profiles, as shown in Figure 4.18(a). For μc-SiC:H, the film is initially N doped, so there is zero P atoms inside the film. $N_{P,\,ave}$ in the silicon alloy films all increased

after Cat-doping, but with different numbers. The increase of $N_{\mathrm{P,\,ave}}$ for μc-Si:H(n) and nc-SiO_x:H(n) after Cat-doping is $1 \times 10^{20} cm^{-3}$ and $2.7 \times 10^{20} cm{-}3$, respectively and these two materials have a similar increase of P atoms in the order of $10^{20} cm^{-3}$. For μc-SiC:H(n), the increase is 2 orders of magnitude less, only $1.6 \times 10^{18} cm^{-3}$. As mentioned before, the effect of Cat-doping likely relates to the microstructure of the materials. Therefore, for the very dense μc-SiC:H(n) film, only small portion of a-SiC:H exists inside the film and this may make it hard for the P atoms to penetrate into the film. From SIMS results in Figure 4.17(c), it can also be seen that the P atoms are mostly attached only at the surface with low N_{P}.

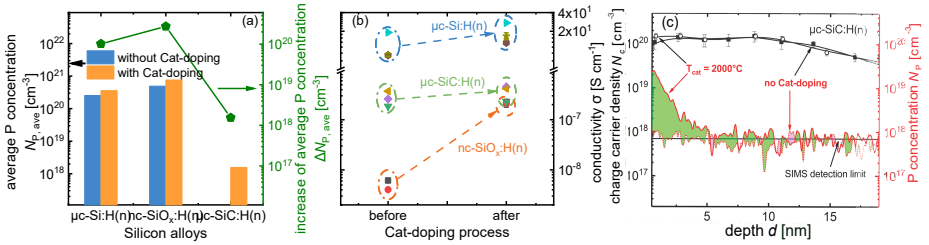

Figure 4.18: *(a): the average P concentration inside three silicon alloy films and the increase of $N_{P,\,ave}$ derived from P profiles and (b): the conductivity change for three silicon alloys films before and after Cat-doping process.The conductivity was measured on the same samples before and after Cat-doping and multiple pieces have been measured to confirm the increase in conductivity. Cat-doping at higher T_f on μc-SiC:H(n) was also carried out by Felix Komoll, the P profiles and charger carrier density profiles were also obtained in (c).*

As P atoms are known dopants for all three types of silicon alloys [10, 110–112], the electrical conductivity is likely to be increased due to the increase of N_{P}. Thus, the electrical conductivity of these films was measured before and after the Cat-doping process and the results are shown in Figure 4.18(b). The results show that the average conductivity for all sample pieces with different silicon alloy films increased after Cat-doping due to incorporation of P atoms, but to a different extend. The μc-Si:H(n) film samples have the largest increase in average conductivity in absolute numbers of $10^{1} Scm^{-1}$. For the nc-SiO_x:H(n) samples, the σ increased almost by two orders of magnitude, from 10^{-9} to $10^{-7} Scm^{-1}$. And for μc-SiC:H(n), the σ only increases slightly by $1 \times 10^{-7} Scm^{-1}$. The reason for the increase in σ could be the

decrease of defects and the increase of mobility and dopants activation ratio of silicon alloys when the samples are annealed by the substrate heating and hot filaments during the Cat-doping treatment [102, 103]. Another reason may be attributed to the increase in phosphorous donors. However, for μc-Si:H(n) and nc-SiO_x:H(n), the amounts of P atoms incorporated into the films are within the same order of $10^{21} cm^{-2}$, the absolute increase in σ is much lower for nc-SiO_x:H(n) indicating a much lower doping efficiency of incorporated P atoms. Here, the activation ratio difference between μc-Si:H(n) and nc-SiO_x:H(n) films has already been discussed in Sec.4.5. The crystalline volume fraction of μc-Si:H(n) and nc-SiO_x:H(n) was derived from Raman spectrum to be $\sim$ 60% and $\sim$ 9%, respectively. The lower doping efficiency could partially be attributed to a lower crystalline volume fraction as lower doping efficiency has been reported for materials with lower crystalline volume fraction [48,107]. However, the determination of the ratio between active and inactive Cat-doped P atoms for μc-Si:H(n) and nc-SiO_x:H(n) is clear from Sec.4.5 that the P atoms from Cat-doping are more activated. But for μc-SiC:H(n) it is still unclear and under investigation. Nevertheless, for μc-SiC:H(n), the effect of the P atoms at the film surface still remains unclear, as the doping is very small and superficial, also because the average increase in σ of $1 \times 10^{-7} Scm^{-1}$ is within the error range of the measurement. Higher T_f during the Cat-doping process on μc-SiC:H(n) film was also used by Felix Komoll. However, the penetration of P atoms is also very shallow, as shown in Figure 4.18(c). The N_c also doesn't vary much. To increase the conductivity significantly in future the Cat-doping process needs to be adjusted in order to implement more P atoms intoμc-SiC:H(n) films as well as increasing the diffusion depth.

4.7 Comparing Cat-doping on different silicon alloys

The mechanism of Cat-doping to incorporate dopants into silicon thin films is not clear yet. Matsumura et. al. [87] proposed several speculations upon how dopants penetrate into c-Si: firstly, from first-principle calculation the P atoms could diffuse into c-Si much easier with the help of H, which is a condition that Cat-doping

provides; secondly, the P atoms might diffuse in form of vacancy-P atom pair in which the vacancy is created by atomic H; thirdly, the c-Si surface layer might be modified by the stress from H attack, thus the facial 5 nm has a different structure as normal c-Si and leads to the shallow doping by Cat-doping. However, despite many experimental results seem to support these speculations, no direct and solid experiments have been reported to support these models. In this work, we extends the materials from c-Si and a-Si:H to other silicon alloys (i.e. μc-Si:H, nc-SiO_x:H and μc-SiC:H). Doping profiles show that the Cat-doping process is more complicate than aforementioned models and possibly related to the microstructures of different silicon alloy thin films. Furthermore, the properties of different films is also changed accordingly to the film compositions upon Cat-doping.

As for a-Si:H films, if compared to c-Si wafers, it has much looser microstructure due to existence of voids and defects. One of speculations above is that P atoms penetrate through defects(such as vacancy and dangling bonds). In a-Si:H films, there are much larger number of these defects throughout the film that can help P atoms to penetrate into the films. The larger N_{P} and deeper penetration depth of P (see in Sec. 4.4) are in agreement of this assumption. Meanwhile, if assume that P atom penetrates into the film via hopping from one dangling bond to a deeper one with the help of H to break the bonds [12], the surface has more chance in contact with H atoms making the P profile gradually decreases as the doping depth increases. Furthermore, both P and H atoms could be captured by the dangling bonds inside the film making the number of P and H atoms from Cat-doping decreases in deeper position inside the film, this explains the limited penetrate depth of P profiles. At last, the number of dangling bonds inside the film is limited, therefore the peak of P profiles at the sample surface is likely limited to a certain extend, which is dependent on the film property. When most dangling bonds are bonded to P or H atoms, the saturation of P from Cat-doping occurs. Upon the saturation of N_{P}, even with largely increasing of treatment time the P profile will not increase any further. This is also in agreement with reported result from Ref. [12].

The behavior of Cat-doping becomes more interesting when it comes to nc-SiO_x:H and μc-SiC:H since their microstructures and compositions are very different from

both c-Si and a-Si:H. The P atoms are incorporated into nc-SiO_x:H films throughout the whole thickness, while P atoms only attaches to the surface of μc-SiC:H films with much lower N_P. There are several possible reasons. Firstly, the solubility of H_2 is much higher in nc-SiO_x:H than that in μc-SiC:H films. While H might help the incorporation of P, higher solubility of H_2 could contribute to the higher incorporation of P. Meanwhile, nc-SiO_x:H has a porous cage structure that is more flexible than that of μc-SiC:H, which has a much denser microstructure consisting of mostly crystalline silicon carbide grains surrounded by amorphous grain boundaries. Furthermore, the bonding energy of Si-C (E_{bond}=3.3 eV) is also higher compared to Si-Si (E_{bond}=2.3 eV), the need to break existing bonds in μc-SiC:H might make it much more difficult to incorporate P into μc-SiC:H than that in a-Si:H and c-Si. Different from breaking existing bonds in μc-SiC:H, c-Si and a-Si:H, P atoms may penetrate into nc-SiO_x:H through interstitial diffusion via the porous cage structure in nc-SiO_x:H films [113,114]. This porous cage structure might offer a channel for P atoms to penetrate throughout the whole film without obvious decrease in N_P. All in all, the difference in microstructure and composition is likely to enable Cat-doping incorporate more P atom and penetrate deeper in nc-SiO_x:H films than in μc-SiC:H films.

4.8 Optical Properties of Silicon Alloys

From sections above, it has been proven that P atoms are incorporated into different silicon alloy films by Cat-doping, thus improve the electrical conductivity of these films. However, it is also well known that extra free charge carriers inside the films could cause extra parasitic absorption in the films, which is called free carrier absorption (FCA) [115–117]. The free carrier absorption is even a more important issue when the Cat-doped layers are intended to be used as window layers. Therefore, in this section the optical properties (absorption coefficient α)of silicon alloy films was investigated by photothermal deflection spectroscopy (PDS) while Cat-doping was applied. The absorption change due to free carriers is determined by [115]:

$$\Delta\alpha = \frac{e^3\lambda^2}{4\pi^2c^3\epsilon_0 n}[\frac{\Delta N_e}{m_{ce}^{*2}\mu_e} + \frac{\Delta N_h}{m_{ch}^{*2}\mu_h}] \tag{4.8}$$

where λ is the wavelength, ΔN_e is the change of electron density, ΔN_h is the change of hole density, e is the electronic charge, ϵ_0 is the permittivity of free space, n is the refractive index , m_{ce}^{*2} is the conductivity effective mass of electrons, m_{ch}^{*2} is the conductivity effective mass of holes, μ_e is the electron mobility, and μ_h is the hole mobility. From Eq.4.8, $\Delta\alpha$ is proportional to λ^2 and change of carrier density (ΔN), so with increase of free charge carriers the absorption will increase. Meanwhile, $\Delta\alpha$ becomes more significant at long wavelength or low energy range at around 1 eV due to the square factor on λ.

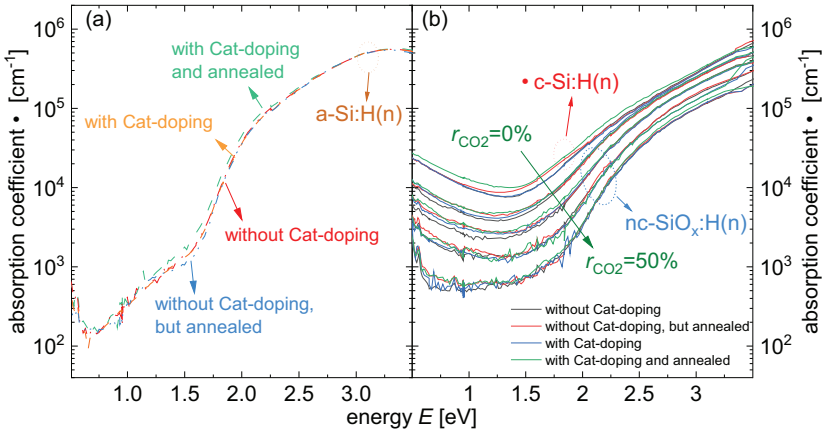

Figure 4.19: *Absorption coefficient α of different silicon alloy films measured by PDS: (a): a-Si:H(n) and (b): µc-Si:H(n) and nc-SiO_x:H(n) prepared with various r_{CO_2}. Films from each kind were post-deposition treated in four ways: without Cat-doping is the as-grown untreated film, without Cat-doping but annealed means the sample was only annealed at 220 °C, with Cat-doping means that the sample went through one Cat-doping process, with Cat-doping and annealed means the samples was annealed at 220 °C after going through the Cat-doping process*

Different absorption coefficients corresponding to energy are plotted in Figure 4.19. For clarity only the α of a-Si:H(n) film is shown in Figure 4.19(a). Comparing samples with four different post-deposition treatments, there is no significant difference in α. From P profiles in Figure 4.11(a) and charge carrier density profiles in Figure 4.12(a), there is no large increase in N_{P} and N_{c}, therefore the FCA due

to Cat-doping inside the a-Si:H(n) film could be ignored. When Cat-doping was applied on μc-Si:H(n) and nc-SiO$_x$:H(n) with r_{CO_2} from 10% to 50%, it seems that there is increase in α at the low energy range, but the increase is quite minor. When the initial value of α is low, more noise can be seen making it hard to distinguish the possible change in α. Nevertheless, the increase in α is quite slight and the effect of increased light absorption still needs to be tested in a device.

5 Improving Passivation Quality by Catalytic-doping

In chapter 4, the impact of Cat-doping on material properties are discussed. In this chapter, we are going to further look into the influence of Cat-doping on the passivation before the implementation in SHJ solar cells. Therefore, passivation stacks with different silicon alloys were prepared and Cat-doping was applied onto different interfaces in the passivation stack. The passivation quality of these stacks were characterized as effective minority carrier lifetime (τ_{eff}) and implied open-circuit voltage (iV_{oc}) measured by Photoconductance lifetime tester (Sinton WCT-120). Firstly, different gases were used during Cat-doping to distinguish different effects. Then silicon alloy materials were used in the passivation stacks to compare the effectiveness of Cat-doping. At last, the Cat-doping parameters were varied for an optimal Cat-doping conditions.

5.1 Three effects during Cat-doping

At first, three effects may co-exist during the Cat-doping process: (i) thermal annealing effect, (ii) hydrogenation, and (iii) phosphorous doping [90]. Three different gases, i.e. Ar, H_2 and PH_3, were used during the Cat-doping process to distinguish the significance of three above-mentioned effects. Symmetric passivated samples with the a structure of 10 nm μc-Si:H(n)/5 nm a-Si:H(i)/c-Si(n)/5 nm a-Si:H(i)/10 nm μc-Si:H(n), referred as *S1* in Figure 5.2, were used. The increase ($\Delta\tau_{\text{eff}}$) in τ_{eff} is shown in Figure 5.1. The τ_{eff} increases by 0.4 ms and 0.9 ms respectively when Ar and H_2 were used. The largest τ_{eff} increase of 1.2 ms was achieved when PH_3 was used.

Using Ar atmosphere, we assume similar heat convection inside the HWCVD chamber compared to that during the actual Cat-doping treatment, but without the effects from hydrogen radicals and phosphorous dopants. Therefore, the increase of 0.4 ms in τ_{eff} could be attributed to the thermal impact of Cat-doping treatment and represents 33% of the total increase in τ_{eff} of 1.2 ms. Using a H_2 atmosphere, combines thermal effect and hydrogenation effect. Consequently, since the treatment increases τ_{eff} by 0.9 ms, 0.5 ms of the increase arise likely from the effect of hydrogenation. Using PH_3 atmosphere finally resulted in the highest increase of 1.2 ms in τ_{eff} where all three above-mentioned effects are combined. However, it is not possible to clearly derive the portions of all three effects for the treatment with atmosphere of 2.25% PH_3 in He. Annealing might have a major effect, increasing τ_{eff} in the range of one third, but the portions of hydrogenation, arising from hydrogen radicals, and increased doping, arising from phosphorous radicals, remain unknown or could be assumed the same as for the use of H_2 gas only. Nevertheless, the use of PH_3 showed the highest improvement of τ_{eff} with an increase of 1.2 ms. This result confirmed that, with the use of PH_3 gas, all three effects co-exist and account for the improvement in τ_{eff}.

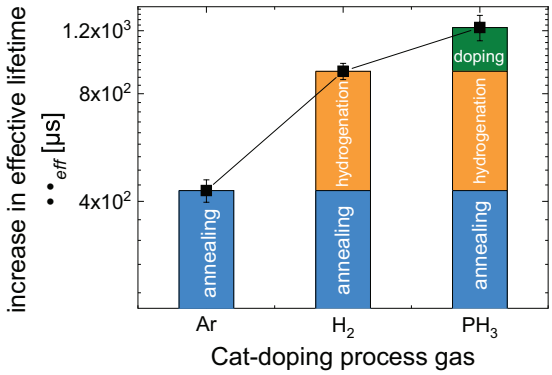

Figure 5.1: *Increase in effective lifetime $\Delta\tau_{eff}$ on passivated samples with μc-Si:H(n) after Cat-doping using three different gases. The color strips indicate the portion of three different effects during Cat-doping: thermal annealing, hydrogenation and P doping. However, for the use of PH_3, it is assumed that the hydrogenation effect is the same as for the use of H_2 gas only*

5.2 Cat-doping on doped silicon alloy films

Silicon alloys, i.e. μc-Si:H(n), nc-SiO_x:H(n) and μc-SiC:H(n), are good candidates for the use in SHJ solar cells for their superior electrical and optical properties. Cat-doping on these silicon alloy films has shown that additional P atoms can be incorporated into the films after film deposition by Cat-doping, thus improve the electrical conductivity while not deteriorating the optical advantage. However, the influence on passivation quality when Cat-doping is applied onto these films needs more investigation.

5.2.1 Comparing three silicon alloys

Symmetric passivated samples with different n-type silicon alloy films (μc-Si:H(n), nc-SiO_x:H(n) and μc-SiC:H(n))were prepared and Cat-doping processes were applied onto the silicon alloy films, as shown in Figure 5.2 on the left side. They have structures of 10 nm μc-Si:H(n)/5 nm a-Si:H(i)/c-Si(n)/5 nm a-Si:H(i)/10 nm μc-Si:H(n) and 20 nm nc-SiO_x:H(n)/8 nm a-Si:H(i)/c-Si(n)/8 nm a-Si:H(i)/20 nm nc-SiO_x:H(n), hereafter referred to *S1* and *S2*, respectively. Here, nc-SiO_x:H(n) with r_{CO_2}=30% was used in *S2*. For μc-SiC:H(n), after HF dipped, the wafers were dipped into HNO_3 at 23 °C for 10 min for the formation of a thin SiO_2 layer with a thickness of ∼1.5 nm. The thin SiO_2 layer was used to passivate the c-Si surface [83]. The passivated samples for μc-SiC:H(n) has a structure of 23 nm μc-SiC:H(n)/ 1.5 nm SiO_2/ c-Si(n)/ 1.5 nm SiO_2/ 23 nm μc-SiC:H(n), hereafter referred to *S3*.The τ_{eff} before and after Cat-doping was obtained on the same samples, shown in Figure 5.2 on the right side. Here the P Cat-doping process was carried out on both sides of the samples on the surfaces of the silicon alloys. The τ_{eff} of *S1* increases from 3.4 ms to 4.6 ms after P Cat-doping. The τ_{eff} of *S2* and *S3* before Cat-doping are 1.1 ms and 2.1 ms, respectively. After Cat-doping the τ_{eff} of *S2* and *S3* remain unchanged.

As discussed in Sec.5.1, three effects co-exist during a Cat-doping process and together might impact the passivation quality. The conductivity and P profile of three silicon alloy films discussed in Sec.4.6 show that different amount of P atoms are incorporated into the film and P atoms are activated differently. For μc-Si:H(n),

it has large increase in N_P which is reflected in the increase in σ. The improvement in N_P could change the doping level (N_c) of the μc-Si:H(n) layers, thus the Fermi energy level (E_F) is moved closer to the conduction band (E_C). This change in the band diagram reduces the barrier height for electron and enhances the surface field effect [16], therefore improves the τ_{eff}. For *S2* with nc-SiO_x:H(n) and *S3* with μc-SiC:H(n) films, the increase in N_P and N_c in silicon alloy films is very small due to their material properties. The negligible change in the doping level makes the P doping effect from Cat-doping insignificant for *S2* and *S3*. Meanwhile, the other two effect, thermal annealing and hydrogenation, don't seem to play a big role for *S2* and *S3* either. Other factors, such as passivation from the a-Si:H(i) layer and SiO_2, might be the limitation for τ_{eff}.

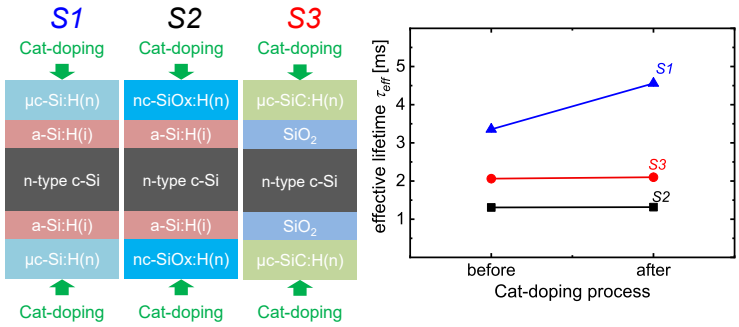

Figure 5.2: *Sketches of passivated samples with different silicon alloy films on the left side together with τ_{eff} of these stacks before and after Cat-doping. For convenience, the samples with μc-Si:H(n) layers are referred as S1, the samples with nc-SiO_x:H(n) layers are referred as S2 and the samples with μc-SiC:H(n) are referred as S3. Different from S1 and S2 where a-Si:H(i) films are used as passivation layer, in S3 the wet-chemical SiO_2 layers are used as passivation layer [83]. τ_{eff} has an error of 10% but it is smaller than the symbols in the graph.*

5.2.2 Cat-doping on n-type microcrystalline silicon

In Sec.4.3.2, Cat-doping was applied on μc-Si:H(n) to improve the conductivity of the films. However, the influence of Cat-doping on the passivation quality of stacks with μc-Si:H(n) is not clear yet. Here, symmetric passivated stacks with μc-Si:H(n)

layers were fabricated (same as *S1* in Figure.5.2). Cat-doping processes were done onto both sides, followed by effective lifetime measurement. First, μc-Si:H(n) layers were prepared with different plasma powers to check Cat-doping on different μc-Si:H(n) films. The results are shown in Figure 5.3(a). It is observed that τ_{eff} decreases from 1.2 ms to 1.0 ms as the plasma power of the μc-Si:H(n) increases from 10W to 50W even though all the μc-Si:H(n) have very similar material properties. This decrease in τ_{eff} with increasing plasma power could be thus sorely associated to the enhanced ion bombardment during the deposition of μc-Si:H(n), which seems to deteriorate the quality of the a-Si:H(i) passivation layers underneath of it, leading to lower τ_{eff}. After P Cat-doping on the μc-Si:H(n) of both sides, it is found that τ_{eff} increases for all samples. It is noteworthy that the τ_{eff} improvement is also significant even for the μc-Si:H(n) fabricated with a plasma power of 50 W. Given that the σ_{Cat} of μc-Si:H(n) increases after P Cat-doping (see Figure 4.5(b)), the increase in τ_{eff} for all samples after P Cat-doping seems largely correlated to the enhanced field-effect passivation [118]. On the other hand, the lifetime improvement could also be due to hydrogen passivation. Matsumura et al. found that the H treatment on Si wafers in HWCVD improved the lifetime of a-Si:H(i) passivated c-Si wafers [89]. They argued that the improvement could be probably due to the moderate etching of the defective parts of c-Si surfaces and/or the effective termination of dangling bonds on the c-Si surfaces. Therefore, it is reasonable to think that the released H atoms from PH_3 by the catalytic decomposition process in part passivate defects of the μc-Si:H(n), leading to the lifetime improvement.

Figure 5.3(b) shows the τ_{eff} of the symmetric passivated samples before and after P Cat-doping at different T_{f}. In this case, μc-Si:H(n) film was fabricated with a plasma power of 10 W. The initial τ_{eff} without any post processes was around 0.6 ms. In Figure 5.3(b), it can be clearly seen that the τ_{eff} of all samples increases after P Cat-doping. As T_{f} increases from 800 to 1200 °C, the rate of increase of τ_{eff} tends to go up continuously and begin to decrease as T_{f} increase from 1000 to 1200 °C. Consequently, the highest τ_{eff} of 1.2 ms was achieved at a T_{f} of 1000 °C. There are three possible reasons for this tendency. Firstly, at higher T_{f}, PH_3 is more decomposed into P and H radicals and subsequently they are incorporated to the surface of samples. Each of these P and H radicals leads to field effect passivation

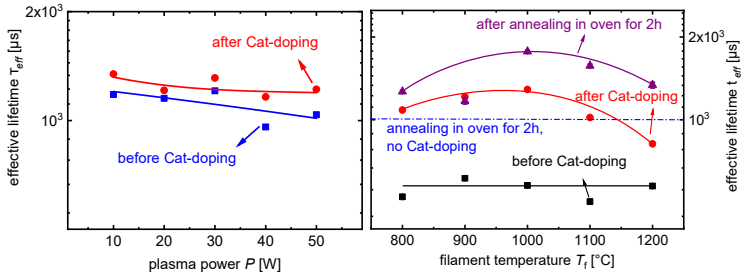

Figure 5.3: *Effective lifetime τ_{eff} of symmetric passivated stacks with µc-Si:H(n) layers (a): µc-Si:H(n) layers were deposited at different plasma power from 10 to 50 W, Cat-doping was performed on both sides and τ_{eff} was measured before and after; (b): passivated stacks with µc-Si:H(n) prepared at plasma power of 10 W, Cat-doping was done at different T_f from 800 °C to 1200 °C on both sides of the stacks, the samples were also annealed after Cat-doping at 220 °C for 2 hours; one reference sample was included which was annealed without Cat-doping, the blue dash line represents the τ_{eff} of the reference sample after annealing. The solid lines act as guide lines for the eyes*

and dangling bond passivation, respectively, leading to the lifetime improvement. However, the kinetic energy and flux of H radicals increase as well with increasing T_f, which can promote the H etching substantially [12]. Thus, at higher T_f, the enhanced H etching could counteract the passivation, leading the τ_{eff} improvement to be compromised. Secondly, the decomposition efficiency of PH_3 might not linearly increase in this condition as T_f increases. When T_f is very high, the numbers of P and H radicals might not be proportional to T_f due to saturated decompose efficiency. Thirdly, the surface temperature of the samples could increase with increasing T_f, probably leading to hydrogen effusion.

After τ_{eff} measurements, the samples were annealed at 220 °C in air for 2 hours. When T_f of 1000 °C was applied, the τ_{eff} increases from 0.6 ms to 1.2 ms after P Cat-doping and from 1.2 to 2 ms after annealing, as shown in Figure 5.3(b). The τ_{eff} of the sample without P Cat-doping increases from 0.6 ms to 1.1 ms after annealing, with an increase of 0.5 ms in τ_{eff}. As two samples went through the same annealing process, the increase in τ_{eff} for both sample is supposed to same. However, for the sample with Cat-doping, τ_{eff} first increased 0.6 ms from Cat-doping and then again

0.8 ms from annealing, which is larger than the sample without Cat-doping. This could be that the sample with Cat-doping has more H inside the sample to passivate dangling bonds and P atoms are further activated during the annealing process, leading to enhanced field passivation effect. Nevertheless, it seems obvious that the τ_{eff} improvement for the sample with P Cat-doping at a T_{f} of 1000 °C is originated from both the improvement of a-Si:H(i) passivation layer quality and incorporation of P into the film during Cat-doping process. The improvement of a-Si:H(i) passivation quality could originate from annealing and hydrogenation effects, which moves the H inside the films and add more H atoms to passivate the surface, respectively. This result also agrees well with the three effects discussed in Sec.5.1.

5.2.3 Cat-doping on n-type microcrystalline silicon oxide

Cat-doping was also applied on nc-SiO_x:H(n) films in Sec.4.5 where different r_{CO_2} was used and the σ of these films increases slightly after Cat-doping. In this section, symmetric passivated samples with a structure as shown in Figure 5.4(a) were prepared. The τ_{eff} results before and after Cat-doping are shown in Figure 5.4(b). The τ_{eff} for all the samples increased after Cat-doping, but with different significance. For samples with nc-SiO_x:H(n) layer from different r_{CO_2}, τ_{eff} locates around $4 \sim 6$ ms and only increases slightly after Cat-doping. Considering the 10% error of the effect lifetime measurement, the tiny increase in τ_{eff} for samples with nc-SiO_x:H(n) can be ignored. For samples with a-Si:H(n) and μc-Si:H(n), the increase in τ_{eff} is from 1.1 ms to 1.6 ms and 3.9 ms to 7.3 ms ,respectively, which is larger than that for samples with nc-SiO_x:H(n) layers.

As discussed in Sec.4.5, the conductivity change for nc-SiO_x:H(n) films after Cat-doping is very small, which is likely due to the low activation ratio of P atoms. Therefore, among the three effects from Cat-doping: thermal annealing, hydrogenation and P doping, the P doping doesn't seem to play a big role to impact the passivation quality. From $\Delta\tau_{\text{eff}}$, the other two effects don't influence the passivation quality largely either. The limitation of the passivated samples with nc-SiO_x:H(n) might lay in the a-Si:H(i) layer passivation or the deposition conditions of the nc-SiO_x:H(n) layers, which could cause damage to the a-Si:H(i) layer underneath. For passivated

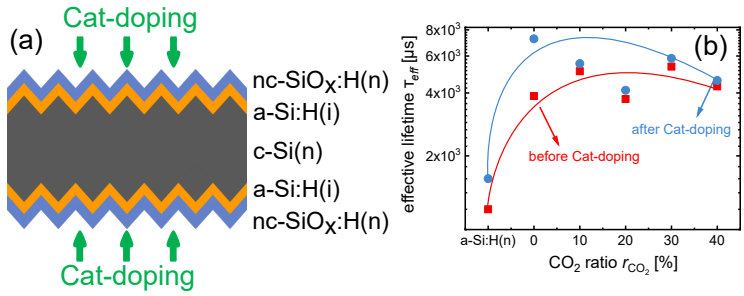

Figure 5.4: *Sketch of the passivated samples in (b), double side textured wafers were used as substrate and a-Si:H(i) layers were deposited on both sides before nc-SiO_x:H(n) and effective lifetime τ_{eff} of symmetric passivated stacks with nc-SiO_x:H(n) layers in (a): nc-SiO_x:H(n) layers were deposited with different r_{CO_2}, Cat-doping was performed on both sides and τ_{eff} was measured before and after. The solid lines act as guide lines for the eyes*

samples with a-Si:H(n) layers, there is slightly larger $\Delta\tau_{\text{eff}}$. The reason could be mainly attributed to the annealing effect and hydrogenation effect. In Figure 4.11(a) and 4.12(a), the increase in both N_{P} and N_{c} is very small, thus leads to the insignificant P doping effect . On the contrary, for passivated samples with μc-Si:H(n) layers, the enormously increases in τ_{eff} from 3.9 ms to 7.3 ms could come from the significant P doping effect when there is an increase in N_{P} and N_{c} of μc-Si:H(n) films. However, as discussed in Sec.5.1, the accurate portion of each effect is hard to distinguish.

Even though the improvement in τ_{eff} varies a lot, Cat-doping is confirmed being able to improve the passivation quality of stacks containing different silicon alloy films. Under current Cat-doping condition, passivated samples with μc-Si:H(n) film has the largest improvement in electrical property and passivation ability than other silicon alloy films. In the cases of other films, the limitation is various, such as low activation ration of P atoms in a-Si:H(n) and nc-SiO_x:H(n) films, small amount of P atoms that can be incorporated into μc-SiC:H(n) films. Furthermore, the limitation to further improve passivation quality may also come from fabrication of other layers or interfaces. To improve the passivation quality even more for all these passivated samples, all the layer and interface properties should be considered and the limitation

should also be identified clearly.

5.2.4 Cat-doping through SiO_2

The amount of P atoms that can be incorporated into μc-SiC:H(n) film is much smaller than that for other silicon alloy films, therefore the surface field effect enhancement introduced by Cat-doping is negligible. This is confirmed in Figure 5.2. However, Cat-doping can still be used in μc-SiC:H(n) related device. Figure 5.5(a) shows the structure of a passivated sample to test the passivation quality prior to the application of μc-SiC:H(n) in SHJ solar cells. Here, instead of using Cat-doping on the surface of μc-SiC:H(n) layers, Cat-doping was used onto the surface of SiO_2 layers. It has been reported that the P atoms can be incorporated into silicon through silicon oxide (SiO_x) films if the thickness of SiO_x is not too large($<$ 7 nm) [12]. Moreover, Cat-doping was shown to improve the passivation quality when used onto surface of c-Si wafer [16, 89] by both H and P radicals from Cat-doping. The H radicals are helpful to passivate the dangling bonds and the P radicals inside the wafer surface lower the barrier height for electrons. The wet chemical prepared SiO_2 has only a thickness of 1.5 nm, so the increase in N_P near wafer surface could be large. Meanwhile, the passivation quality could be more sensitive to the Cat-doping conditions. Here, the T_f of Cat-doping was altered from 800 °C to 2000 °C. The τ_{eff} of the passivated sample without Cat-doping is 3 ms. When Cat-doping was used, the τ_{eff} of the samples is first improved to 4 ms with T_f below 1000 °C then declined with T_f above 1000 °C. The improvement of τ_{eff} could be attributed to the three effects during Cat-doping. However, when T_f is higher than 1000 °C, the effect of Cat-doping on passivation turns to negative and the τ_{eff} intends to decrease below 1 ms with the rise of T_f up to 2000 °C. At higher T_f during Cat-doping, the substrate was found to be etched by the H radicals [12]. Likewise in the case of Cat-doping through the thin SiO_2 layer, the SiO_2 could be etched away when high T_f was used. Consequently, the underneath c-Si surface could be damaged results in deteriorated τ_{eff}. Therefore, no higher than T_f of 1000 °C during the Cat-doping should be used to dope through thin SiO_2.

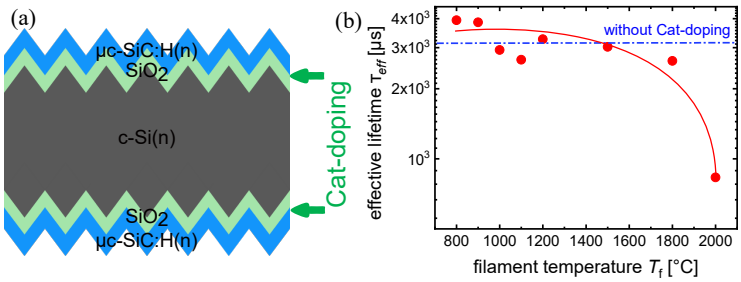

Figure 5.5: *Effective lifetime τ_{eff} of symmetric passivated stacks with μc-SiC:H(n) layers in (a): different T_f during Cat-doping were used; a reference value is indicated as blue dash line representing the sample without Cat-doping. (b): sketch of the passivated samples with SiO_2 layers. The 1.5 nm SiO_2 layer on both sides were wet chemical prepared. Cat-doping was performed on both sides prior to the deposition of μc-SiC:H(n) and τ_{eff} was measured on the complete stacks*

5.2.5 Cat-doping on intrinsic amorphous silicon

In former sections, Cat-doping was mainly used on n-type doped silicon alloy films to further increase the electrical conductivity, enhance the surface field effect and improve interface passivation. In this section, Cat-doping is tested on a-Si:H(i) layers in a solar cell precursor to evaluate the impact on passivation quality of the cell precursor. The structure of the samples are illustrated in Figure 5.6(d), where in the front side only a-Si:H(i) with different thicknesses were deposited. Since there is only a thin layer of a-Si:H(i) between the c-Si surface and H radicals from Cat-doping, the H radicals may deteriorate the passivation on c-Si surface and reduce the τ_{eff}. Therefore, different thicknesses of a-Si:H(i) was used to investigate the relation between the a-Si:H(i) thickness and passivation quality when Cat-doping was used.

With different thickness of a-Si:H(i) and Cat-doping applied on them, the τ_{eff} is shown in Figure 5.6(a-c). First of all, the initial τ_{eff} of these samples fluctuates slightly around 1 ms. After Cat-doping, the values stay almost unchanged for all samples with three different thicknesses. From the discussion in Sec.5.1, due to the co-existence of thermal annealing, hydrogenation and P doping, the τ_{eff} of these samples in principle should be improved. However, despite the use of higher T_{f} which

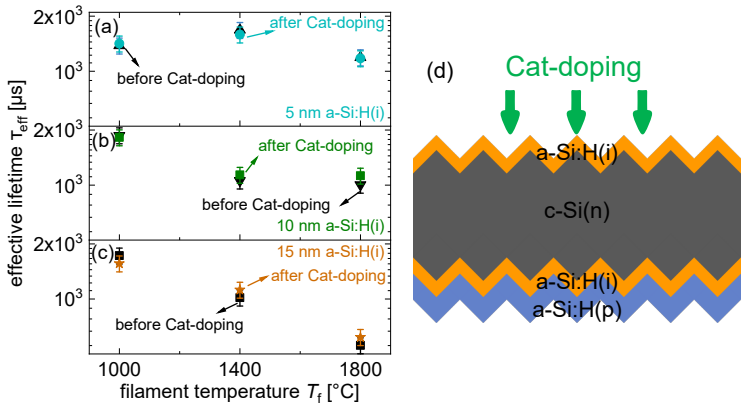

Figure 5.6: *Sketch of solar cell precursor with only a-Si:H(i) layer on the front and a-Si:H(i)/a-Si:H(p) on the backside in (d); here different thicknesses (5, 10, 15 nm) of a-Si:H(i) were used; Cat-doping was done to the surface of a-Si:H(i) layer on the front and τ_{eff} was measured both before and after Cat-doping. The τ_{eff} of cell precursors with different thicknesses of a-Si:H(i) is shown in (a-c). The black points are τ_{eff} for samples before Cat-doping and the colored ones are after Cat-doping.*

results in higher N_P in the films and enhanced field effect, the τ_{eff} stays unchanged. It has been proved that the H radicals from Cat-doping can etch the silicon substrate [12], therefore when there is only thin a-Si:H(i) layers on top of c-Si surface, the enhancement of passivation from Cat-doping could be compensated by the damage from H radical etching. Meanwhile, τ_{eff} could also be limited by the deposition condition that determines the property of a-Si:H(i) layer, which consequently limits the ability of a-Si:H(i) layer to passivation the c-Si surface. Nevertheless, Cat-doping doesn't deteriorate the passivation quality when applied on the a-Si:H(i) passivation layer. Moreover, the increase in σ still exists and can benefit the electrical transport in a cell. The effect in cells will be discussed in detail in Chapter 6.

6 Catalytic-doping in Silicon Heterojunction Solar Cells

Cat-doping has been studied on many materials [12, 13, 90] and interfaces in devices [118–120]. However, the study and application in SHJ solar cells is very limited and no high efficiency has been achieved [16, 120]. In this chapter, the feasibility and potential of implementing Cat-doping in SHJ solar cells with various silicon alloy films is discussed. At first, Cat-doping with the same parameter was applied on cells with different silicon alloy films for comparison. Then different Cat-doping conditions were tested in cells with different silicon alloy films. At last, a different approach, where Cat-doping on a-Si:H(i) was used to replace the deposition of a-Si:H(n) layers, thus reduce parasitic absorption, was investigated.

6.1 Silicon heterojunction solar cells

Silicon heterojunction (SHJ) solar cells have been widely researched both in laboratory and industry levels for its high efficiency, simple fabrication procedure and low production cost [3, 7, 17, 18]. In SHJ solar cells, stack with intrinsic amorphous silicon (a-Si:H(i)) and doped amorphous silicon (a-Si:H(n/p)) layers are used on both sides to passivate the crystalline silicon wafer [5, 17, 121]. The excellent passivation quality provides high open-circuit voltage (V_{oc}) for the cell and very high efficiency solar cells have already been reported using or based on SHJ structure [4, 105, 121]. However, there are still several problems with SHJ solar cell to be solved on its way to higher efficiency. The first one is that a-Si:H(n/p) layers are used in the front as surface field layer or emitter, which cause parasitic absorption especially in the short wavelength range [4, 21]. Many new materials and structures have

been explored to replace the a-Si:H(n/p) layers in the front, such as wide bandgap materials [10, 11, 32, 84], transition metal oxide [6, 34, 35] and back-contacted structure [4, 21]. The second problem is that to guarantee sufficient passivation, a certain thickness of a-Si:H(i) is required. The a-Si:H(i) layer with poor conductivity, however, is a barrier for charge carrier collection and limit the fill factor (FF) in SHJ cells [17, 27].

Figure 6.1(a) shows the typical structure of a rear emitter SHJ solar cells. It consists of a double-side a-Si:H(i) passivated c-Si wafer, doped a-Si:H layers as emitter or surface field layer, ITO and Ag on both sides which are used to extract carriers. Figure 6.1(b) shows the results of the SHJ cell including the J-V curve and also the light response spectrum (EQE, IQE, R). It can be seen that the cell has low efficiency at that time due to low J_{sc} and low FF. This cell type acts as a baseline for this work and it should be mentioned that the development of this cell type was continuously done to improve the efficiency. Therefore, the work discussed below is always based on the up-to-date baselines in our laboratory at that time, which means the improved baseline as reference can be seen. Nevertheless, the aim of implementing Cat-doping in SHJ solar cells is always to improve the performance based on the up-to-date cells.

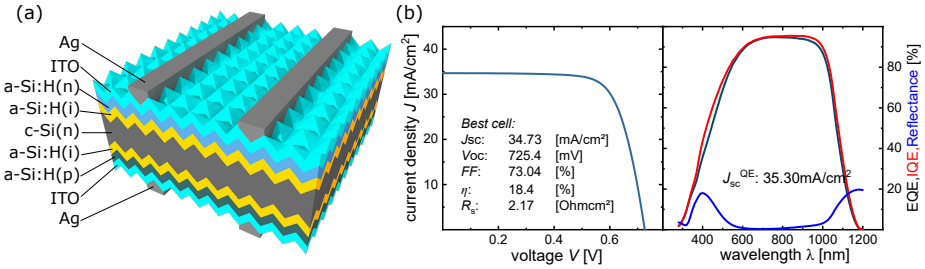

Figure 6.1: *Typical structure of a SHJ solar cell in (a) consisting of a-Si:H(i) passivated c-Si wafer, doped a-Si:H layers, ITO and Ag grids to extract carriers; (b) is the result of the cells including the J-V curve as well as the light spectrum information*

To solve the problems mentioned above, different methods have been studied [4, 6, 10, 11, 21, 32, 34, 35, 84]. In this work, we implemented two silicon alloys, i.e. μc-Si:H

and nc-SiO_x:H, for better light absorption while applying Cat-doping to overcome the intrinsic limitation of these materials. New concepts based on conventional SHJ solar cells were also studied to explore the potential of Cat-doping in improving the efficiency of SHJ solar cells.

6.2 Cat-doping on different n-type silicon alloys

SHJ solar cells were prepared with different silicon alloys and Cat-doping were also applied on the n-layer in the front to have a first insight of the impact from Cat-doping. The results are shown in Figure 6.2. Here, the cell structure is the same as illustrated in Figure 6.1(a), but a-Si:H(n), μc-Si:H(n) and nc-SiO_x:H(n) with different r_{CO_2} were used in the front as n layer. Firstly, comparing cells without Cat-doping, it can be seen that the η is going down slightly from 18.9% to 18.4% as the n layer changes from a-Si:H(n) to μc-Si:H(n); then the η goes up to 19.0% when nc-SiO_x:H(n) layers with different r_{CO_2} are used, but when further increase r_{CO_2} the η decreases to 17.7%. The V_{oc} has the same change as in η, but the fluctuation is relative. The J_{sc} increases significantly from 36.2 to 37.2 mA/cm^2 when nc-SiO_x:H films were used and with higher r_{CO_2} the J_{sc} is higher. On the contrary, the FF decreases as the r_{CO_2} increases. It has already be mentioned in Sec. 4.5 that for nc-SiO_x:H films the transparency increases and conductivity decreases as the O content increases. Therefore, when r_{CO_2} increases the nc-SiO_x:H(n) films become more transparent and less conductive, resulting in higher J_{sc} and lower FF.

When Cat-doping was applied onto the n layers in the front, the η of all the cells with different n layers was improved. The improvement mainly comes from the improved V_{oc} and FF. The V_{oc} increases is likely due to three effects that happens during the Cat-doping process, i.e. thermal annealing, hydrogenation and P doping, which is discussed in Sec. 5.1 The improved FF might also be attributed to Cat-doping, after which the various n layer become more conductive and the R_{s} in return is reduced. However, the J_{sc} drops slightly probably due to the increased recombination loss in the n layers when the doping increases.

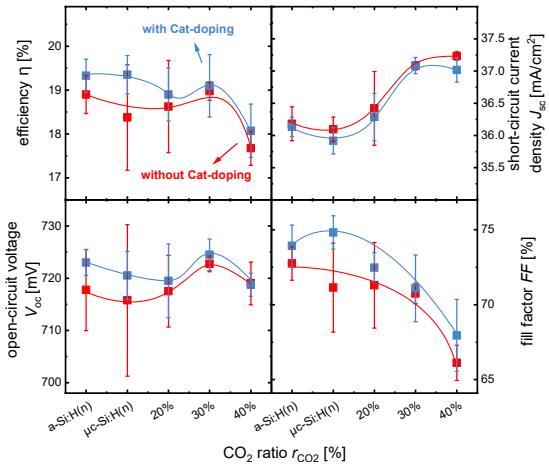

Figure 6.2: *Results of SHJ solar cells with different silicon alloys. The red ones represent cells without any special treatment and the blue ones are cells with Cat-doping applied onto different n-layers in the front. The large scatter may come from the evaporated Ag grid.*

For a close look into the light absorption in cells with different n layers, the IQE of these cells are shown in Figure 6.3(a). It clearly shows that with increase of the r_{CO_2}, the light absorption in the short wavelength range is improved due to the nc-SiO$_x$:H becomes more transparent. In Figure 6.3(b) is the IQE of these cells with and without Cat-doping in the short wavelength range, it can be seen that the absorption is slightly reduced after Cat-doping. After Cat-doping, the n layer becomes more conductive and has more free carriers, therefore the reduced absorption could be attributed to the increased recombination loss in the front n layer.

As proved above that Cat-doping could be used to improve the η of SHJ solar cells with different n layers, more detailed study of further optimization of Cat-doping were carried out in the following. Firstly, different Cat-doping conditions were tested on the μc-Si:H(n) layers, then Cat-doping was optimized for application on nc-SiO$_x$:H(n) layer aiming at improving the trade-off between conductivity and transparency of nc-SiO$_x$:H(n) films. At last, Cat-doping on a-Si:H(i) layers for the use in SHJ solar cells was tested.

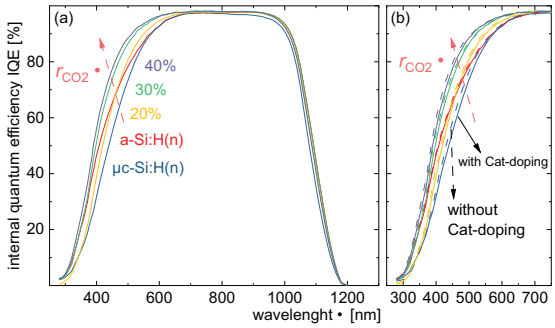

Figure 6.3: *IQE spectrum of cells with different n layers in (a) and IQE in the short wavelength range of cells with and without Cat-doping in (b): all the solid lines are from cells with Cat-doping and all the dash lines are from cells without Cat-doping*

6.3 Cat-doping on μc-Si:H(n)

Microcrystalline silicon is an appealing alternative for the front a-Si:H carrier selective contacts because its absorption coefficient at short wavelengths is much lower than that of a-Si:H leading to lower parasitic absorption. In addition, the conductivity of μc-Si:H is considerably higher than that of a-Si:H, which reduces series resistance. However, the conductivity of μc-Si:H is largely dependent on its crystallinity and doping concentration. The crystallinity of μc-Si:H tends to be suppressed as dopant gas flow increases [43, 122, 123]. As a result, the deposition conditions of μc-Si:H are usually compromised at optimal trade-off, which limits the conductivity of μc-Si:H. Here, for the first time Cat-doping is applied on the μc-Si:H(n) layer in SHJ solar cells to improve the electrical property as well as cell performance.

6.3.1 Effect of filament temperature

The results of Cat-doping with different T_f on cells with μc-Si:H(n) are shown in Figure 6.4. It can be seen that after Cat-doping, all η increased and with higher T_f the η is higher. The reference cell has a η of 17.7% and when Cat-doping was applied, the η increases to 18.4% at T_f of 1000 °C and reaches 19.5% at T_f of 2200 °C. The improvement of η comes from slightly increase in J_{sc}, slightly increase in

V_{oc} and largely improved FF. It has been mentioned in Sec.6.2 that increased N_P in the front n layer give rise to the recombination loss in the front due to free carrier absorption. However, here is the not case since the J_{sc} increases from 35.3 mA/cm^2 at T_f of 1000 °C to 36.2 mA/cm^2 at T_f of 2200 °C, which is contradictory to the conclusion before. Therefore, other reasons might exist that account for the slightly increase in J_{sc}. It has been confirmed that high T_f results in etching of the silicon films [12], so the slight improved J_{sc} is likely to be attributed to the etching of the μc-Si:H(n) films in the front when Cat-doping was carried out at high T_f. Similarly, the V_{oc} was also improved from 693 mV of the reference cell to 706 mV of the cell with Cat-doping at T_f of 1000 °C; then continuously improved to 712 mV at T_f of 2200 °C. As mentioned before, the improved V_{oc} is a result of three effects that happen during the Cat-doping process. Meanwhile, advancement is also seen in FF as it was enhanced from 72.3% from the reference cell to 75.7% from the cell with Cat-doping at T_f of 2200 °C. The advancement in FF is the result of improved conductivity of the μc-Si:H(n) layers in the cell. This is in very good agreement with the N_P and N_c study in Sec. 4.3 that μc-Si:H(n) films becomes more conductive when applying Cat-doping, which decreases the R_s and gives better FF.

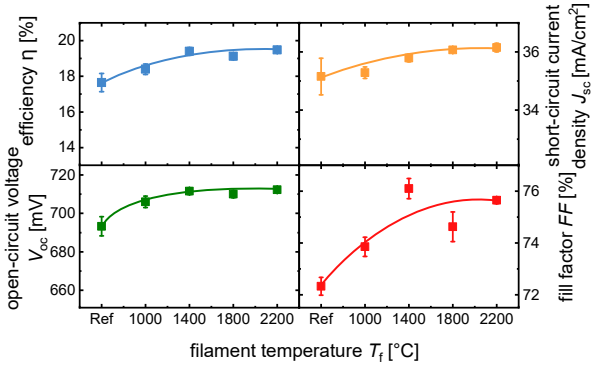

Figure 6.4: *Results of cells with Cat-doping at different T_f on μc-Si:H(n) in SHJ solar cells. A reference cell without Cat-doping was also included for comparison and Cat-doping processes were performed with T_f varying from 1000 °C to 2200 °C, the T_{sub} is 200 °C and pressure is 0.01 mabr for all Cat-doped cells*

6.3.2 Effect of substrate temperature

Beside T_f during Cat-doping process, another important parameter is T_{sub} as it also influences the thermal condition inside the chamber and the doping effect of P [97]. Therefore, different T_{sub} were used during the Cat-doping process to investigate the effect of T_{sub}. Figure 6.5 shows the cell results. Comparing to the reference cell without Cat-doping, the η from cells with Cat-doping first increases and then gradually decreases. At T_{sub} of 150 to 200 °C, the η reaches the highest 18.8%, then declines to 16.2% at T_{sub} of 250 °C. The reason for the unexpected bad performance at T_{sub} of 300 is yet unclear, but probably due to the bad wafer quality in this sample. The same trend exists for V_{oc} as it also first increases and then decreases. The reasons why the V_{oc} is improved upon application of Cat-doping, from 693 mV to 706 mV, could largely be attributed to the three effects during Cat-doping.

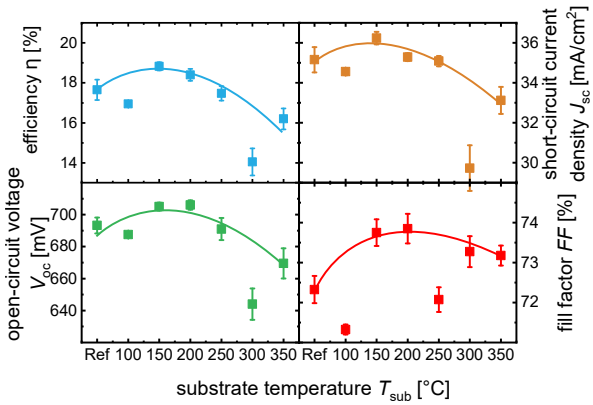

Figure 6.5: *Results of cells with Cat-doping at different T_{sub} on μc-Si:H(n) in SHJ solar cells. A reference cell without Cat-doping was also included for comparison and Cat-doping processes were performed with T_{sub} varying from 100 °C to 350 °C, the T_f is 1000 °C and pressure is 0.01 mbar for all Cat-doped cells*

However, when applying higher T_{sub} the V_{oc} tends to decrease to 670 mV, the possible explanation could be: (1) at higher T_{sub}, lower N_P could be reached (as shown in Sec. 4.3), resulting in less significant field effect; (2) at higher T_{sub} the H starts to effuse out of the film, deteriorating the passivation at the interface and compensating the improvement from Cat-doping effects. For FF, it was first

improved up to 73.9% possibly due to the P doping and then reduced to 73.2%, but still higher than 72.3% from the reference cell. This again confirms the effectiveness of Cat-doping upon improving the electrical transport in the cell and the FF, which also agree with the material study in Sec. 4.3. In the following work, the T_{sub} was set to 200 °C if not mentioned otherwise.

6.3.3 Effect of processing pressure

Apart from T_{f} and T_{sub}, processing pressure is another important issue that could influence the effectiveness of Cat-doping since it directly changes the PH_3 molecules source inside the chamber. Thus, different pressures were used to test the change in cell performance. The results are illustrated in Figure 6.6 and the results again confirm that Cat-doping is valid to improve the η of the cells.

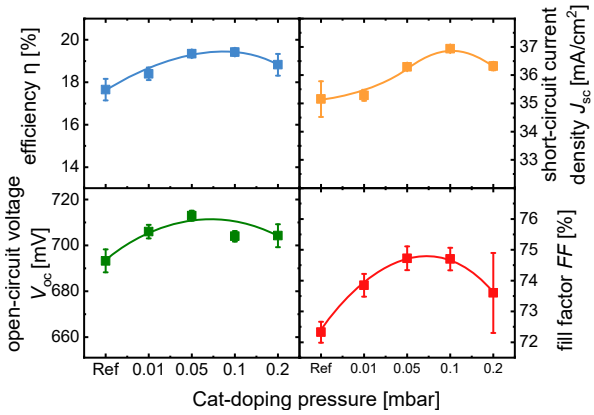

Figure 6.6: *Results of cells with Cat-doping at different processing pressures on µc-Si:H(n) in SHJ solar cells. A reference cell without Cat-doping was also included for comparison and Cat-doping processes were performed with pressures varying from 0.01 mbar to 0.2 mbar, the T_f is 1000 °C and T_{sub} is 200 °C for all Cat-doped cells*

As shown in Sec. 4.3, N_{P} after Cat-doping with different pressures shows a trend of first increase then decrease when pressure is too high. Consequently, the cell results also show the same trend. The η first increases from 17.7% to 19.4% when

the Cat-doping was applied and the pressure was increased from 0.01 mbar to 0.1 mbar; the η then decreases to 18.8% as further increase the pressure to 0.2 mbar. Both V_{oc} and FF show similar trend as well. The V_{oc} was improved from 693 mV of the reference cell to 713 mV of the cell with Cat-doping at 0.1 mbar, then V_{oc} was reduced to 704 mV of the cell with Cat-doping at 0.2 mbar. The FF also performs in the same way with variation from 72.3% to74.7% and then to 73.6%. All in all, all the V_{oc} and FF values from cells with Cat-doping are higher than that from the reference cell, showing Cat-doping's ability to improve the performance of the cells in different aspects. The improvement might be attributed to the three effects during Cat-doping, however, the similar tendency could be attributed to the change of N_{P} when different conditions were used in Cat-doping.

6.4 Cat-doping on nc-SiO$_x$:H(n)

It has been shown in Figure 6.2 that Cat-doping could be used to improve the performance of cells with different silicon alloy. As for nc-SiO$_x$:H(n) film, the film property varies as the r_{CO_2} change during deposition and a clear trade-off lays between the optical and electrical properties. To overcome the trade-off and obtain both good optical and electrical property, Cat-doping on nc-SiO$_x$:H(n) films was investigated in Sec 4.5. In this section, Cat-doping was applied on to nc-SiO$_x$:H(n) films in SHJ solar cells to test the ability to advance the cell performance. nc-SiO$_x$:H(n) film with r_{CO_2}=30% was chosen for the study for a balanced optical and electrical properties. If the r_{CO_2} is too low, the film will be very conductive and Cat-doping might only play a minor role. Meanwhile, for nc-SiO$_x$:H(n) with too low r_{CO_2} the transparency will be sacrificed and the point of using nc-SiO$_x$:H in cells is gone. On the other hand, the conductivity of nc-SiO$_x$:H with too high r_{CO_2} will be too low even after Cat-doping, thus results in low FF. Therefore, r_{CO_2}=30% was chosen here to be used in SHJ solar cells.

The cell results are shown in Figure 6.7. Different from the improvement shown before where Cat-doping was done on μc-Si:H(n) in the cells, here the Cat-doping doesn't seem to have significant influence on the cell performance although T_{f} was

varied from 900 °C to 1800 °C. The J_{sc} seems to increase slightly as T_f increases, which is possibly due to the slightly etching of the nc-SiO_x:H(n) layers in the front of the cells. However, the etching could also be the reason for the slightly decrease of V_{oc} as it might create more defects. Meanwhile, the most expected improvement in FF is not shown in the cell results. In Sec. 4.5, it has been shown that the conductivity of nc-SiO_x:H films can be increased slightly by Cat-doping. However, the increase in the conductivity doesn't shown in the improvement of FF. Here the most possible reason could be that the increase in δ is too small to cause improvement in FF. Therefore, if Cat-doping is aimed to be used on nc-SiO_x:H films in cells to improve the performance, more study should be carried out and more intense Cat-doping conditions might be explored.

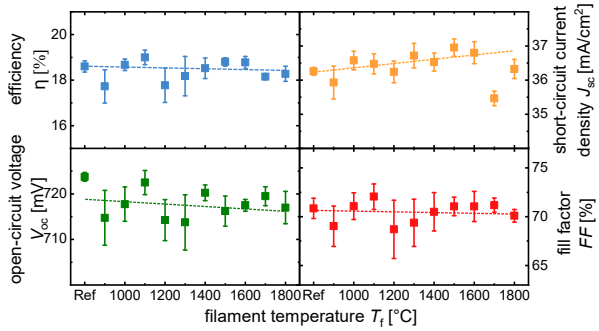

Figure 6.7: *Results of cells with Cat-doping at different processing pressures on nc-SiO_x:H(n) in SHJ solar cells. A reference cell without Cat-doping was also included for comparison and Cat-doping processes were performed with T_f varying from 900 °C to 1800 °C, the T_{sub} is 200 °C and pressure is 0.01 mabr for all Cat-doped cells*

6.5 Cat-doping on a-Si:H(i)

Until now, different silicon alloys with unique optical and electrical properties have been studied in SHJ solar cells with Cat-doping applied onto the n layers in the front. Improvement to different extends in cell performance has also shown the effectiveness of Cat-doping upon advancing the cell performance. However, despite the prior optical property of nc-SiO_x:H and electrical property of μc-Si:H, the use of

these two materials still leads to additional parasitic absorption in the front. Therefore, a new concept of eliminating the deposition of n layer in the front was proposed here to avoid the parasitic absorption. The structure of conventional SHJ solar cells is illustrated in Figure 6.1, where in the front is a-Si:H(i)\a-Si:H(n)\ITO\$Ag\ grids$ stack. To eliminate the parasitic absorption from the n layer, Cat-doping was applied directly on the a-Si:H(i) layer to form a doped a-Si:H layer which could act as a n layer. In this way, the thickness of the front n layer is reduced, which reduces the parasitic absorption in the front. Therefore, the front side is a stack of a-Si:H(i) + Cat-doping\a-Si:H(n)\ITO\$Ag\ grids$. However, the passivation quality of such stacks with Cat-doping applied directly on the thin a-Si:H(i) layer needs to be tested before the use in device.

6.5.1 Passivation enhancement

The effect of Cat-doping on passivation quality has already been discussed in Chap. 5 and the results there show that Cat-doping could effectively improve the passivation quality of different passivated samples. As for passivated samples with a-Si:H(i) discussed in Sec. 5.2.5, at that time the passivation was not deteriorated by Cat-doping and seemed to be limited by other aspects, such as cleaning condition, wafer quality and a-Si:H(i) layer quality. With the development of SHJ solar cells in the lab, better passivation and better cell performance were achieved. Therefore, here Cat-doping on a-Si:H(i) in better passivated samples was studied again to investigate the validation of Cat-doping on different passivated samples. The structure of the passivated samples and their τ_{eff} are shown in Figure 6.8 (a) and (b), respectively.

For the first sample, P Cat-doping was done on the front side and here Cat-doping with T_{f} of 2200 °C, T_{sub} of 200 °C and pressure of 0.01 mbar was chosen for its largest increase in N_{P}. For the second sample, 8 nm a-Si:H(n) was deposited on the front side for comparison. The relation between minority carrier lifetime vs excess carrier density together with iV_{oc} of these two samples were shown in Figure 6.8(b). For the sample with a-Si:H(n) layer, the iV_{oc} stays almost unchanged around 729 mV. The iV_{oc} for the sample with Cat-doping increases from 732 mV to 741 mV indicating

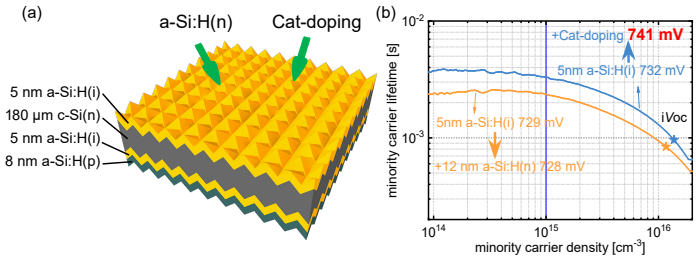

Figure 6.8: *Sketch of passivated samples with two post treatment in (a): one is Cat-doping on the a-Si:H(i) layer and the other one is deposition of a-Si:H(n) layer; (b) shows the τ_{eff} of the passivated samples with two post treatments.*

improved passivation quality.

As discussed in Sec. 5.1, the co-existence of thermal annealing, hydrogenation and P doping effects during the Cat-doping process could lead to the improvement in passivation quality [91]. The thermal annealing effect and hydrogenation effect during the process both help to saturate the dangling bonds, therefore improve the passivation in the stack [124]. Meanwhile, P doping may create a shallow highly doped layer at the surface and acts as FSF, which could also improve the passivation. All these three effects together lead to the improvement of passivation quality of the stack.

6.5.2 Cat-doping on a-Si:H(i) in SHJ cells

The passivation quality has been proven to be improved by Cat-doping on a-Si:H(i) layer in the former section. However, the n layer in the front has contact with the ITO layer which provide good ohmic contact between the layers in a cell. It could be that the Cat-doped a-Si:H layer is not conductive enough and the band diagram alignment is not good enough to provide good ohmic contact. Therefore, a modified conventional SHJ cell structure is also tested. In this modified structure, the front is a stack of a-Si:H(i) + Cat-doping\a-Si:H(n)\ITO\$Ag\ grids$. Accordingly, the aim of this structure is not to reduce the parasitic absorption but to further improve the FF. Two structures are illustrated in Figure 6.9.

These two structures both involve the Cat-doping on a-Si:H(i) layers, so they are put together for comparison. Meanwhile, one reference cell without Cat-doping for each structure is included. For simplicity, the reference for cell without n layer deposition is hereafter referred to as *C0*, cell without n layer but with Cat-doping (structure(a) in Figure 6.9) is hereafter referred to as *C1*, reference for conventional SHJ cell (cell with n layer) is hereafter referred to as *C2* and conventional cell with Cat-doping (structure (b) in Figure 6.9) is hereafter referred to as *C3*. In this series, only T_f was varied among other Cat-doping conditions because it provides the largest change in N_P and doping depth inside the film. Thus, different thicknesses of a-Si:H(i) were also used. Since different thicknesses of a-Si:H(i) were also used in these cells, suffix is used to distinguish the difference, such as *C0-5* means a reference cell with 5 nm a-Si:H(i) in the front and *C3-15* means a conventional cell with Cat-doping applied on the 15 nm a-Si:H(i) in the front side.

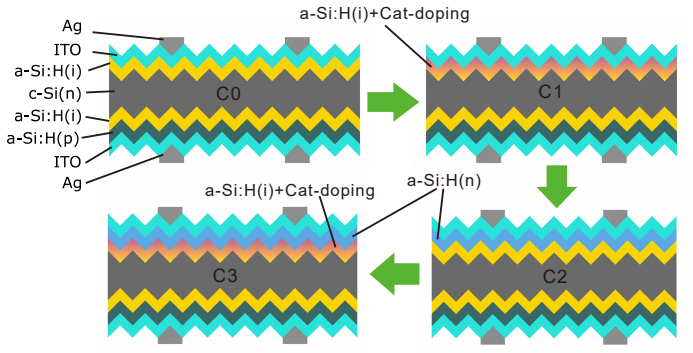

Figure 6.9: *Sketches of SHJ solar cells with four different structures. From C0 to C1, Cat-doping treatment was added to the a-Si:H(i) layer in the front; C2 has a conventional SHJ structure, and from C2 to C3, Cat-doping was also added to the a-Si:H(i) layer in the front.*

The cell results are shown in Figure 6.10. First of all, for *C0* cell, the η is very poor below 9%. When Cat-doping was applied to the a-Si:H(i) layer on the front, the η increases. With higher T_f during Cat-doping, the η becomes higher. For *C1* cell, when the T_f reaches 2200 °C, the η is the highest, which is 19.4%. The value

is as good as the conventional SHJ cells (*C2*), which have a-Si:H(n) layers. The J_{sc} of the cell without a-Si:H(n) layer (*C0* and *C1*) is around 39.0 mA/cm^2, higher than the 38.0 mA/cm^2 from cells with a-Si:H(n) layer (*C2* and *C3*) and this higher J_{sc} is independent from whether use Cat-doping or not. For *C1* cell, both V_{oc} and FF increase when the Cat-doping was used and reached their highest value at T_f of 2200 °C. Furthermore, Cat-doping was also done on the front a-Si:H(i) layer in *C3*. It turns out the *C3* cell have the highest η and the champion η is 21.2% while the conventional *C2* cell has 19.7% efficiency. The increase in η mainly comes from the improvement in FF, which increases from 73.2% to 78.1%.

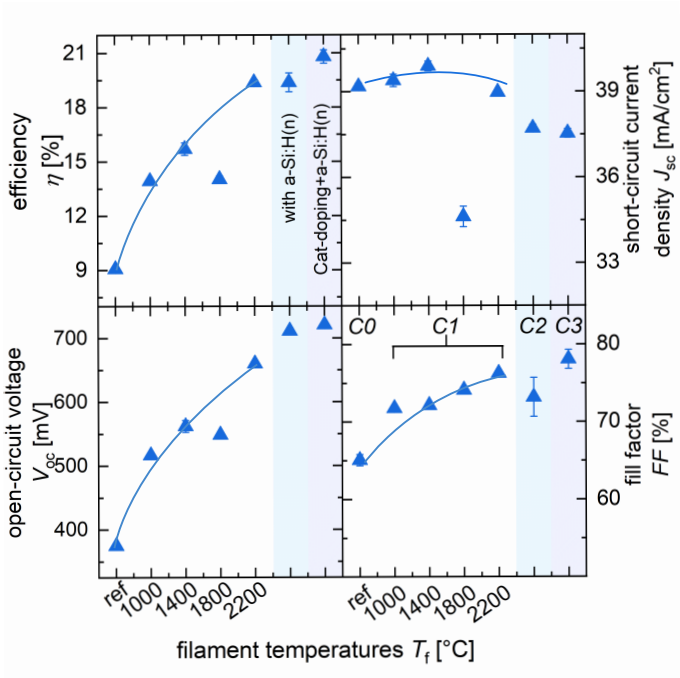

Figure 6.10: *Results of cells with different front side structures, referred to as C0, C1, C2, C3. The reference cells (C0) are with only a-Si:H(i) layers in the front; conventional cells (C2) are indicated in green strips and conventional cells with additional Cat-doping (C3) are indicated in light purple strips. C1 cells without a-Si:H(n) on top of a-Si:H(i) are with Cat-doping under different filament temperatures in the range of 1000 to 2200 ° C.*

Comparing *C0* and *C1* cells, the possible reason for η to increase as T_f increases is that when Cat-doping is applied, three effects, i.e. thermal annealing, hydrogenation and P doping, happen to the samples. Thermal annealing and hydrogenation improve the V_{oc} due to chemical passivation. P doping, which is likely to provide more P dopants, improves both the V_{oc} and FF by FSF effect and doping of a-Si:H(i), respectively. These three effects become more significant with higher T_f. Therefore, at T_f up to 2200 °C, the cell efficiency of *C1* reaches 19.4%, a value which is equivalent to a conventional cell *C2*. The V_{oc} is 660 mV and FF is 76.3% for cell *C1* with Cat-doping at T_f of 2200 °C and as comparison, the V_{oc} is 711 mV and FF is 73.2% for cell *C2*. Compared to *C2*, the lower V_{oc} of cell *C1* at T_f of 2200 °C may come from the damage during the ITO sputtering since there is only a 5 nm a-Si:H(i) between the c-Si surface and high kinetic energy plasma. Meanwhile, the higher FF of cell *C1* is the result of higher conductivity from Cat-doped a-Si:H(i).

Compared to *C2* cells, *C3* cells which have a-Si:H(n) layers and additional Cat-doping on a-Si:H(i) layer still have the highest efficiency despite of the lower J_{sc}. Actually, the highest efficiency of 21.2% is from *C3* where Cat-doping was used comparing to the 19.7% of *C2* without Cat-doping. The difference in η mainly comes from the FF, which increases from 73.2% of *C2* to 78.1% of the champion cell *C3*. Compared to *C2* cell, *C3* cell has lower J_{sc} and same V_{oc}, but the FF is higher. The possible reason for higher FF is that the conductivity of the a-Si:H(i) layer has been increased by applying Cat-doping. Meanwhile, compared *C3* to *C1* FF from *C3* is also higher. Here the reason is likely that only using Cat-doping on a-Si:H(i) layer may not achieve same high level of doping as compared to in-situ doped a-Si:H(n) layer, therefore the band gap alignment between the Cat-doped a-Si:H(i) layer and ITO is not as good as the one between in-situ a-Si:H(n) and ITO. The aforementioned two reasons imply that currently the a-Si:H(n) is still necessary but Cat-doping on the a-Si:H(i) layer might further improve the FF.

6.5.3 Effect on light absorption

For a closer look at the increase in J_{sc}, internal quantum efficiency (IQE) measurements were done for the *C2-10* cells and *C1-10* cells (with T_f of 2200 °C), as

shown in Figure 6.11(a). Here 10 nm a-Si:H(i) in the front, instead of 5 nm used in cells, was used for a more obvious change in front side light absorption. IQE of *C1-10* cells with different T_{f} was also measured in Figure 6.11(b). The IQE spectrum in Figure 6.11(a) clearly shows that for the cell without a-Si:H(n), there is a significant absorption increase in the short wavelength range, resulting in about 1 mA/cm^2 increase in J_{sc}. However, when Cat-doping was applied with different T_{f}, there is slightly decrease of light absorption in the short wavelength range and it reduces the J_{sc} 0.5 mA/cm^2 by raising T_{f} from 1000 °C to 2200 °C. At higher T_{f}, defects from atomic H etching may become severer [12] and P doping becomes more significant, this could give rise to the number of recombination center. Therefore, the slight decrease in J_{sc} could come from the increased recombination of Cat-doped a-Si:H film in the front. The clear large improvement of light absorption in the short wavelength range for *C1-10* where there is no a-Si:H(n) layer deposited. This confirms that by replacing a-Si:H(n) with Cat-doping on a-Si:H(i), the parasitic absorption could be reduced in the front side and an increase in J_{sc} about 1 mA/cm^2 has been achieved.

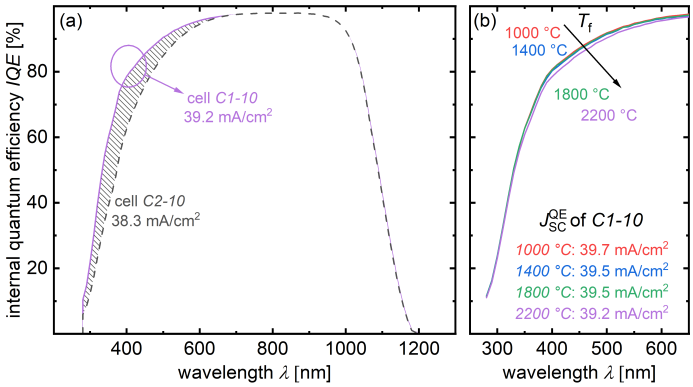

Figure 6.11: *IQE of the 10 nm a-Si:H(i) cell series: (a) IQE of C1-10 cell with Cat-doping at T_f of 2200 °C and C2-10 cell with a-Si:H(n) layer; (b) IQE of C1-10 cells with Cat-doping at different T_f and their corresponding J_{sc} from IQE.*

7 Summary and outlook

The urgency to find green and renewable energy to replace existing fossil fuels has promoted intensive studies in various researches in climate and energy fields. Converting sunlight with unlimited lifespan to electricity, photovoltaic technology has found its way to take over a large portion in the sustainable energy market. However, the challenge still lays in lowering the levelized cost of electricity (LCOE) of PV, which is yet not competitive enough compared to fossil energy. SHJ solar cells has the advantages in high efficiency, simple production procedure and low cost. Conventional SHJ solar cells use a-Si:H(i) layers on both sides to passivate the wafer and a-Si:H(n/p) layers as surface field layer or emitter layer. However, the use of doped a-Si:H layers in the front leads to parasitic absorption that reduces the J_{sc} of cells. Furthermore, to ensure good passivation certain thickness of a-Si:H(i) layer is necessary which is against good electrical transport in the cells. To solve problem mentioned above, new window layer materials, such as nc-SiO_x:H and μc-SiC:H, have been widely studied for better light absorption. Materials with better electrical property, such as μc-Si:H, have also been tested. The passivation layer is also explored in terms of both optimization of existing a-Si:H(i) layer and introducing new passivation layers [83]. Beside these new material research, another promising technique is to introduce Cat-doping process that further enhance the electrical property of aforementioned silicon alloys and improve the passivation.

Accordingly, the goals of this thesis were to: (1) understand the mechanism of Cat-doping on different silicon alloys and the effects on both electrical and optical properties of silicon alloys; (2) understand how the passivation quality was affected when Cat-doping was applied onto silicon alloy layers inside cell precursors; (3) explore the efficiency improvement from Cat-doping on silicon alloys in SHJ solar cells.

In this chapter, a summary of the main results and conclusion of this thesis is given. Moreover, an outlook for further investigating Cat-doping on silicon alloys in terms of both mechanism and implementation in device is provided.

7.1 Summary

Short summary for each section is listed below including Cat-doping on various silicon alloys, effect on passivation and advancement in device performance.

Cat-doping on silicon alloys

Electrical property and doping profile Cat-doping on different silicon alloy films proved Cat-doping's ability to further improve the conductivity of these films and N_P increase shown in P profiles from SIMS confirmed that P atoms were incorporated into the films. The number of P atoms incorporated into the films were influenced by the Cat-doping conditions (i.e. T_f, T_{sub} and processing pressure) and N_P can reach the range of $10^{21} cm^{-3}$. The increase in conductivity from μc-Si:H implies its independence of χ_c when Cat-doping was used. However, the doping depth and N_P from Cat-doping is largely dependent on the microstructure and composition of the silicon alloy films. As for a-Si:H and μc-Si:H films, the loose microstructure might enable P atoms to penetrate more and deeper inside the films, if compared to Cat-doping on c-Si. This results in higher N_P and larger doping depth in a-Si:H and μc-Si:H. It becomes more interesting when Cat-doping was applied on nc-SiO_x:H films. The P atoms penetrate throughout the whole thickness of nc-SiO_x:H films via the porous cage microstructure of nc-SiO_x:H. This porous microstructure may offer channel for P atoms to penetrate deep inside the film. However, the incorporated P atoms are not all activated as dopants. Actually, the activation ratio of Cat-doping incorporated P atoms seems to decrease with increase of O content inside the film. Therefore, Cat-doping on nc-SiO_x:H only improve the conductivity slightly. When it comes to μc-SiC:H films, P atoms from Cat-doping likely only attach to the surface of μc-SiC:H films, which has a very dense microstructure and has merely any channel for P atoms to penetrate.

Structural and Optical properties The microstructure of silicon alloys doesn't change after Cat-doping process, though defects and etching might happen through the process depending on the Cat-doping conditions used. Furthermore, no significant optical property change has been seen with PDS measurement. However, slightly increase in light absorption in the low energy range is seen and the influence in devices was investigated later.

Enhancement in passivation quality

Three effects during Cat-doping Using different gases during Cat-doping, coexistence of three effects, i.e. thermal annealing, hydrogenation and P doping, was confirmed. However, the portion of the three effects in the enhancement in passivation quality remains difficult to derive. The thermal annealing and hydrogenation exist in Cat-doping process independent from the materials used, but P doping could rely heavily on the microstructure of silicon alloys. Therefore, passivated samples with silicon alloys with higher ΔN_{P} results in larger improvement in τ_{eff}. This is likely due to the fact that P doping effect enhances the surface field effect and improves the τ_{eff}.

Passivated stacks with silicon alloys The τ_{eff} of passivated stacks with different silicon alloys was improved differently after Cat-doping. In general, with larger change in σ after Cat-doping the τ_{eff} improvement is more significant. The Cat-doping conditions play a big role upon improving the passivation quality and balance between aforementioned three effects and H etching exists. In detail, the τ_{eff} for samples with μc-Si:H film has the most significant enhancement after Cat-doping, which co-relates to its large increase in σ. Meanwhile, the τ_{eff} for samples with nc-SiO_x:H and μc-SiC:H has no significant change due to the minor in σ. However, the difference between nc-SiO_x:H and μc-SiC:H is the P atoms were incorporated into nc-SiO_x:H but the activation ratio is low while P atoms were barely incorporated into μc-SiC:H films. Similar as μc-Si:H, the P profile for a-Si:H films shows that P atoms were successfully incorporated but the τ_{eff} didn't improve much. The reason might be that the τ_{eff} was limited by other aspects.

Cat-doping in SHJ solar cells

Three silicon alloys were tested in SHJ solar cells for their prior optical or electrical properties. Beside the new materials, Cat-doping as a new method was also studied for the use in SHJ solar cells. In general, the goal to implement Cat-doping in SHJ solar cells is to achieve better electrical property of the film while not jeopardize the optical property. With the three effects from Cat-doping upon τ_{eff}, the device could reach higher V_{oc} and FF, therefore improved η. Meanwhile, with Cat-doping's ability to dope the intrinsic materials, new approaches of making SHJ solar cells with less procedure or higher η were proposed and tested. In the following, the main conclusion involving devices is summarized.

Cat-doping on different silicon alloys Firstly, a scan of Cat-doping on different n-type silicon alloys in SHJ solar cells shows improved η from Cat-doping and the improvement comes mainly from improved V_{oc} and FF, which is the goal of this work. Slightly decrease in J_{sc} was also seen, as an result of increased free carrier absorption in short wavelength range.

Cat-doping on μc-Si:H(n) Cells with μc-Si:H(n) in the front were studied in detail via varying the Cat-doping conditions. The performance of cells were improved upon the application of Cat-doping and the processing condition (i.e. T_{f}, T_{sub} and processing pressure) have a significant impact on the performance improvement and local optimal conditions were identified. The cell results also agrees very well with the change in material properties.

Cat-doping on nc-SiO$_x$:H(n) Although Cat-doping with T_{f} in a large range has been tried on nc-SiO$_x$:H(n) inSHJ solar cells, the impact of Cat-doping on the η is very small. The cell performance doesn't seem to change much with Cat-doping. In another sense, this also agrees with the tiny change in conductivity of nc-SiO$_x$:H(n) after Cat-doping.

Cat-doping on a-Si:H(i) The goal of applying Cat-doping on a-Si:H(i) in cells was to eliminate the parasitic absorption from the front side n layers as well as

improve the FF. This results in two approaches with Cat-doping on a-Si:H(i) layers: one is without deposition of a-Si:H(n) and one is with a-Si:H(n) like that in conventional SHJ solar cells. In both approaches, Cat-doping was done on the a-Si:H(i) passivation layer. The one without a-Si:H(n) layer shows advantage in reducing parasitic absorption in the front of the cells and the other one with additional Cat-doping on a-Si:H(i) layer shows improvement in FF and results in the champion cell efficiency of 21.2%. Meanwhile, applying Cat-doping on the a-Si:H(i) layer in passivated samples also shows improvement in iV_{oc} with a value of 741 mV. There is slightly increase in free carrier absorption in the front of cells likely due to Cat-doping on a-Si:H(i) layer. However, compared to the gain of 1 mA/cm^2 in J_{sc} via using no a-Si:H(n) layer, it is worth to applying Cat-doping in such SHJ solar cells.

7.2 Outlook

Based on the results in this work, the directions of further developing Cat-doping in terms of mechanism, materials and devices are presented in the following.

Cat-doping mechanism

Several hypotheses of Cat-doping mechanism have been proposed by Matsumura et al. [87] together with some experiment and simulation results on a-Si:H and c-Si. This work extends the Cat-doping materials to various silicon alloys, i.e. μc-Si:H, nc-SiO_x:H and μc-SiC:H, as well as more study in a-Si:H. However, these studies support the hypotheses in an indirect way and no directly proof has been shown. To get deeper insight into what happen in a Cat-doping process, the following directions are recommended:

I **Defects and vacancy** Defects and vacancy seem to play a big role for the happening of Cat-doping. The H radicals produced from the hot filament may etch the silicon film but could also create defects and vacancy for P atoms to penetrate inside. Therefore, characterizing the defect states and vacancy might reveal the relation between Cat-doping and them.

II **Surface modification** Surface modification is one of the hypotheses that could explain the limited thickness of Cat-doping. If one can find a way to characterize the surface structure within a few nanometer, the limited thickness of Cat-doping might be understood.

III **Hydrogen** Hydrogen plays a big role during Cat-doping. Both SIMS profiles and simulation show that H is involved in the process and might help P atoms to penetrate. Therefore, if one can use isotopic H and P atoms to locate the H and P atoms from Cat-doping and their relative distribution, the role the H might be understood.

IV **Microstructure** Comparing among silicon alloys, clearly the microstructure is an important issue that determines N_P and doping depth from Cat-doping. Methods such as APT combined with other microstructure characterization methods may disclose where the P atoms are located in the microstructure, therefore, reveal the penetration channel for P atoms or preferred channel.

Cat-doping on silicon alloys

High N_P in a-Si:H and μc-Si:H has already been achieved with Cat-doping by varying Cat-doping conditions. However, for nc-SiO_x:H and μc-SiC:H, due to their composition and microstructure the increase in N_P and N_c is still very limited. Based on existing results, one direction is to go to extremer Cat-doping conditions, such as higher T_f and pressure to push more P atom into the films. The activation of the Cat-doping incorporated P atoms is another problem, which is likely related to the intrinsic properties of silicon alloys.

Passivation enhancement

It is clear that three effects co-exist in the Cat-doping process and help to improve the effective lifetime. However, it should be noted that as the Cat-doping conditions changes, other effects, such as H etching, may also come into play and compensate the improvement. Therefore, more detailed study of Cat-doping conditions may give even higher improvement in τ_{eff}. Another aspect is to produce more low energy H

radicals that won't etch the film and deteriorate the passivation quality.

Cat-doping in SHJ cells

The cell results show Cat-doping's ability to improve the efficiency. However, the reference cells used in this work initially don't have state-of-art η. The question remains that whether Cat-doping can further improve the η of already excellent cells. Therefore, Cat-doping should be validated in state-of-art SHJ solar cells.

For all SHJ solar cells with a-Si:H(i) passivation layers, the Cat-doping might be applied on several interfaces to maximize the improvement. In general, three interfaces are interesting for Cat-doping: a-Si:H(i)/c-Si, n layer/a-Si:H(i) and ITO/n layer. Applying Cat-doping on a-Si:H(i)/c-Si interface improves the passivation quality; on n layer/a-Si:H(i) interface improves both passivation quality and conductivity of a-Si:H(i); on ITO/n layer interface improves the conductivity of n layer. All together the V_{oc} and FF can be improved the most.

8 Abbreviations and Symbols

Variables and physical constants

α	optical absorption coefficient
$\alpha_{\mathbf{1\,eV}}$	sub-bandgap absorption at the photon energy of 1.0 eV
$\Delta E_{\mathbf{c}}$	conduction band offset
$\Delta E_{\mathbf{v}}$	valence band offset
Δn	excess carrier density
η	solar cell efficiency
λ	wavelength
μ	charge carrier mobility
ν	wavenumber
$\rho_{\mathbf{c}}$	contact resistivity
$\rho_{\mathbf{SiC}}$	resistivity of μc-SiC:H(n) film
σ	lateral electrical conductivity
$\tau_{\mathbf{eff}}$	effective carrier lifetime
A	absorptance
$c_{\mathbf{MMS}}$	monomethylsilane concentration
$d_{\mathbf{f\text{-}s}}$	distance between filament and substrate
E_{04}	optical bandgap
E_{μ}	activation energy of charge carrier mobility
$E_{\mathbf{A}}$	activation energy
$E_{\mathbf{B}}$	effective potential barrier height
$E_{\mathbf{C}}$	conduction band edge
$E_{\mathbf{F}}$	Fermi level
$E_{\mathbf{g}}$	bandgap energy
$E_{\mathbf{n}}$	activation energy of charge carrier density

EQE	external quantum efficiency
$E_{\mathbf{V}}$	valence band edge
$f_{\mathbf{CO2}}$	gas ratio of carbon dioxide
$F_{\mathbf{CO2}}$	flow rate carbon dioxide gas
FF	fill factor
$F_{\mathbf{H}}$	flow rate of hydrogen gas
$F_{\mathbf{MMS}}$	flow rate of monomethylsilane gas
$F_{\mathbf{N2}}$	flow rate of nitrogen gas
$\mathbf{h}$	Planck's constant
IQE	internal quantum efficiency
$I_{\mathbf{c}}$	crystallinity of silicon phase measured by Raman spectroscopy
$I_{\mathbf{sc}}$	short circuit current density
$I_{\mathbf{Si\text{-}C}}$	intensity of Si-C mode in FTIR spectroscopy
$\mathbf{i}FF$	implied fill factor
$\mathbf{i}V_{\mathbf{oc}}$	implied open circuit voltage
J	electrical current density
$J_{\mathbf{0}}$	saturation current density
$J_{\mathbf{R}}$	reflection loss in form of current density
$J_{\mathbf{ph}}$	photo-current density
$J_{\mathbf{sc}}$	short circuit current density
k	extinction coefficient or imaginary part of complex refractive index from ellipsometer
$\mathbf{k_B}$	Boltzmann constant ($\approx 8.6 \cdot 10^{-5}$ eV)
L	hypothetical cubic grain size
$L_{\mathbf{SiC}}$	average 3C-SiC grain size
$m_{\mathbf{e}}$	tunneling mass of electrons
$m_{\mathbf{h}}$	tunneling mass of holes
n	infractive index (real part)
$N_{\mathbf{A}}$	acceptor doping concentration
$n_{\mathbf{i}}$	intrinsic charge carrier concentration
$n_{\mathbf{j}}$	refractive index of material j
$N_{\mathbf{c}}$	charge carrier density
$N_{\mathbf{c,\ ave}}$	average charge carrier density in the film

$N_{\mathbf{P,\ ave}}$	average P concentration in the film
$r_{\mathbf{a,\ ave}}$	average activation ratio in the film
$N_{\mathbf{P}}$	phosphorus concentration
p	deposition pressure
$P_{\mathbf{f}}$	forward power
$P_{\mathbf{max}}$	maximum generated power
$P_{\mathbf{sun}}$	sun power
$\mathbf{q}$	elementary charge
QE	quantum efficiency
$r_{\mathbf{depo}}$	deposition rate
R	reflectance
r_{CO_2}	carben dioxide ratio in gas mixture
χ_c	Raman crystallinity
$R_{\mathbf{s}}$	series resistance
RSF	relatvie sensitivity factor
$R_{\mathbf{sh}}$	shunt resistance
S	thermopower
SRV	surface recombination velocity
T	temperature
$t_{\mathbf{anneal}}$	accumulated annealing time
$t_{\mathbf{acc}}$	accumulated deposition time of several depositions
$t_{\mathbf{depo}}$	deposition time
$T_{\mathbf{f}}$	filament temperature
$T_{\mathbf{sub}}$	heater temperature
V	voltage potential
$V_{\mathbf{oc}}$	open circuit voltage
$V_{\mathbf{s}}$	volume of surface layer of c-SiC grain
X	carbon fraction of μc-$Si_{1-X}C_X$:H

Material and elements

:H	hydrogenated
μc-	microcrystalline
a-	amorphous

Al	aluminum
Ag	silver
Ar	argon
B	boron
$\mathbf{B_2H_6}$	diborane
c-Si	crystalline silicon
C	carbon
H	hydrogen
N	nitrogen
O	Oxygen
$C_{\mathbf{O}}$	oxygen concentration
$\mathbf{CO_2}$	carbon dioxide
$\mathbf{H_2}$	molecular hydrogen
$\mathbf{H_2O}$	water
He	helium
$\mathbf{HNO_3}$	nitric acid solution
IPA	isopropyl alcohol
$\mathbf{H_3SiCH_3}$	monomethylsilane
(i)	intrinsic
(n)	n-type doped
$\mathbf{N_2}$	molecular nitrogen
$\mathbf{O_2}$	molecular oxygen
(p)	p-type doped
P	phosphorus
$\mathbf{PH_3}$	phosphine
Si	silicon
SiC	silicon carbide
SiH	mono-hydride
$\mathbf{SiH_2}$	dihydride
$\mathbf{SiH_4}$	silane
$\mathbf{SiN_x}$	sub-stoichiometric silicon nitride
$\mathbf{SiO_2}$	silicon dioxide
$\mathbf{a\text{-}SiO_x{:}H}$	amorphous silicon oxide

SiO_x	sub-stoichiometric silicon oxide
a-Si:H	hydrogenated amorphours silicon
μc-Si:H	hydrogenated microcrystalline silicon
nc-Si:H	hydrogenated nanocrystalline silicon
nc-SiO_x:H	hydrogenated nanocrystalline silicon oxide
μc-SiC:H	hydrogenated microcrystalline silicon carbide
Ta	tantalum
SnO_2	tin oxide
W	tungsten

Abbreviations

AC	alternating current
AM	air-mass
APT	atom probe tomography
ARC	anti-reflection coating
BSF	back surface field
FSF	front surface field
Cat-CVD	catalytic-chmical vapor deposition
Cat-doping	catalytic-doping
CVD	chemical vapor deposition
Cz	Czochralski
DB	dangling bond
eCV	electrochemical capacitance voltage
FCA	free carrier absorption
FTIR	Fourier transform infrared spectroscopy
Fz	float zone
HF	hydrofluoric acid (1% diluted)
HWCVD	hot wire chemical vapor deposition
IBC	interdigitated back contact
ITO	indium tin oxide
J-V	current density-voltage
IV	current-voltage
LCOE	levelised cost of electricity

MMS	monomethylsilane (CH_3SiH_3)
PDS	photothermal deflection spectroscopy
PECVD	plasma enhanced chemical vapor deposition
PERL	passivated emitter and rear locally diffused
PL	photoluminescence
PV	photovoltaics
PVD	physical vapor deposition
QSSPC	quasi steady-state photo conductance
RCA	standard cleaning process developed at Radio Corporation of America
RT	room temperature
SEM	scanning electron microscopy
SHJ	silicon heterojunction
SHJ solar cells	silicon heterojunction solar cells
SIMS	secondary ion mass spectrometry
SRH	Shockley-Read-Hall
SRIM	Stopping and Range of Ions in Matter
TCO	transparent conducting oxide
TEM	transmission electron microscopy
TLM	transfer length method
TOPCon	tunnel oxide passivated contact
VHF	very high frequency
XRD	X-Ray diffraction

9 List of publications

1 **Y. Liu**, DY. Kim, A. Lambertz and K. Ding, *Post-deposition Catalytic-doping of Microcrystalline Silicon Thin Layer for Application in Silicon Heterojunction Solar Cell*, Thin Solid Films 635 (2017) 63-65

2 **Y. Liu**, M. Pomaska, W. Duan, DY. Kim, M. Köhler, U. Breuer and K. Ding, *Phosphorous Catalytic-Doping of Silicon Alloys for the Use in Silicon Heterojunction Solar Cells*, Advanced Engineering Materials, 2019, 1900613

3 **Y. Liu**, M. Pomaska, W. Duan, D. Qiu, S. Li, A. Lambertz, A. Gad, U. Breuer, F. Finger, U. Rau and K. Ding, *Phosphorus Catalytic doping on Intrinsic Silicon Thin Films for the Application in Silicon Heterojunction Solar Cells*, ACS Applied Materials & Interfaces, 2020, 12, 50, 56615–56621

4 **Y. Liu**, W. Duan, M. Pomaska, A. Lambertz, D. Qiu, I. Povstugar, F. Finger, U. Rau and K. Ding, *Catalytic-doping of Hydrogenated Nanocrystalline Silicon Oxide Thin-films and the Application in Silicon Heterojunction Solar cells*, in preparation for submission

5 D. Qiu, W. Duan, A. Lambertz, K. Bittkau, **Y. Liu**, A. Gad, M. Pomaska, U. Rau and K. Ding, *Front Contact Optimization for Rear-emitter SHJ Solar Cells with Ultra-thin n-type Nanocrystalline Silicon Oxide*, Solar Energy Materials and Solar Cells, 209 (2020) 110471

6 DY. Kim, F. Lentz, **Y. Liu**, A. Singh, A. Richter, M. Pomaska, A. Lambertz and K. Ding, *Selective Dry Etching of p-Type Si Films for Photolithography Processing of Interdigitated Back Contact Silicon Heterojunction Solar Cells*, IEEE Journal of Photovoltaics, vol. 7, no. 5, pp. 1292-1297, Sept. 2017

10 Curriculum Vitae

Personal details

Name	Yong Liu
Date of birth	January 22nd, 1990
Place of birth	Sichuan, China
Citizenship	Chinese

Education

1996-2002	Guanming Central Primary School, Santai, Sichuan, China
2002-2005	Santai English Experimental School, Santai, Sichuan, China
2005-2008	Santai Middle School, Santai, Sichuan, China
2008-2012	University of Science and Technology Beijing, Beijing, China
	School of Mathematics and Physics
	Bachelor in Applied Physics
2012-2015	University of Chinese Academy of Science
	College of Material Science and Opto-Electronic Technology
	Master in Condensed Matters
2015-2019	PhD thesis at the Forschungszentrum Jülich GmbH,
	IEK5-Photovoltaics

References

[1] IRENA, Renewable capacity statistics 2019, Technical report, International Renewable Energy Agency (IRENA), Abu Dhabi, 2020.

[2] International Renewable Energy Agency, Global Renewables Outlook: Energy transformation 2050, Technical report, International Renewable Energy Agency, Abu Dhabi, 2020.

[3] S. De Wolf, A. Descoeudres, Z. C. Holman, and C. Ballif, Green **2**, 7 (2012).

[4] K. Masuko et al., IEEE Journal of Photovoltaics **4**, 1433 (2014).

[5] M. Taguchi et al., IEEE Journal of Photovoltaics **4**, 96 (2014).

[6] C. Battaglia et al., Nano Letters **14**, 967 (2014).

[7] B. Legradic et al., High efficiency Si-heterojunction technology - it's ready for mass production, in *2015 IEEE 42nd Photovoltaic Specialist Conference (PVSC)*, pages 1–3, 2015.

[8] Z. C. Holman et al., IEEE Journal of Photovoltaics **2**, 7 (2012).

[9] M. W. M. van Cleef et al., Journal of Applied Physics **82**, 6089 (1997).

[10] A. Richter et al., Solar Energy Materials and Solar Cells **174**, 196 (2018).

[11] M. Pomaska et al., Japanese Journal of Applied Physics **56**, 22302 (2017).

[12] H. Matsumura et al., Journal of Applied Physics **116**, 114502 (2014).

[13] J. Seto, K. Ohdaira, and H. Matsumura, Japanese Journal of Applied Physics **55**, 04ES05 (2016).

[14] M. Pomaska, W. Beyer, E. Neumann, F. Finger, and K. Ding, Thin Solid Films (2015).

[15] K. Ohdaira, J. Seto, and H. Matsumura, Japanese Journal of Applied Physics **56**, 08MB06.

[16] S. Tsuzaki, K. Ohdaira, T. Oikawa, K. Koyama, and H. Matsumura, Japanese Journal of Applied Physics **54** (2015).

[17] J. Haschke, O. Dupré, M. Boccard, and C. Ballif, Solar Energy Materials and Solar Cells **187**, 140 (2018).

[18] C. Battaglia, A. Cuevas, and S. De Wolf, Energy & Environmental Science **9**, 1552 (2016).

[19] R. V. K. Chavali, S. D. Wolf, and M. A. Alam, Progress in Photovoltaics: Research and Applications **26**, 241 (2018).

[20] M. Yamaguchi et al., Journal of Materials Research , 1 (2017).

[21] K. Yoshikawa et al., Nature Energy **2**, 17032 (2017).

[22] A. Tomasi et al., Photovoltaics, IEEE Journal of **4**, 1046 (2014).

[23] F. Sahli et al., Nature Materials **17**, 820 (2018).

[24] J. Werner et al., ACS Energy Letters **3**, 2052 (2018).

[25] W. Fuhs, L. Korte, and M. Schmidt, Journal of Optoelectronics and Advanced Materials **8**, 1989 (2006).

[26] B. Paviet-Salomon et al., IEEE Journal of Photovoltaics **5**, 1293 (2015).

[27] H. Fujiwara and M. Kondo, Journal of Applied Physics **101**, 54516 (2007).

[28] N. Jensen, R. M. Hausner, R. B. Bergmann, J. H. Werner, and U. Rau, Progress in Photovoltaics: Research and Applications **10**, 1 (2002).

[29] R. Varache, A. Valla, N. Nguyen, and D. Muñoz, Energy Procedia **55**, 302 (2014).

[30] T. Koida, H. Fujiwara, and M. Kondo, Applied Physics Express **1**, 41501 (2008).

[31] K. Ding, U. Aeberhard, F. Finger, and U. Rau, Journal of Applied Physics **113** (2013).

[32] L. Mazzarella, A. B. Morales-Vilches, L. Korte, R. Schlatmann, and B. Stannowski, Solar Energy Materials and Solar Cells **179**, 386 (2018).

[33] L. Mazzarella et al., IEEE Journal of Photovoltaics **8**, 70 (2018).

[34] J. Bullock et al., Nature Energy , 15031 (2016).

[35] J. Yu et al., Solar Energy **159**, 704 (2018).

[36] W. Fuhs, K. Niemann, and J. Stuke, AIP Conference Proceedings **20**, 345 (1974).

[37] J. I. Pankove and M. L. Tarng, Applied Physics Letters **34**, 156 (1979).

[38] M. Taguchi, Improvement of the Conversion Efficiency of Polycrystalline Silicon Thin Film Solar Cell, in *proc. of Fifth PVSEC*, Florida, 1990.

[39] K. Wakisaka, M. Taguchi, and T. Sawada, Record of the Twenty-Second IEEE Photovoltaic Specialists Conference **2**, 887 (1991).

[40] NEDO, World's Highest Conversion Efficiency of 26.33% Achieved in a Crystalline Silicon Solar Cell -A World First in a Practical Cell Size-, 2016.

[41] A. Dussan, R. H. Buitrago, and R. R. Koropecki, Microelectronics Journal **39**, 1292 (2008).

[42] H. Sai, T. Matsui, H. Kumagai, and K. Matsubara, Applied Physics Express **11**, 22301 (2018).

[43] O. Vetterl et al., Solar Energy Materials and Solar Cells **62**, 97 (2000).

[44] M. W. M. van Cleef, J. K. Rath, F. A. Rubinelli, C. H. M. van der Werf, and R. E. I. Schropp, Microcrystalline-crystalline silicon heterojunction solar cells using highly conductive thin p-type microcrystalline silicon window layers, in *Conference Record of the Twenty Fifth IEEE Photovoltaic Specialists Conference - 1996*, pages 429–432, 1996.

[45] D. Muñoz et al., Journal of Non-Crystalline Solids **352**, 1953 (2006).

[46] Y. Xu et al., Journal of Non-Crystalline Solids **352**, 1972 (2006).

[47] O. Sergeev, A. Neumüller, I. Shutsko, M. Vehse, and C. Agert, Energy Procedia **124**, 371 (2017).

[48] T. Bronger and R. Carius, Thin Solid Films **515**, 7486 (2007).

[49] C. Droz et al., Solar Energy Materials and Solar Cells **81**, 61 (2004).

[50] H. Guo-Fu et al., Chinese Physics **16**, 553 (2007).

[51] M. Kondo, Y. Toyoshima, A. Matsuda, and K. Ikuta, Journal of Applied Physics **80**, 6061 (1996).

[52] A. Matsuda, Journal of Non-Crystalline Solids **338–340**, 1 (2004).

[53] H. Overhof, M. Otte, M. Schmidtke, U. Backhausen, and R. Carius, Journal of Non-Crystalline Solids **227-230**, 992 (1998).

[54] H. Stiebig et al., Solar Energy Materials and Solar Cells **48**, 351 (1997).

[55] F. Einsele, P. J. Rostan, M. B. Schubert, and U. Rau, Journal of Applied Physics **102**, 94507 (2007).

[56] O. Madani Ghahfarokhi, K. von Maydell, and C. Agert, Applied Physics Letters **104**, 113901 (2014).

[57] D. Gerlach et al., Applied Physics Letters **103**, 23903 (2013).

[58] J. Geissbühler et al., Applied Physics Letters **102**, 231604 (2013).

[59] S. Ghosh, A. De, S. Ray, and A. K. Barua, Journal of Applied Physics **71**, 5205 (1992).

[60] C. Jenq-Shiuh, S. Wen-Jyh, L. Si-Chen, C. T'ien-Chih, and W. Jon-Ching, Materials Chemistry and Physics **32**, 273 (1992).

[61] M. Tzolov, F. Finger, R. Carius, and P. Hapke, Journal of Applied Physics **81**, 7376 (1997).

[62] B. Strahm, A. A. Howling, L. Sansonnens, and C. Hollenstein, Plasma Sources Science and Technology **16**, 80 (2006).

[63] A. H. M. Smets, T. Matsui, and M. Kondo, Journal of Applied Physics **104**, 34508 (2008).

[64] N. Layadi, P. Roca i Cabarrocas, B. Drévillon, and I. Solomon, Physical Review B **52**, 5136 (1995).

[65] K. Ding et al., Journal of Non-Crystalline Solids **358**, 2145 (2012).

[66] K. Ding, U. Aeberhard, F. Finger, and U. Rau, Physica Status Solidi-Rapid Research Letters **6**, 193 (2012).

[67] K. Ding et al., Canadian Journal of Physics **92**, 758 (2014).

[68] K. Ding et al., Solar Energy Materials and Solar Cells **129**, 3 (2014).

[69] A. Richter, Z. Lei, F. Finger, and K. Ding, Microstructure model for nanocrystalline hydrogenated silicon oxide thin films in silicon heterojunction solar

cells, in *2015 IEEE 42nd Photovoltaic Specialist Conference (PVSC)*, pages 1–4, 2015.

[70] A. Richter, F. Lentz, M. Meier, F. Finger, and K. Ding, physica status solidi (a) **213**, 1976 (2016).

[71] A. Richter, L. Zhao, F. Finger, and K. Ding, Surface and Coatings Technology **295**, 119 (2016).

[72] A. Richter, *Nanocrystalline silicon oxide in silicon heterojunction solar cells*, Dissertation, RWTH Aachen University, Jülich, 2018.

[73] M. B. Pomaska, *Microcrystalline Silicon Carbide for Silicon Heterojunction Solar Cells*, PhD thesis, RWTH Aachen University, 2017.

[74] A. A. Lebedev, Semiconductors **33**, 107 (1999).

[75] S. Miyajima, A. Yamada, and M. Konagai, Japanese Journal of Applied Physics, Part 1: Regular Papers and Short Notes and Review Papers **46**, 1415 (2007).

[76] F. Finger et al., Thin Solid Films **517**, 3507 (2009).

[77] C. Sellmer, T. Bronger, W. Beyer, and R. Carius, Physica Status Solidi (C) Current Topics in Solid State Physics **7**, 670 (2010).

[78] O. Klutha et al., Thin Solid Films **351** (1999).

[79] J. Irikawa, S. Miyajima, T. Watahiki, and M. Konagai, Applied Physics Express **4** (2011).

[80] C. Banerjee et al., Japanese Journal of Applied Physics, Part 1: Regular Papers and Short Notes and Review Papers **46**, 1 (2007).

[81] S. Miyajima, J. Irikawa, A. Yamada, and M. Konagai, Applied Physics Letters **97** (2010).

[82] M. Pomaska, W. Beyer, E. Neumann, F. Finger, and K. Ding, Thin Solid Films (2015).

[83] M. Köhler et al., ACS Applied Materials & Interfaces **10**, 14259 (2018).

[84] M. Köhler et al., Development of a Transparent Passivated Contact as a Front Side Contact for Silicon Heterojunction Solar Cells, in *2018 IEEE 7th World Conference on Photovoltaic Energy Conversion (WCPEC) (A Joint*

Conference of 45th IEEE PVSC, 28th PVSEC & 34th EU PVSEC), pages 3468–3472, 2018.

[85] H. Taro et al., Japanese Journal of Applied Physics **50**, 121301 (2011).

[86] H. Taro, N. Yuki, K. Koichi, O. Keisuke, and M. Hideki, Japanese Journal of Applied Physics **51**, 61301 (2012).

[87] H. Matsumura, H. Umemoto, K. K. Gleason, and R. E. I. Schropp, *Catalytic Chemical Vapor Deposition: Technology and Applications of Cat-CVD*, Wiley, 2019.

[88] T. Ohta, K. Koyama, K. Ohdaira, and H. Matsumura, Thin Solid Films **575**, 92 (2015).

[89] H. Matsumura, M. Miyamoto, K. Koyama, and K. Ohdaira, Solar Energy Materials and Solar Cells **95**, 797 (2011).

[90] Y. Liu, D. Y. Kim, A. Lambertz, and K. Ding, Thin Solid Films **635**, 63 (2017).

[91] Y. Liu et al., Advanced Engineering Materials **1900613**, 1 (2019).

[92] P. Philipp, P. Barry, and T. Wirtz, Surface and Interface Analysis **46**, 7 (2014).

[93] Probion-Analysis, https://probion.fr/ecv-en/.

[94] R. A. Sinton, A. Cuevas, and M. Stuckings, Quasi-steady-state photoconductance, a new method for solar cell material and device characterization, in *Conference Record of the Twenty Fifth IEEE Photovoltaic Specialists Conference - 1996*, pages 457–460, 1996.

[95] H. Umemoto, Y. Nishihara, T. Ishikawa, and S. Yamamoto, Japanese Journal of Applied Physics **51**, 86501 (2012).

[96] H. N. Wanka and M. B. Schubert, Journal of Physics D: Applied Physics **30**, L28 (1997).

[97] M. Ohring, *Materials Science of Thin Films*, Elsevier Science & Technology, Burlington, UNITED STATES, 2001.

[98] L. T. Anh et al., Journal of Applied Physics **119**, 45703 (2016).

[99] F. Finger et al., Applied Physics Letters **65**, 2588 (1994).

[100] J. K. Holt et al., Thin Solid Films **395**, 29 (2001).

[101] O. Astakhov et al., Physical Review B - Condensed Matter and Materials Physics **79**, 104205 (2009).

[102] K. Wilken, F. Finger, and V. Smirnov, Energy Procedia **84**, 17 (2015).

[103] O. Astakhov et al., Physical Review B **79**, 104205 (2009).

[104] A. Tomasi et al., Nature Energy **2**, 17062 (2017).

[105] A. Descoeudres et al., Advanced silicon thin films for high-efficiency silicon heterojunction-based solar cells, in *2017 IEEE 44th Photovoltaic Specialist Conference (PVSC)*, pages 50–55, 2017.

[106] A. Richter, *Nanocrystalline Silicon Oxide in Silicon Heterojunction Solar Cells*, PhD thesis, 2017.

[107] R. Carius et al., Electronic properties of microcrystalline silicon, in *Amorphous and Microcrystalline Silicon Technology*, edited by S. Wagner, M. Hack, E. A. Schiff, R. Schropp, and I. Shimizu, volume 467 of *Materials Research Society Symposium Proceedings*, pages 283–294, Cambridge University Press, 1997.

[108] M. Pomaska et al., Journal of Applied Physics **119**, 175303 (2016).

[109] A. Dasgupta et al., Thin Solid Films **516**, 622 (2008).

[110] W. E. Spear and P. G. Le Comber, Solid State Communications **17**, 1193 (1975).

[111] R. E. Hollingsworth and P. K. Bhat, Applied Physics Letters **64**, 616 (1994).

[112] F. Demichelis, C. F. Pirri, and E. Tresso, Journal of Applied Physics **72**, 1327 (1992).

[113] D. Kaining et al., physica status solidi (a) **209**, 1960 (2012).

[114] K. Ding et al., Solar Energy Materials and Solar Cells **129**, 3 (2014).

[115] R. Soref and B. Bennett, IEEE Journal of Quantum Electronics **23**, 123 (1987).

[116] D. K. Schroder, R. N. Thomas, and J. C. Swartz, IEEE Journal of Solid-State Circuits **13**, 180 (1978).

[117] K. Narayanan and S. F. Preble, Optics Express **18**, 8998 (2010).

[118] T. C. Thi, K. Koyama, K. Ohdaira, and H. Matsumura, Journal of Applied Physics **116**, 44510 (2014).

[119] O. Keisuke, C. Trinh Thi, and M. Hideki, Japanese Journal of Applied Physics **56**, 102301 (2017).

[120] O. Keisuke, S. Junichi, and M. Hideki, Japanese Journal of Applied Physics **56**, 08MB06 (2017).

[121] T. Mishima, M. Taguchi, H. Sakata, and E. Maruyama, Solar Energy Materials and Solar Cells **95**, 18 (2011).

[122] Y. Yin, J. Long, S. Venkataraj, J. Wang, and A. G. Aberle, Energy Procedia **25**, 34 (2012).

[123] J. Perrin, Y. Takeda, N. Hirano, Y. Takeuchi, and A. Matsuda, Surface Science **210**, 114 (1989).

[124] M. Kondo, S. De Wolf, and H. Fujiwara, MRS Proceedings **1066**, 1001 (2011).

Acknowledgments

"Die Uhren gehen vielleicht mal vor und mal zurück. Aber die Zeit vergeht gleich schnell." It has been four years for me to live and study in Germany. I won't be here without the warm support from many people and I value everything I learned and shared with. I would like to express my deepest gratitude to those who contributes to this work and helped me during this work.

- Prof. Dr. Uwe Rau for the supervision and examination of this thesis, for providing me the opportunity to work in IEK-5.
- Prof. Dr. Andrei Vescan for taking care of the second review of the thesis.
- Prof. Dirk Uwe Sauer and Prof. Renato Negra for being in the defend committee and reviewing the dissertation.
- Dr. Kaining Ding for being a great supervisor. He showed me in many ways how to become a good scientist and make use of all you have. He leads us well both at work and in life, all the barbecues and hot-pots spark in memory.
- Dr. Friedhelm Finger for review of manuscripts and valuable comments.
- Prof. Dr. Hideki Matsumura for the external mentoring and fruitful discussion.
- Dr. Wolfhard Beyer for fruitful and enlightening discussions.
- Dr. Do Yun Kim for supervision in the early days.
- Dr. Manuel Pomaska for supervising my scientific activities. The countless and fruitful discussions we had contribute to the founding and complete of this work. His scientific thinking has also inspired me.
- Dr. Andreas Lambertz, Dr. Oleksandr Astakhov, Dr. Bittkau Karsten and Dr. Florian Lentz for their suggestion and advise in many aspects. Dr. Weiyuan

Duan and Dr. Kaifu Qiu for their discussion and support. Dr. Shenghao Li for reviewing manuscripts and this thesis.

- The many people who helped me with equipments, sample preparation and characterization. Andreas Schmalen, Johannes Wolff and Sven Schiffer for their technical support. Manuela Meyer for many introductions and sample preparation. Silke Lynen, Hilde Siekmann, Alain Doumit, Dr. Alaaeldin Gad, Sandra Moll and Andreas Mück for sample preparation. Wilfried Reetz, Oliver Thimm, Uwe Zastrow, Frank Pennartz, Dr. Uwe Breuer and Dr. Andreas Tiedemann for their support in characterization. Dr. Vladimir Smirnov for helping with closing gases so many times late in the afternoon.
- All the PhD students and interns for the great environment in IEK-5.
- All my lovely friends in IEK-5 and other places with whom I share the joy when time was bright and the sorrow when time was dark: Jinane Haddad, Samia Nadi, Robert Dolmans, Weiyuan Duan, Huimin Li, Depeng Qiu, Shenghao Li, Kaifu Qiu, Wei Qin, Zhifa Liu, Zhao Cao, Weiyan Wang, Zhirong Yao, Ding Li, Aryak Sigh, Yang Liu, Jeerawan Brendt, Alexandre Zamchiy, Malte Köhler, Annabel Mikosch, Dapeng Zhou, Wencai Leng and so on. You've lightened my days.
- My beloved family who support me and always have faith in me. You are the power that encourages me to walk this far.

Band / Volume 543
Processing and creep resistance of short SiC fiber containing Ti_3SiC_2 MAX phase composites
A. Dash (2021), vii, 125 pp
ISBN: 978-3-95806-558-1

Band / Volume 544
Synthese und Charakterisierung von Geopolymeren für die Entsorgung der Spaltprodukte ^{137}Cs und ^{90}Sr
S. K. Weigelt (2021), VI, 186 pp
ISBN: 978-3-95806-559-8

Band / Volume 545
Potential depletion of ozone in the mid-latitude lowermost stratosphere in summer under geoengineering conditions
S. Robrecht (2021), 185 pp
ISBN: 978-3-95806-563-5

Band / Volume 546
Two-phase Flow in Porous Transport Layers of Polymer Electrolyte Membrane Electrolysers
D. Borah (2021), xi, 196 pp
ISBN: 978-3-95806-564-2

Band / Volume 547
Effects of root temperature on food quality of horticultural crops
F. He (2021), V, 143 pp
ISBN: 978-3-95806-565-9

Band / Volume 548
Verhalten und Kontrolle von Schlacken des bioliq®-Vergasers
K. Mielke (2021), 162, XXXV pp
ISBN: 978-3-95806-566-6

Band / Volume 549
Gravity waves resolved in Numerical Weather Prediction products
C. Strube (2021), iii, 139 pp
ISBN: 978-3-95806-567-3

Band / Volume 550
Experimental study of the chemical degradation of biogenic volatile organic compounds by atmospheric OH radicals
M. Rolletter (2021), XIII, 199 pp
ISBN: 978-3-95806-568-0

Band / Volume 551
Infiltrated Positive Electrodes for All-Solid-State Sodium Batteries
T. Lan (2021), vi, 104 pp
ISBN: 978-3-95806-576-5

Band / Volume 552
Trajectory Analysis on the Asian Tropopause Aerosol Layer (ATAL) based on Balloon Measurements at the Foothills of the Himalayas
S. Hanumanthu (2021), xiv, 147 pp
ISBN: 978-3-95806-578-9

Band / Volume 553
Field assisted sintering of yttria ceramics for plasma etching applications
M. Kindelmann (2021), VI, 122, XXX pp
ISBN: 978-3-95806-579-6

Band / Volume 554
Characterisation of the effect of redox potential on the emission of greenhouse gases using wireless sensing techniques
J. Wang (2021), XIV, 104 pp
ISBN: 978-3-95806-581-9

Band / Volume 555
Stability assessment of variably saturated hillslopes using coupled hydromechanical models
S. Moradi (2021), xxxii, 123 pp
ISBN: 978-3-95806-583-3

Band / Volume 556
Catalytic-doping of Silicon Alloys for the Use in Silicon Heterojunction Solar Cells
Y. Liu (2021), 126 pp
ISBN: 978-3-95806-591-8

Energie & Umwelt / Energy & Environment
Band / Volume 556
ISBN 978-3-95806-591-8

Mitglied der Helmholtz-Gemeinschaft

JÜLICH
Forschungszentrum